

Innovative Tools and *in vivo* Methods for Tuberculosis Drug Discovery and Development

Thèse N° 9248

Présentée le 26 mars 2019

à la Faculté des sciences de la vie

Unité du Prof. Cole

Programme doctoral en approches moléculaires du vivant

pour l'obtention du grade de Docteur ès Sciences

par

Raphael Christopher SOMMER

Acceptée sur proposition du jury

Prof. A. Ablasser, présidente du jury

Prof. S. Cole, Prof. A. C. Oates, directeurs de thèse

Prof. A. van der Sar, rapporteuse

Prof. U. Schaible, rapporteur

Dr N. Dhar, rapporteur

2019

À ma Nonna

Abstract

Worldwide, tuberculosis (TB) is the leading cause of death due to a single infectious agent, claiming 1.6 million human lives and causing >10 million new cases in 2017 alone, mostly in low-income regions. The intracellular pathogen *Mycobacterium tuberculosis* is the etiological agent and generally infects the lungs. Although treatments exist, curing TB requires long and often expensive chemotherapy, frequently accompanied by undesirable side-effects. In the absence of an effective vaccine and with the increasing emergence of multidrug resistance, new and more powerful antibiotics are urgently needed to control the global TB crisis.

In this respect, benzothiazinones (BTZs), a class of new anti-TB compounds, have recently been discovered. Macozinone (PBTZ169), that has reached phase I and II clinical trials in Switzerland and Russia, respectively, is undoubtedly the most promising drug of this category. We derivatized PBTZ169 into a fluorescent chemical probe that efficiently, covalently and selectively labels the enzyme DprE1, thereby localizing the target of BTZs to the periplasm at the poles of actinobacteria. We further discuss the potential applications of such probes for *in vivo* imaging, mycobacterial detection and designing new diagnostic tools.

In general, the search for novel anti-mycobacterial drugs is an extremely long process, delaying the progression of new compounds down the pipeline and to the clinic. Assessing drug efficacy *in vivo* typically requires extensive resources and is time-consuming. This process can be shortened by applying alternative and innovative methods devised in this thesis, namely the implementation of *in vivo* imaging procedures and use of the zebrafish embryo model of mycobacterial infection for drug discovery and development.

In vivo imaging enables bacterial loads in animal models to be assessed in real time, by means of fluorescence or bioluminescence imaging. We constructed, optimized and characterized genetically engineered near-infrared fluorescent reporters of the pathogens *Mycobacterium marinum* and *M. tuberculosis* that allow direct visualization of bacteria in infected zebrafish and mice, respectively. Furthermore, we show that the fluorescence level accurately reflects the bacterial load, as determined by colony forming unit enumeration, thus enabling the efficacy of antibiotic treatment to be assessed in live animals. Alternatively, we applied autobioluminescent

M. tuberculosis to evaluate drug efficacy in mice and demonstrated that our system enables the therapeutic response to be followed in real time. Longitudinal imaging also reduces the number animals required thus providing a substantial gain of time and resources. Finally, the zebrafish embryo is an inexpensive and faster alternative model that has been applied to investigate mycobacterial pathogenesis. We implemented this model of *M. marinum* infection and successfully applied it to assess the activity of several drugs *in vivo*.

Altogether, the innovative methods described in this work are advantageous for TB drug discovery and development, especially for the *in vivo* evaluation of new anti-mycobacterial candidates, and provide more ethically acceptable approaches and biomedical applications.

Keywords

Tuberculosis (TB), mycobacteria, benzothiazinones, drug discovery and development, fluorescent probes, *in vivo* imaging, near-infrared imaging, bioluminescence imaging, mouse model, zebrafish model.

Résumé

La tuberculose est la majeure cause de décès due à un agent infectieux unique, dans le monde entier. Plus de 10 millions de personnes ont été atteintes par cette maladie et 1.6 millions en sont mortes en 2017 uniquement, principalement dans des régions à bas revenu. Le pathogène intracellulaire *Mycobacterium tuberculosis* est l'agent étiologique responsable de cette maladie et infecte généralement les poumons. Bien que des remèdes existent, soigner la tuberculose requiert un long traitement chimio-thérapeutique, souvent cher et fréquemment accompagné d'effets secondaires indésirables. En l'absence d'un vaccin efficace et avec l'émergence de multiples résistances aux traitements, de nouveaux antibiotiques plus puissants sont rapidement requis dans le but de contrôler l'épidémie de tuberculose.

Dans cette optique, les benzothiazinones (BTZs), une classe de nouveaux composés antituberculeux, ont récemment été découverts. La macozinone (PBTZ169), qui est récemment entrée en phase clinique I en Suisse et en phase clinique II en Russie, représente sans doute la molécule la plus prometteuse de cette catégorie. Nous avons transformé le PBTZ169 en sonde chimique fluorescente permettant de marquer efficacement, sélectivement et de manière covalente l'enzyme DprE1, indiquant la localisation de la cible des BTZs dans le périplasme de certaines actinobactéries, au niveau de leurs pôles. Nous discutons plus en détail les applications potentielles de telles marqueurs pour l'imagerie *in vivo*, pour la détection de mycobactéries et pour le design d'outils de diagnostic novateurs.

En général, la recherche de nouvelles molécules antimicrobiennes représente un processus extrêmement long, retardant la progression des composés candidats vers leurs applications cliniques. L'évaluation de ces molécules *in vivo* requiert typiquement un temps considérable et d'importantes ressources. Ce processus peut cependant être accéléré en appliquant certaines méthodes alternatives et innovantes, telles que l'implémentations de procédures d'imagerie *in vivo* et l'utilisation d'embryons de poissons-zèbres comme modèles d'infection mycobactérienne. Leur application à la découverte et au développement des composés antituberculeux est amplement discutée dans cette thèse.

L'imagerie *in vivo* permet d'évaluer la charge bactérienne dans des modèles animaux en temps réel, grâce à des techniques basées sur les phénomènes de fluorescence et de bioluminescence. Dans cet ouvrage, nous décrivons la construction, l'optimisation et la caractérisation de pathogènes (*Mycobacterium marinum* et *M. tuberculosis*) génétiquement modifiés afin de créer des souches fluorescentes dans le proche infrarouge. Ces souches permettent de visualiser directement les bactéries dans des poissons-zèbres des souris infectés, respectivement. De plus, nous démontrons que le niveau de fluorescence reflète précisément la charge bactérienne déterminée par énumération de colonies, ce qui permet d'évaluer l'efficacité d'un traitement antibiotique dans des animaux vivants. Comme méthode alternative, nous avons utilisé une souche de *M. tuberculosis* autoluminescente pour tester l'efficacité d'un médicament dans des souris et démontrons que notre système permet de suivre la réponse thérapeutique en temps réel. L'imagerie en série permet également de réduire le nombre d'animaux requis, apportant ainsi une considérable économie de temps et de ressources en général. Finalement, l'embryon de poisson-zèbre est un modèle animal alternatif, rapide et peu cher, qui peut être utilisé pour étudier la pathogénèse mycobactérienne. Nous avons implémenté ce modèle d'infection avec *M. marinum* et l'avons appliqué avec succès à l'évaluation *in vivo* de plusieurs antibiotiques en cours de développement.

Globalement, les méthodes innovantes décrites dans cet ouvrage sont avantageuses pour la recherche et le développement de nouvelles molécules antituberculeuses, notamment pour leur évaluation *in vivo*, et fournissent des approches et des applications biomédicales éthiquement plus acceptables.

Mots-clés

Tuberculose, mycobactéries, benzothiazinones, découverte et développement de nouveaux médicaments, sondes fluorescentes, imagerie *in vivo*, imagerie par fluorescence proche infrarouge, imagerie par bioluminescence, modèle murin, modèle de poisson-zèbre.

Zusammenfassung

Tuberkulose (TB) ist die weltweit führende Todesursache durch Infektionen, die durch einen einzelnen Krankheitserreger bedingt sind; allein im Jahre 2017 hat sie über 10 Millionen Erkrankungen verursacht und 1.6 Millionen Menschenleben gefordert, wobei vornehmlich Gegenden tiefer Einkommensschichten betroffen sind. Das intrazelluläre Pathogen *Mycobacterium tuberculosis* ist der Krankheitsverursacher und infiziert primär die Lungen. Obwohl Behandlungen existieren, ist für eine vollständige Genesung eine lange und zum Teil teure Chemotherapie vonnöten, die häufig von Nebenwirkungen begleitet wird. Da kein effizienter Impfstoff zur Verfügung steht und zudem vermehrt Multiresistenzen auftreten, besteht ein dringender Bedarf für neue, wirksamere Antibiotika, damit die globale TB-Krise unter Kontrolle gebracht werden kann.

Benzothiazinone (BTZs) stellen eine Gruppe neuer, kürzlich entdeckter anti-TB Wirkstoffe dar. Macozinon (PBTZ169) befindet sich bereits in klinischen Studien (Phase I in der Schweiz, Phase II in Russland) und ist das vielversprechendste Mitglied seiner Kategorie. Hier wird ein fluoreszierendes Derivat des PBTZ169 beschrieben, das als Sonde selektiv und kovalent an das Enzym DprE1 bindet, wodurch das Zielenzym der BTZs als sich an den Polen im Periplasium befindend lokalisiert werden konnte. Wir diskutieren das Potenzial solcher Sonden für die In-vivo-Bildgebung, Mykobakteriendetektion und für die Entwicklung neuer diagnostischer Werkzeuge.

Die Suche nach neuen antimykobakteriellen Medikamenten ist in der Regel ein sehr langwieriger Prozess, wodurch neue Verbindungen erst nach längerer Zeit weiteren Studien und letzten Endes klinischen Versuchen unterzogen werden können. Die In-vivo-Beurteilung von Medikamentenwirksamkeit benötigt viel Zeit und verlangt nach substantiellen Ressourcen. Dieser Prozess kann durch geeignete, alternative und innovative Methoden, die in dieser Dissertation beschrieben sind, verkürzt werden: Durch die Implementierung von In-vivo-Bildgebungsverfahren einerseits, und durch die Verwendung eines Zebrafischembryomodells für Mykobakterieninfektion und -medikamentenentwicklung andererseits.

Fluoreszenz- oder Biolumineszenzbildgebung erlaubt die In-vivo-Beurteilung der bakteriellen Belastung in tierischen Modellorganismen in Echtzeit. In dieser Arbeit werden gentechnisch Nahinfrarot-Stämme für die Krankheitserreger *Mycobacterium marinum* und *M. tuberculosis* entwickelt, optimiert und charakterisiert, welche eine unmittelbare Sichtbarkeitsmachung der Bakterien in infizierten Mäusen und Zebrafischen ermöglichen. Zudem wird gezeigt, dass die Stärke der Fluoreszenz mit der bakteriellen Belastung korreliert, was durch Zählen der kolonienformierenden Einheiten (CFUs) bestätigt wurde; damit kann nunmehr die Wirksamkeit einer antibiotischen Behandlung in lebenden Tieren beurteilt werden. Autobioluminiszente *M. tuberculosis* werden zur Beurteilung der Medikamentenwirksamkeit in Mäusen hinzugezogen und es wird gezeigt, dass sich der therapeutische Effekt damit in Echtzeit verfolgen und bewerten lässt. Überdies werden durch longitudinale Bildgebung weniger Versuchstiere benötigt, womit Zeit und Ressourcen eingespart werden können. Zebrafischembryos stellen ein kostengünstiges, schnelles Alternativmodell zur Untersuchung der mykobakteriellen Pathogenese dar. Anhand der Infektion mit *M. marinum* wird die Aktivität verschiedener Medikamente *in vivo* beurteilt.

Die hier beschriebenen, innovativen Methoden sind der Entwicklung und Entdeckung neuer TB-Medikamente dienlich; sie ermöglichen im Speziellen die In-vivo-Beurteilung neuer potenziell antimykobakterieller Verbindungen und die Verwendung ethisch besser akzeptabler Versuchsprotokolle.

Schlagwörter

Tuberkulose (TB), Mycobakterien, Benzothiazinone, Fluoreszenzmarkierte Sonde, Medikamentenentdeckung und -entwicklung, In-vivo-Bildgebung, Nahinfrarotbildgebung, Biolumineszenzbildgebung, Mausmodell, Zebrafischmodell.

Contents

Abstract	v
Résumé	vii
Zusammenfassung	ix
Contents	xi
Chapter 1. General Introduction	15
Tuberculosis – Ending the Epidemic by 2035?	16
Microbiology and Pathogenesis	19
Strategies to Address the Global TB Situation	21
Discovering and Developing New Anti-TB Drugs	24
Animal Models of TB	27
<i>in vivo</i> Imaging of Mycobacterial Infections.....	30
Rationale and Thesis Outline	33
References	35
PART I FLUORESCENT BENZOTHIAZINONES	43
Chapter 2. Fluorescent Benzothiazinones to Label DprE1	45
Abstract	46
Introduction	46
Results and Discussion.....	48
Concluding Remarks	57
Methods.....	57
References	61
Supporting Information	65
Chapter 3. Fluorescent Benzothiazinone Analogues for Mycobacterial Detection	77
Introduction	78
Results	78
Discussion	82
Methods.....	83
References	86

PART II	<i>IN VIVO</i> IMAGING.....	89
Chapter 4.	Near-Infrared Fluorescence Imaging of TB Infection.....	91
	Abstract.....	92
	Introduction.....	92
	Results.....	95
	Discussion.....	105
	Methods.....	107
	References.....	112
	Supplementary Data.....	116
Chapter 5.	Bioluminescence Imaging of TB Infection.....	119
	Abstract.....	120
	Introduction.....	120
	Results.....	122
	Discussion.....	130
	Methods.....	132
	References.....	135
	Supplementary data.....	138
PART III	CONSUMPTIVE ZEBRAFISH EMBRYOS	139
Chapter 6.	Zebrafish Embryos for TB Drug Discovery	141
	Preface.....	141
	Introduction.....	142
	<i>in vivo</i> Activity of Pyridomycin in <i>M. marinum</i> -Infected Embryos.....	144
	Investigating the Role of <i>fadD9</i> in Clofazimine Resistance <i>in vivo</i>	147
	Efficacy of Inhibitors of Mycobacterial Virulence Factor Secretion.....	151
	Activity of Arylvinylpiperazine Amides Against <i>M. abscessus in vivo</i>	155
	General Discussion.....	158
	Methods.....	160
	References.....	162

PART IV	RETROSPECTIVES AND PERSPECTIVES	167
Chapter 7.	Conclusion and Outlook.....	169
	References	175
	Acknowledgements.....	177
	Abbreviations.....	179
	<i>Curriculum Vitae</i>.....	183

Chapter 1.

General Introduction

TEN MILLION. This corresponds to the estimated number of people who fell ill with tuberculosis (TB) in 2017 alone, according to the World Health Organization (WHO).¹ Among them, the disease claimed 1.6 million deaths, including 300'000 among HIV-positive people. Worldwide, TB is the leading cause of death due to infection with a single pathogenic agent, *Mycobacterium tuberculosis*. The increasing emergence of drug-resistant strains of *M. tuberculosis* and the absence of an effective vaccine are major drivers of this long-lasting TB epidemic, highlighting the urgent need for new and more efficient antibiotics. In order to understand the global challenges related to TB and the strategies ongoing to tackle the disease, let us start with a general introduction in which I would like to present some approaches that I investigated during my doctoral studies, in order to refine and accelerate the TB drug discovery process.

TUBERCULOSIS – ENDING THE EPIDEMIC BY 2035?

Tuberculosis in the 20th century

In March 1882, Robert Koch, a German doctor, announced his discovery of the bacillus *M. tuberculosis*, that he described as the etiological agent responsible for the TB disease,² although there is now evidence that humans were already affected by TB more than 8'000 years ago.³ His discovery earned him the Nobel Prize in 1905. Since the end of the 19th century, fresh air, sunlight, outdoor exercise and good diet were associated with a better control of TB and were the only medical prescriptions for patients. This led to the apparition of sanatoria, which are medical institutions commonly installed in the mountains and dedicated to hosting and treating TB patients. In Switzerland, signs of such facilities still exist in Davos and Leysin for instance but they have been repurposed. Of note, the isolation of TB patients in sanatoria was also likely a collateral benefit for society.

Between 1906 and 1919, Calmette and Guérin obtained an attenuated strain of *Mycobacterium bovis*, the mycobacterial agent of bovine TB, following multiple passages *in vitro*.⁴ This strain had indeed lost its capability to cause disease in animals and is today known as Bacille Calmette-Guerin (BCG). Attenuation of BCG has been attributed to the loss of RD1, a genetic region encoding virulence factors in pathogenic mycobacteria. BCG was used for the first time in 1921 as a vaccine in an attempt to prevent TB in humans. Vaccination with BCG proved to be protective against miliary and meningeal TB in children. However, it does not prevent primary infection nor the progression of latent pulmonary infection to active TB in adults.¹ The impact of BCG vaccination on transmission of the disease is therefore limited and this explains partly why the

epidemic has not been eradicated. Almost 100 years after its discovery, BCG also remains the only vaccine available as preventive treatment for human TB, although with considerably limited efficacy.¹

In 1940, the discovery of streptomycin⁵, the first effective antibiotic against TB, constituted a major breakthrough and paved the way for anti-TB chemotherapy and further drug discovery. For 20 years, fruitful research and development led to the marketing of many anti-TB drugs. With the extensive utilization of these drugs in regimens, along with the social and economic development, a substantial decline in TB cases and deaths has been experienced worldwide. In the late 1980s, however, a resurgence of TB was seen mainly due to the HIV/AIDS pandemic and the emergence of drug-resistant strains of *M. tuberculosis*. This situation led the WHO to declare TB a global health emergency in 1993.

Tuberculosis today and modern challenges

Worldwide, TB is the major cause of death due to a single infectious agent and ranks above HIV/AIDS and malaria. In Western Europe and North America, high-income regions, the disease burden is extremely low with <10 cases and even <1 death per 100'000 inhabitants. In contrast, two thirds of TB cases are distributed among eight countries: India, China, Indonesia, The Philippines, Pakistan, Nigeria, Bangladesh and South Africa (Figure 1). In 2017, among the 1.3 million new TB cases in HIV-negative people and the 300'000 new cases among HIV-positive people, the WHO estimated that 580'000 patients were not responding to rifampicin, a frontline anti-TB drug. Among rifampicin-resistant (RR) TB patients, 82% had multidrug-resistant (MDR) TB, meaning resistance to at least rifampicin and isoniazid (a second frontline drug). Drug resistance is certainly today one of the greatest threats and challenges related to the TB epidemic. It is thought that one quarter of the world's population is infected with *M. tuberculosis*, 90% of them carrying latent TB, which is an inactive and non-contagious form of the disease. These people, who often remain undiagnosed, represent therefore a major reservoir. Aging and weakening of the immune system (sometimes associated with HIV co-infection for instance) are, however, major drivers of TB reactivation in latently infected patients. Hence, the end of TB as an epidemic is still for many countries, an aspiration rather than a reality.¹

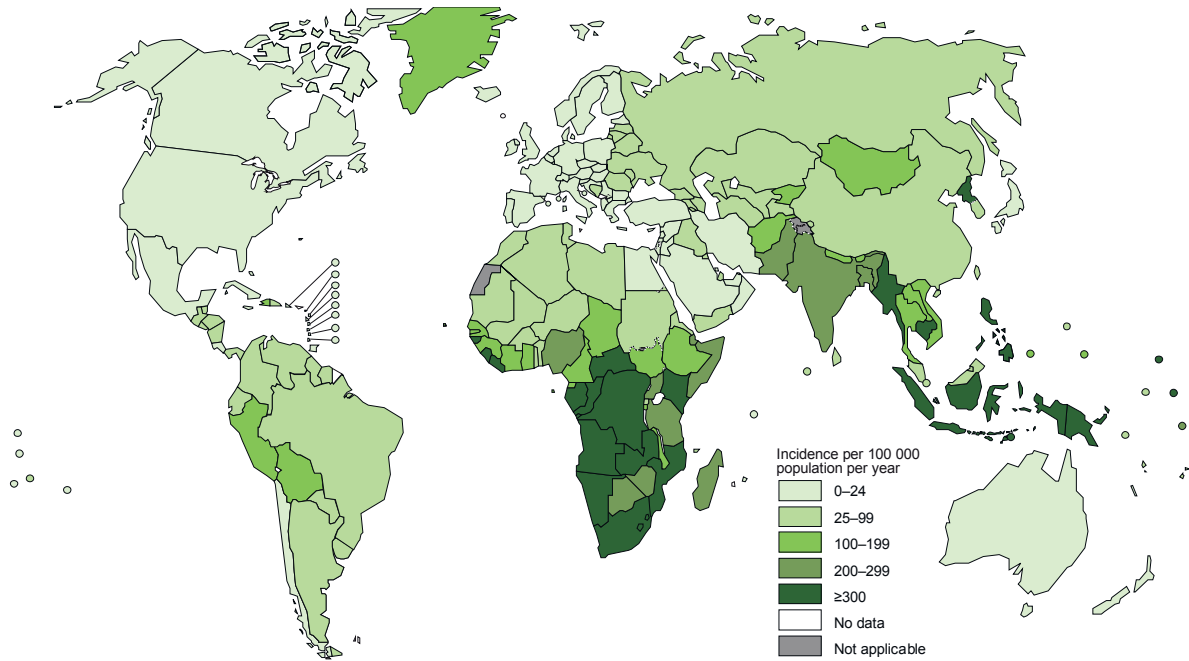


Figure 1. Estimated TB incidence rates, 2017. Adapted from the WHO’s Global Tuberculosis Report 2018.¹

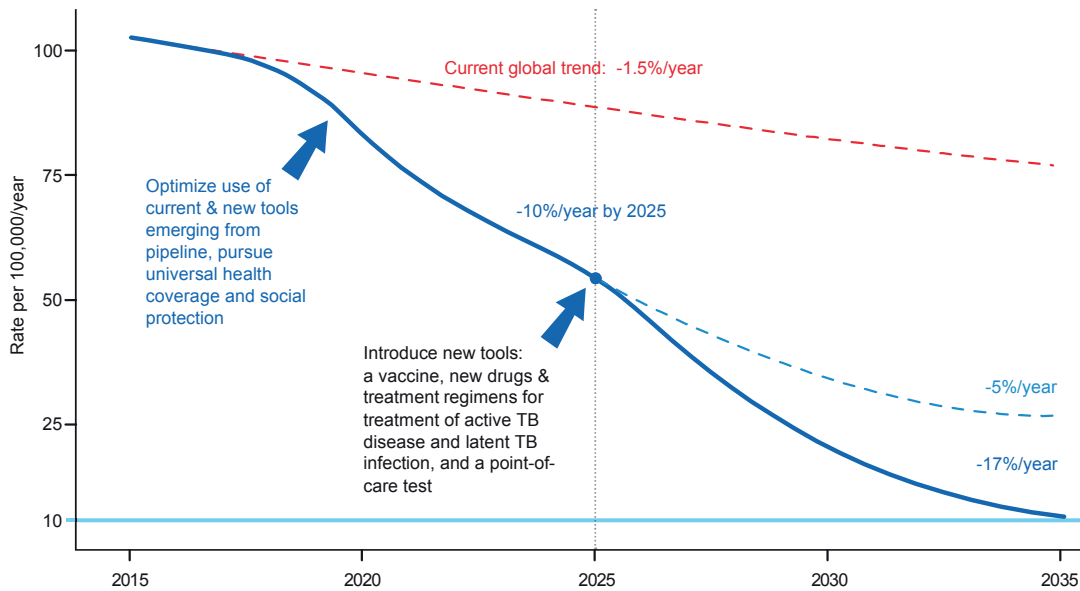


Figure 2. Desired decline in the global TB incidence rates to reach the 2035 targets. Adapted from the WHO’s End TB Strategy brochure.⁶

The End TB Strategy

The overall goal of the WHO's End TB Strategy is to end the global TB epidemic by achieving substantial reduction of TB deaths and incidence rate¹. The major target fixed by the strategy is in 2035 and sets the following indicators: reduction of TB deaths by 95%, reduction of TB incidence rate by 90% and zero TB-affected households experiencing disastrous costs due to the disease. The actual global trend concerning the TB incidence rate is a decline of 1.5% per year (Figure 2) and in order to meet the fixed milestones and targets, the strategy relies on three pillars: 1) integrated, patient-centred care and prevention, 2) bold policies and supportive systems and 3) intensified research and innovation.⁶ Notably, the third pillar promotes the discovery and development of new tools and strategies, and this has been a major source of inspiration for the different approaches that will be presented in this thesis, including the amelioration of the drug discovery process by implementing real-time evaluation of antibiotic efficacy *in vivo* and the exploitation of the zebrafish embryo as a faster and cheaper surrogate to the mouse model of disease.

MICROBIOLOGY AND PATHOGENESIS

***M. tuberculosis* and mycobacteria**

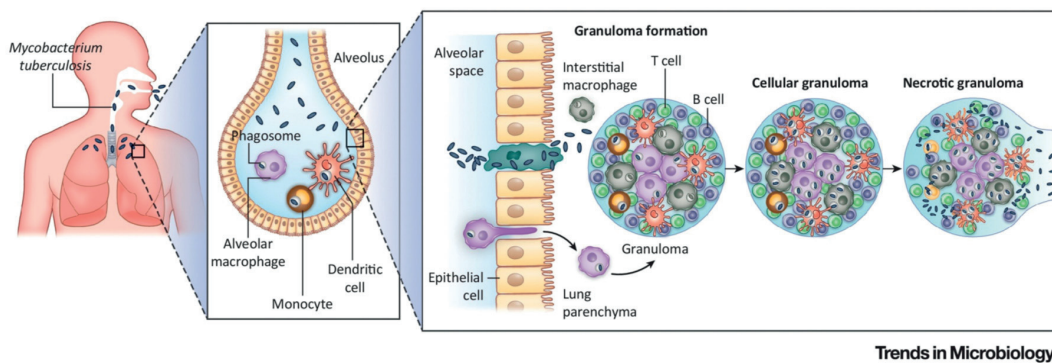
The TB disease is caused by a range of mycobacteria closely genetically related and part of the *M. tuberculosis* complex (MTBC)⁷, including, *M. tuberculosis* and *Mycobacterium africanum*, causing TB in humans. Several animal-adapted strains from the MTBC cause TB in non-human species, exemplified by *M. bovis*, primarily causing TB in cattle.⁸ Not included in the MTBC are *Mycobacterium ulcerans*, causing Buruli ulcer in humans, and *Mycobacterium leprae*, the agent responsible for leprosy. Nontuberculous mycobacteria (NTM) are opportunistic pathogens that can cause disease in immunosuppressed humans, such as HIV-positive patients. NTM typically include species from the *Mycobacterium avium* complex, *Mycobacterium kansasii*, *Mycobacterium marinum* and *Mycobacterium abscessus*. Finally, *Mycobacterium smegmatis* is a rapid-growing bacterial species from the genus *Mycobacterium* commonly used in laboratories as a surrogate to *M. tuberculosis*, as it is not pathogenic and grows fast (generation time ~3 h).

M. tuberculosis is a slow-growing (generation time ~20 h in laboratory media), obligate aerobe; facultative intracellular and rod-shaped bacterium.⁹ It is neither Gram-positive nor Gram-negative but acid-fast and can be identified by Ziehl–Neelsen staining. It carries a single circular chromosome of ~4.4 Mbp.⁷ Its thick cell envelope, containing complex lipids and sugars, is a dominant feature of *M. tuberculosis*.⁹ Unlike the uncultivable pathogen *M. leprae*, *M. tuberculosis*,

as well as *M. marinum* and *M. smegmatis*, are genetically accessible and multiple tools are available to study the essentiality of certain genetic features or to express heterologous genes, for example coding for fluorescent proteins, to construct mycobacterial reporters.

Pathogenesis

The disease is spread when people with active TB cough or sneeze, expelling bacteria into the environment in aerosol droplets. The common route of entry of *M. tuberculosis* into the body is by inhalation via the respiratory tract (Figure 3). The bacteria are then translocated towards the lower respiratory tract where they are generally engulfed by phagocytic cells.¹⁰ Alveolar macrophages are the dominant cell type being infected by *M. tuberculosis* and the bacteria can actively block the fusion of the phagosome with the lysosome, avoiding host cell clearance and promoting their intracellular survival.^{9,11} Migration of infected cells to the lung parenchyma generates a multicellular (including neutrophils, monocytes and lymphocytes) host response resulting in the formation of a granuloma. The granulomatous structure is constituted of several types of immune cells, as simplified and depicted in Figure 3. It contains the bacteria and limits the propagation of the infection, leading to latent TB.¹⁰ This situation applies to >90% of immunocompetent individuals and infected patients will remain asymptomatic and non-contagious while the pathogens persist in a dormant state.¹² AIDS and immunosuppressive treatments may cause reactivation and progression to active TB disease, following failure of the immune containment.¹⁰ In some cases, *M. tuberculosis* may disseminate to other sites such as the lymph nodes, pleura or the spinal cord (Pott's disease).¹³



Trends in Microbiology

Figure 3. Infection with *M. tuberculosis*. The infection begins when bacteria are inhaled and directed to the lower respiratory tract, where they are generally taken up by phagocytic cells. If this first line of defence does not eliminate the bacteria, migration of the infected cells to the parenchyma leads to the recruitment of more immune cells to constitute a granuloma. The granulomatous structure contains *M. tuberculosis*, preventing the progression of the infection. Upon failure of this containment, reactivation and dissemination of the bacteria can give rise to the active and contagious form of the TB disease. Figure adapted from⁹.

STRATEGIES TO ADDRESS THE GLOBAL TB SITUATION

Antibiotics

Antibiotics are generally small molecule drugs aimed at controlling and eliminating the bacterial agent responsible for an infection, while minimizing side-effects on the body and the normal flora. Since the discovery of streptomycin in 1943, antibiotic treatments, as well as social and economic development, have dramatically reduced the TB burden. Subsequently discovered drugs, with better safety profiles, enabled shorter and more efficient treatment to be implemented in the following years (Figure 4). It was soon observed that the administration of streptomycin alone rapidly led to the apparition of resistant strains and TB has since then mainly been managed by the administration of regimens containing two or more drugs (Figure 4). The regimen recommended by the WHO nowadays for treating active and drug-sensitive TB is composed of an intensive 2 months treatment phase with the frontline drugs isoniazid, rifampicin, pyrazinamide and ethambutol, followed by a continuation phase with isoniazid and rifampicin for four months.¹² In the case of drug-resistant TB, however, the treatment is much longer, heavier and has more undesirable side-effects. It consists of four second-line drugs, including a fluoroquinolone (moxifloxacin, levofloxacin, gatifloxacin), a parenteral agent (amikacin, capreomycin, kanamycin), a core second-line drug (ethionamide, prothionamide, cycloserine, terizidone, *para*-aminosalicylic acid) and an add-on drug, as recommended by the WHO since 2016.

The apparition and transmission of MDR *M. tuberculosis* and the onset of the HIV/AIDS pandemic led to a resurgence of TB and revived the search for new and more efficient antibiotics. Meanwhile, new patient data have arisen and the WHO has revised the guidelines for MDR/RR-TB treatment, leading to key changes in the recommended regimen, published in a communication in August 2018.¹⁴ The revised recommendation, based on the latest evidence regarding the balance of effectiveness to safety, now includes: 1) medicines to be prioritized (levofloxacin or moxifloxacin, bedaquiline and linezolid), 2) medicines to be added next (clofazimine, cycloserine or terizidone) and 3) medicines to be added to complete the regimen, especially if some of the previous drugs cannot be used (ethambutol, delamanid, pyrazinamide, imipenem-cilastatin or meropenem, amikacin, ethionamide or prothionamide, *para*-aminosalicylic acid). The second-line injectable agents kanamycin and capreomycin are not recommended anymore. While immediate application of the new guidelines to every MDR-TB patient is not possible, strategic planning will be required. The revision of these guidelines reflects consideration of the most recent advances in terms of drug discovery and development, promoted by the third pillar of the End TB Strategy. However, the current status of the rare new or repurposed drugs remains insufficient to face the global TB epidemic.

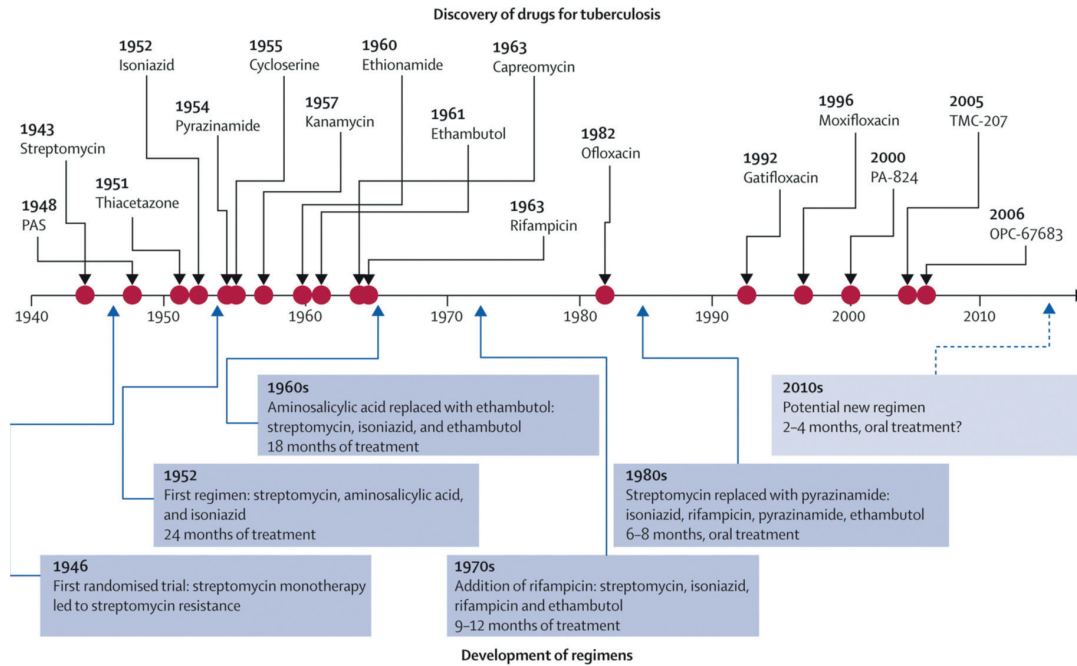


Figure 4. History of drug discovery and development of treatment regimens for TB.
Adapted from¹⁵.

Vaccines

Bacille Calmette-Guérin (BCG), used for the first time in 1921, remains nowadays the only licensed TB vaccine for human beings. It has proven to be effective against severe childhood TB (meningeal and miliary) while the protective effect of BCG vaccination is variably lost in adults.¹⁶ Although BCG vaccination has been widely used and has protected many infants, the need for protection against TB infection and reactivation in adults remains unmet. Much effort is currently needed for TB vaccine development and different novel strategies are being investigated. These new vaccine candidates are for instance based on protein/adjuvant mixtures containing *M. tuberculosis* antigens (e.g. Ag85B, ESAT-6), viral vectors to deliver *M. tuberculosis* antigens into host cells, mycobacterial whole cell or extracts and live attenuated mycobacterial strains.¹⁷ Notably, MTBVAC is the first live attenuated *M. tuberculosis* based vaccine reaching clinical trials¹⁸ and new recombinant strains of BCG are being investigated, BCG *ΔureC::hly* (VPM1002) being the most advanced one (in clinical phase III).¹⁹

Diagnostic tools

A limited number of tools are available for the diagnosis of TB and the choice of the available methods depends on whether the patient is suspected to have latent TB or active disease.¹⁰ In the first case, two tests are available: the tuberculin skin test (TST) and the interferon-gamma (IFN- γ) release assay (IGRA). Tuberculin, a sterilized *M. tuberculosis* extract initially developed by Robert Koch as a potential, albeit unsuccessful cure for TB, induces a skin reaction in people who have cell-mediated immunity to antigens contained in the preparation, when injected intradermally.^{10,20} The size of the resulting induration is the major readout of this diagnostic test but it fails to discriminate between patients truly infected with *M. tuberculosis* and those who had been previously vaccinated with BCG (likely due to an overlap of the antigens from both species, contained in the tuberculin preparation). IGRA was introduced in the 2000s and is an *in vitro* blood test quantifying T-cell release of IFN- γ following stimulation with ESAT-6 and CFP-10, two RD1-encoded proteins.²¹ More specific for *M. tuberculosis* than TST, IGRA remains less accessible in low-resource settings as it requires specific reagents, and advanced equipment and laboratory skills.

The diagnosis of active TB relies mainly on the isolation and identification of *M. tuberculosis* in samples from infected patients. The most accessible and widely used technique is smear microscopy, where bacilli are visually identified from sputum samples.²² However, this method generates a high percentage of error and is poorly sensitive. Culture-based methods are applied but necessitate laboratory settings and require more time before a precise diagnosis can be made. Molecular assays have become an attractive option since 2010, exemplified by the Xpert MTB/RIF technology (Cepheid Inc.), a nucleic acid amplification test that can additionally detect rifampicin resistance from sputum samples.²³ Thanks to its sensitivity and specificity, this system is now recommended by the WHO as first-line diagnostic test for people suspected to have active TB. In clinical settings, microscopy, culture- and molecular-based assays are complemented by imaging techniques, such as chest X-ray radiography or positron emission tomography coupled to computed tomography (PET/CT), to detect and analyse TB-induced lesions in the lungs.^{24,25}

Each of the proposed diagnostic solutions has diverse advantages and limitations in terms of sensitivity, specificity or cost, and the need for a rapid, precise and cost-effective point-of-care diagnostic tool providing prognosis value, remains unmet.

DISCOVERING AND DEVELOPING NEW ANTI-TB DRUGS

The urgent need for new anti-TB drugs

*“In the absence of an effective vaccine and with the increasing emergence of drug-resistant *M. tuberculosis*, there is an urgent need for new, more efficient, faster-acting and better tolerated treatments for TB”.* This type of statement is recurrent in many recent publications related to TB and drug discovery, and describes well the importance and the need for new antibiotics and strategies to confront TB. Ideally, new drugs should permit shorter treatments (especially for MDR-TB), have limited side-effects, be easy to administer, affordable and compatible with other TB drugs, and with antiretroviral therapies.

The drug discovery and development process

The leads in the TB drug development pipeline (Figure 5) commonly arose from phenotypic screening of a large library of compounds, assessed for their efficacy in cell-based assays. The subsequent target identification, validation and mechanism of action is typically investigated with whole-genome sequencing of resistant mutants.²⁶ More rarely, rational drug design and a target-to-drug approach has been applied.²⁷ The following hit-to-lead stage typically involves structure-activity relationship (SAR) studies, determination of the physicochemical properties, cytotoxicity and *in vitro* stability studies.²⁸ The subsequent lead optimization process involves further medicinal chemistry, combination and *in vivo* efficacy investigations. If successful, the optimized lead further continues to preclinical and clinical studies, in which the safety, tolerability, pharmacokinetics/pharmacodynamics and efficacy are investigated. The *in vivo* efficacy is commonly assessed in mouse models of TB infection, although such assays are time-consuming and require substantial resources. Strategies to boost the evolution of a lead compound at this stage will be investigated and discussed later.

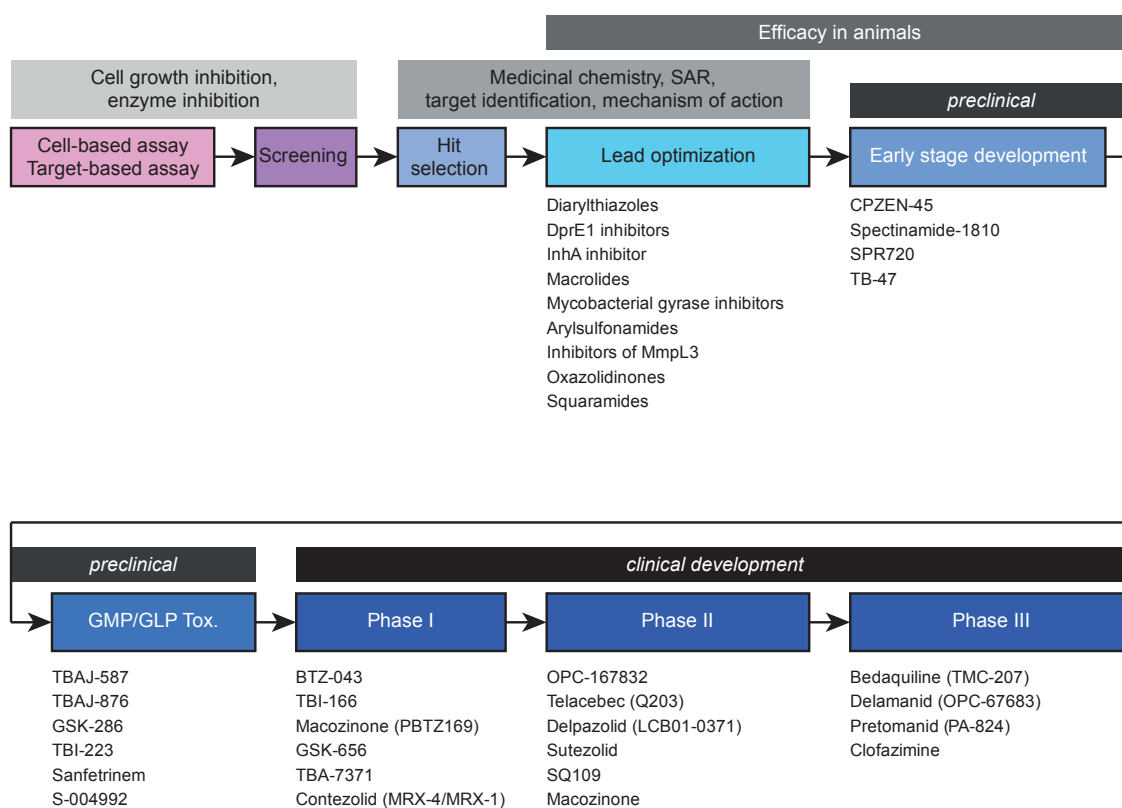


Figure 5. 2018 Global new TB drug pipeline. This figure describes new molecular entities or repurposed drugs not yet approved (or only conditionally approved), being developed for TB treatment, as proposed by the Working Group on New TB Drugs. Adapted from <https://www.newtbdrugs.org/pipeline/clinical>, the WHO's Global TB Report 2018¹ and²⁸. Compounds are listed under their current stage. Note the drugs macozinone and bedaquiline, currently in clinical phases I/II and III, respectively, which will be applied to *in vivo* imaging experiments further in the present work. Beside new or repurposed drugs, new regimen (not shown) are currently in clinical trials, aiming to shorten treatment duration for MDR-TB.

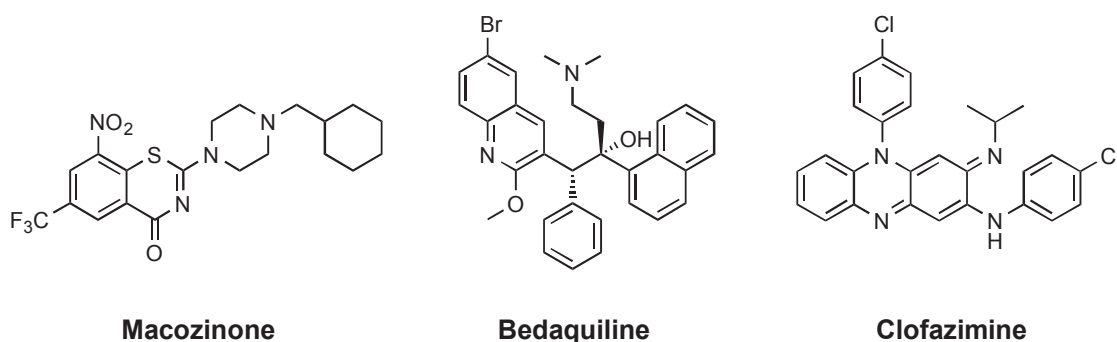


Figure 6. Molecular structure of macozinone, bedaquiline and clofazimine.

Focus on some promising TB drugs

The drugs presented in the current pipeline in Figure 5 are either new chemical entities or repurposed drugs. I would like to discuss three famous examples (Figure 6), relevant for the coming chapters of this thesis.

- (i) Macozinone, previously known as PBTZ169, is a preclinical candidate optimized from the lead compound BTZ043. It is a piperazine-containing benzothiazinone (BTZ), a new class of highly specific anti-mycobacterial compounds, targeting the essential enzyme DprE1, that is necessary for the synthesis of key cell wall components.²⁹⁻³¹ Notably, macozinone covalently inhibits DprE1 by forming a semimercaptal adduct with Cys378 in the active site of this enzyme, in *M. tuberculosis*.³² It shows synergistic effects with bedaquiline³³ and clofazimine³⁴ in preclinical models. Macozinone has completed phase I clinical trials in Switzerland and has started a phase II in Russia. Beside its potential as anti-TB drug, macozinone has been derived into a fluorescent chemical probe for specific labelling of DprE1 in several BTZ-sensitive actinobacteria.³⁵ Fluorescent BTZ derivatives are the subject of the second chapter of this work and potential applications of mycobacterial labelling *in vivo* with fluorescent BTZ analogues are discussed in chapter 3.
- (ii) Bedaquiline (TMC-207), a diarylquinoline drug discovered in 2005, is an inhibitor of the proton pump of the adenosine triphosphate (ATP) synthase in *M. tuberculosis*. Point mutations in *atpE*, encoding a part of the F₀ subunit of the ATP synthase, conferred bedaquiline resistance.³⁶ The Food and Drugs Administration (FDA) granted accelerated approval for bedaquiline (commercial name SIRTURO™) – the first approved new TB drug in 40 years – as part of combination therapy for adults with MDR-TB.³⁷ Interestingly, bedaquiline is also active against the NTM *M. abscessus*³⁸ and is probably one of the most advanced, promising and entirely new anti-mycobacterial drugs discovered to date, along with the BTZs. The comparative efficacy of bedaquiline and other drugs in mice, assessed with *in vivo* imaging, will be discussed in chapters 4 and 5.
- (iii) Clofazimine is a drug used to treat leprosy, a disease caused by long-term infection with *M. leprae*. In combination with rifampicin and dapsone, it is recommended by the WHO for the treatment of leprosy³⁹ and was recently repurposed for the treatment of MDR-TB.⁴⁰ The precise mode of action of clofazimine is poorly understood and cannot be assessed in *M. leprae* as this organism cannot be cultured *in vitro*. An investigation of a potential mechanism of resistance to clofazimine is described in the zebrafish model of *M. marinum* infection in chapter 6.

ANIMAL MODELS OF TB

In the context of infectious diseases and more precisely TB, different animal models have been exploited to gain more insights into the pathogenesis, the pathophysiology and the response of the host to a microbial infection. Animal models are also necessary to test new vaccine candidates in terms of safety and protective efficacy, to help with assessing new antimicrobials and designing new therapies. Even if a given species used as a model is closely genetically related to *Homo sapiens*, it is important to remember that animals are *not* humans and observations made in animal models do not guarantee that identical events will happen in humans.⁴¹ I will present below some animal models with particular relevance to the subject of this thesis, that have proven to be useful for the understanding of TB pathogenesis and then focus on their application to drug development.

The mouse model

Mice are one of the most accessible mammalian species to study TB and provide a living, breathing, vertebrate lung with the capacity to perform a large variety of experiments. Major knowledge regarding the immune response to *M. tuberculosis* infection has been obtained with this model.⁴² Several routes of infection with the pathogen have been explored, including intraperitoneal or intravenous injection, intranasal or intratracheal instillation and aerosol exposure, the latter mimicking more realistically the natural route of infection by reproducibly delivering a suspension of bacteria into the lungs of the animals following inhalation.⁴³ The susceptibility to TB varies among inbred mouse strains. For instance, C57BL/6J and BALB/c mice are more resistant to *M. tuberculosis* infection and will survive much longer than their CBA, C3HeB/FeJ, DBA/2 or 129SvJ counterparts.⁴⁴ The development of gene knockout mice allowed the importance and necessity of immune cell types or signaling molecules to be recognized. For example, mice with the gene for interferon-gamma (IFN- γ) knocked out, mice lacking tumor necrosis factor alpha (TNF- α) receptor or granulocyte-macrophage colony-stimulating factor (GM-CSF) are much more susceptible to infection, demonstrating the important role of these cytokines in TB immunity.^{45–47} Immunodeficient mice are obviously much more susceptible to TB than wild type BALB/c or C57BL/6J. For instance, infection of athymic BALB/c (nude) mice with *M. tuberculosis* underlined the importance of T-cells in host immune response.⁴⁸ Severe combined immunodeficiency (SCID) mice carry the loss-of-function *prkdc*^{scid} mutation, resulting in incomplete V(D)G recombination and inability for T- and B-cells to fully mature. SCID mice have therefore both impaired cellular and humoral immunity and are highly permissive to *M. tuberculosis* expansion. Indeed, while the bacterial burden in BALB/c plateaus around $10^6 - 10^7$ colony forming units (CFUs)⁴⁹, a higher bacterial load can be achieved in SCID animals. CB-17 SCID mice have been used for *in vivo* optical imaging of *M. tuberculosis*.^{50,51} Based on previous observations and in an effort to increase

the sensitivity of *in vivo* imaging, we introduce in this work SCID Hairless Outbred (SHO) mice for real-time monitoring of TB infection and drug assessment, by means of whole body imaging.

The application of the mouse model of chronic TB infection to evaluate drug efficacy *in vivo* generally involves the resistant mouse strains BALB/c or C57BL/6J and the following scheme. Groups of mice are initially exposed to aerosolized *M. tuberculosis* and kept without treatment for one month, until the bacterial load reaches $\sim 10^6$ CFUs per lung. Treatment is then administered by oral gavage for different periods of time but typically for at least one month. Relapse experiments, to evaluate the efficacy and durability of drug treatments, last much longer and the treatment is in this case administered for up to six months and the animals are then held for several months to assess the frequency and extent of relapse. To assess the efficacy of a given treatment, mice are sacrificed at different time points, lungs are excised, homogenized and serial dilutions are plated on agar media for CFU enumeration. Note that it takes 4 weeks or so for *M. tuberculosis* colonies to form on agar plates. Overall, drug testing in mice requires extensive resources, large numbers of animals, is time-consuming, and the measurements are in general endpoints requiring the euthanasia of the animals. The implementation of *in vivo* optical imaging for rapid, real-time and longitudinal assessment of antibiotic efficacy with luminescent and fluorescent reporters is a major subject of this thesis, described and discussed in chapters 4 and 5.

The zebrafish model

As discussed above, human TB typically affects the lungs and upper respiratory tract. It seems therefore contradictory to use fish as a model for TB, as they do not have lungs and are furthermore cold-blooded, which may be a major disadvantage for *M. tuberculosis* infection (optimal growth at 37°C).⁵² Despite these considerations, zebrafish (*Danio rerio*) prove to be excellent subjects to investigate the pathogenesis of several pathogens, as they possess both innate and adaptive immunity, and extensive homology with the human immune system.⁵³ The zebrafish model of TB involves the opportunistic human pathogen *Mycobacterium marinum*, a close genetic relative to *M. tuberculosis* and a natural pathogen for fish with an optimal growth temperature around 30°C. Interestingly, systemic infection of zebrafish with *M. marinum* results in bacterial phagocytosis by macrophages and formation of granulomatous structures histologically similar to human granulomas caused by *M. tuberculosis* infection.^{54,55} Notably, zebrafish embryos solely rely on the innate immune system and larvae are optically clear, permitting real-time monitoring with microscopy.^{52,54} Both the bacteria and the host are genetically tractable, enabling the roles of different immune cells, macrophages and neutrophils for instance, to be readily observed.⁵⁶⁻⁵⁸ On the bacterial side, the role of several mycobacterial virulence factors have been understood by tracking mutant *M. marinum* upon zebrafish embryo infection.⁵⁹⁻⁶²

Beside the investigation of mycobacterial pathogenesis and virulence factors, *M. marinum*-infected zebrafish embryos have been used to assess the efficacy of new anti-mycobacterial compounds.^{33,63-65} The application of the *M. marinum*-zebrafish embryo infection model to the search for new anti-TB drugs can dramatically accelerate the drug development process. Indeed, drug testing in this model can be performed *in vivo*, over a short period (5 days) and with a medium/high throughput. This topic is discussed in chapter 6.

Alternative animal models

Non-human primates (NHP) are perhaps the most clinically relevant experimental animal model of tuberculosis. Cynomolgus and rhesus macaques share many anatomical and physiological features with humans, are highly susceptible to *M. tuberculosis* infection and recapitulate the full spectrum of pathological and clinical manifestation as seen in humans with TB.⁶⁶ NHP models of TB have been reported for pathophysiological investigations, as well as for preclinical evaluation of vaccines and drugs.⁶⁶ More recently, the use of the common marmoset for TB modeling has been reported, with the advantage of their smaller size compared to macaques,⁶⁷ while experiments involving NHP remain extremely more expensive than experimentations involving rodents. Notably, PET/CT imaging has been successfully applied to NHP to assess bacterial loads, virulence and response to chemotherapy in the context of *M. tuberculosis* infection.⁶⁸⁻⁷⁰ PET/CT imaging typically utilizes 2-deoxy-2-[¹⁸F]fluoro-D-glucose (FDG) as contrast agent to map tuberculous lesions and this imaging technique, unlike optical imaging, is translatable to humans.²⁵

Guinea pigs are highly susceptible to *M. tuberculosis* infection and display some pathological features similar to humans, such as necrotic lesions in the lungs and disease dissemination, and have been used as experimental models of TB,⁷¹ while rabbits and rats have been much less reported.⁴¹ Finally, cattle are natural hosts of *M. bovis* and a general target and reservoir of bovine TB. Experimental infections and natural transmission studies (in the field) can be applied in this context to evaluate the efficacy of vaccines aimed at preventing TB propagation in cattle and such investigations may benefit for humans as well, thanks to the close genetic proximity of *M. bovis* and *M. tuberculosis* in the MTBC.⁴¹

IN VIVO IMAGING OF MYCOBACTERIAL INFECTIONS

Various imaging modalities have been applied to visualize bacteria and monitor microbiological events, ranging from time-lapse microscopy to follow the growth of bacteria in microfluidic devices⁷² to PET/CT imaging of tuberculous lesions and response to anti-TB treatment in living humans.²⁵ Obviously, the choice of the imaging technique depends on the subject being imaged. For instance, imaging of fluorescent mycobacteria in transparent zebrafish embryos can be performed with standard fluorescence microscopy (wide-field, confocal, light sheet, etc.) while monitoring bacterial infection in mice requires a larger setup enabling whole body imaging with high spatial and temporal precision. The depth of imaging is the major limitation for signal measurement, and detecting *M. tuberculosis* reporters deep in the lungs of an infected rodent appears more challenging than detecting a labeled subcutaneous tumor, for example. For small rodents such as mice, fluorescent and bioluminescent sources can generally be measured with optical imaging and a depth of penetration of 1-2 cm is achievable.⁷³ Importantly, quantification of a photonic signal is highly desirable to precisely correlate with the number of bacteria in the lungs of an infected mouse. For bigger animals and humans, radiolabeled probes are necessary for deep tissue imaging (PET, single photon emission CT (SPECT)) and non-optical methods are generally applied (radiography, CT, magnetic resonance imaging (MRI)). The latter have virtually no depth of penetration limit but contrast has to be optimized to distinguish different structures of interest.

Biophotonic imaging

Biophotonic imaging is a technique enabling the detection of light emanating from an organism.⁷⁴ Light is defined here as an electromagnetic radiation, situated amongst a certain portion of the electromagnetic spectrum. The wavelength of visible light roughly ranges from 400 to 700 nm. Below 400 nm, the radiation is called ultraviolet and above 700 nm infrared. Light exists as photons, which are a type of elementary particles, carrying a defined amount of energy associated with the electromagnetic radiation. *In vivo* imaging systems permit to detect and collect light arising from a source within an animal, with highly sensitive detectors such as charge-coupled device (CCD) cameras. The procedure is noninvasive and the source of the signal can be spatially located and quantified, providing real-time and quantitative information. Notably, red-shifted wavelengths are best suited for *in vivo* biophotonic imaging, as red-shifted light is less subject to scattering and absorption by mammalian tissues. The possible sources of radiation for *in vivo* optical imaging are of two types, bioluminescence or fluorescence, and are discussed further below.

Bioluminescence imaging

Bioluminescence is the emission of photons upon an enzymatic reaction catalyzed by a luciferase, involving the oxidation of a substrate (a luciferin) and generally requiring reduced flavin mononucleotide (FMNH₂) or ATP as sources of energy, and Mg²⁺ and/or O₂ as cofactors. This phenomenon is widespread in nature and genetic engineering enabled the generation of luciferase-based reporter systems in eukaryotic cells and bacteria, for *in vitro* and *in vivo* applications. The luciferases from the firefly *Photinus pyralis*, the sea pansy *Renilla reniformis*, the copepod *Gaussia princeps* and various bacteria (*Photorhabdus luminescens*, *Vibrio* and *Photobacterium* sp.) represent the common luciferases used as reporter systems.⁷⁴ More recently, the luciferase from the shrimp *Oplophorus gracilirostris* has been engineered (NanoLuc, commercialized by Promega) and highly efficient and ATP-independent bioluminescence has been reported.⁷⁵ Further improvements have been initiated with the development of different synthetic imidazo[1,2- α]pyrazines substrates, optimal for *in vivo* imaging.⁷⁶ The firefly luciferase (FFluc) is known to produce one of the most efficient reactions⁷⁷ and requires the exogenous addition of its substrate, D-luciferin, generally injected intraperitoneally in mice immediately before performing *in vivo* bioluminescence imaging. Notably, D-luciferin is not toxic for cells and mice.⁷⁴ In contrast, the *luxCDABE* operon from *P. luminescens*, encoding a luciferase heterodimer (LuxAB) and the enzymes necessary for the biosynthesis of its substrate, has been successfully cloned in heterologous bacteria, thereby generating autbioluminescent systems.⁷⁸ An optimized, red-shifted and thermostable firefly luciferase gene (*fflucRT*) has been cloned in *M. tuberculosis* and enabled *in vivo* quantification of the bacterial load in immunodeficient CB-17 SCID mice.^{51,79} The *luxCDABE* operon has been cloned in *M. tuberculosis* and applied as a marker of bacterial viability *in vitro*⁸⁰ and for quantification of the bacterial burden in mice, although not by means of whole body imaging.⁸¹ Quantitative bioluminescence imaging of *M. tuberculosis* infection *in vivo* as a method to accelerate and refine anti-mycobacterial drug assessment will be discussed in chapter 5 of this thesis.

Fluorescence imaging

Fluorescence takes place when a fluorescent compound is irradiated with light at a suitable wavelength. This triggers an electronic transition to the excited state and upon relaxation, a photon is emitted, giving rise to fluorescence.⁷⁴ As vibrational energy is lost in the process, the emitted photon is of lower energy than the exciting light and its wavelength is therefore shifted to the red (Stokes shift). Fluorescence labelling, of mycobacteria for instance, can be performed with chemical probes attached to a fluorochrome moiety or via genetic engineering and expression of genes encoding fluorescent proteins.

Chemical dyes can be used to label a specific target such as a protein or tagged protein, or nucleic acids, acidic cellular compartments and lipophilic structures such as membranes. The advantage of this approach is that many fluorochromes are commercially available and can be easily chemically coupled to other molecules to generate specific probes. As an example, we designed several fluorophore-coupled benzothiazinones to visualize their covalent target, the essential enzyme DprE1.³⁵ This enabled the polar and periplasmic localization of DprE1 to be highlighted on living, intact bacteria with fluorescence microscopy, as described in chapter 2. The further application of such probes to detect mycobacteria *in vivo* upon infection is discussed in chapter 3.

Alternatively, fluorescent proteins can be used to generate bacterial reporters. In this case, the gene encoding a fluorescent protein is cloned and transformed in bacteria. As discussed above, red-shifted light is more appropriate for *in vivo* imaging in rodents thanks to lower light scattering and absorption. Autofluorescence originating from animal tissues is also attenuated and the penetration of incident light is enhanced for red-shifted wavelengths. The wavelengths for fluorescence *in vivo* imaging are theoretically optimal in the near-infrared (NIR) range of the electromagnetic spectrum, i.e. above 700 nm. However, fluorescent protein variants derived from the well-known green fluorescent protein (GFP) from the jelly fish *Aequorea victoria* or the red fluorescent protein DsRed from the coral *Discosoma* sp. hardly reach such far-red-shifted spectral properties. Recently, a NIR fluorescent protein derived from a bacterial phytochrome and specifically engineered for *in vivo* imaging, was reported with a maximal emission at 713 nm.⁸² However, use of this protein, named iRFP, has never been reported for mycobacteria. We exploited iRFP for fluorescence *in vivo* imaging of TB infection in mice and zebrafish embryos, as described in chapter 4.

Performing *in vivo* optical imaging in mouse models of TB infection

To generate the data presented in this thesis, imaging of *M. tuberculosis*-infected mice was performed with a Photon Imager Optima (Biospace Lab, France) *in vivo* imaging platform, enabling both epi-fluorescence and luminescence imaging on the same system. This device consists of a light-tight chamber in which up to 10 mice are aligned on a heated (37°C) plate and maintained immobile through delivery of anesthetic gas (1-2% isoflurane). The detection system is composed of lenses to vary the field of view, optical cut-off filters to select the appropriate wavelength upon fluorescence imaging, and a cooled intensifier tube (photocathode) coupled to a charge-coupled device (iCCD) for signal collection. When the fluorescence modality is used, optical fibers guide the excitation light from a halogen lamp through optical filters to the sample being irradiated and “background” fluorescence, acquired with a lower excitation wavelength, is subsequently subtracted with spectral deconvolution algorithms. Image analysis with the M3

Vision software enabled the production of pictures superimposing black and white photographic images of the animals with the bioluminescent or fluorescent signal (overlaid in false colors to ease visualization) and the regional quantification of the biophotonic signal. The full system was operated in a biosafety level III (BSL3) animal facility.

RATIONALE AND THESIS OUTLINE

Since 1980, the HIV/AIDS epidemic and the emergence of MDR *M. tuberculosis* strains gave rise to a resurgence of TB incidence, mainly in low-income countries. In the absence of an effective vaccine, new and more powerful anti-tubercular agents are necessary to combat the global TB epidemic. Here, macozinone (PBTZ169) has proven to be a highly potent new antibiotic and has progressed through clinical trials since its discovery a few years ago.^{29,33} A particularity of the PBTZ169 molecule is the flexibility of the 2-substituent of the BTZ ring, enabling the linkage of different chemical groups without losing its specificity and bactericidal activity. We took advantage of this fact to attach different fluorochromes to a PBTZ moiety, thereby generating highly specific fluorescent probes that selectively target DprE1 and label BTZ-sensitive bacteria, as discussed in chapter 2. We subsequently assessed the capability of fluorescent BTZ probes to detect mycobacteria *in vivo*, for instance *M. tuberculosis* in mice and *M. marinum* in zebrafish embryos. This approach for imaging purposes is outlined in chapter 3.

In vivo imaging of *M. tuberculosis* infection permits the bacterial load to be assessed in real time and measurements can be repeated on a single group of animals, typically mice, thus reducing the number required per experiment. This is strongly encouraged by the 3R policy (refine, reduce, replace) and favors the ethical suitability regarding the utilization of laboratory animals in this context. Besides reducing the absolute number of animals required, *in vivo* imaging enables the efficacy of new anti-TB candidate compounds to be assessed much faster, which is especially important given the slow growth rate of *M. tuberculosis*. This furthermore permits a substantial gain of time and resource saving, and favors the progression of new antibiotics down the pipeline and towards the clinic. We explored these possibilities by implementing *in vivo* optical imaging for assessment of drug activity in a mouse model of TB infection. The development of NIR fluorescent mycobacterial reporters and their application for *in vivo* imaging of TB in mice is explained in chapter 4. Alternatively, although following the very same motivation, the application of bioluminescent *M. tuberculosis* strains for longitudinal treatment follow up is described in chapter 5.

The mouse model of TB infection is an unavoidable stage to test the efficacy of antibiotics *in vivo*. Since 1990, zebrafish have however become attractive animal models for biomedical research, including TB pathogenesis and drug discovery. Following the general trend of this thesis aiming at improving the anti-TB drug discovery process, we implemented the zebrafish embryo model of mycobacterial infection and optimized drug efficacy assays with this organism for several classes of novel anti-mycobacterial compounds, as discussed in chapter 6. The implementation of the zebrafish embryo model in this context follows the 3R policy by replacing the standard mouse model by a substitute.

In a nutshell, this thesis investigates alternatives to the standard techniques for *in vivo* assessment of anti-TB compounds, by implementing quantitative, longitudinal *in vivo* imaging with fluorescent BTZ-derived probes, NIR fluorescent and bioluminescent *M. tuberculosis* reporters, as well as the application of zebrafish embryos in order to accelerate and refine the anti-TB drug discovery and development process.

REFERENCES

1. WHO. *Global tuberculosis report 2018* (World Health Organisation, Geneva, 2018).
2. Koch, R. Die Ätiologie der Tuberkulose (1882) in *Robert Koch. Klassische Texte der Wissenschaft* (ed. Gradmann, C.) 113–131 (Springer Spektrum, Berlin, 2018).
3. Hershkovitz, I. *et al.* Tuberculosis origin: the Neolithic scenario. *Tuberculosis* **95 Suppl 1**, S122-126 (2015).
4. Brosch, R. & Behr, M. Comparative genomics and evolution of *Mycobacterium bovis* BCG in *Tuberculosis and the Tubercle Bacillus* (eds. Cole, S. T., Eisenach Davis, K., McMurray, D. N. & Jacobs, Jr., W. R.) 155–164 (ASM Press, Washington, DC, 2005).
5. Schatz, A., Bugle, E. & Waksman, S. A. Streptomycin, a substance exhibiting antibiotic activity against Gram-positive and Gram-negative bacteria. *Proc. Soc. Exp. Biol. Med.* **55**, 66–69 (1944).
6. WHO. *The End TB Strategy* (World Health Organisation, Geneva, 2015).
7. Cole, S. T. *et al.* Deciphering the biology of *Mycobacterium tuberculosis* from the complete genome sequence. *Nature* **393**, 537–544 (1998).
8. Gagneux, S. Host–pathogen coevolution in human tuberculosis. *Philos. Trans. R. Soc. B Biol. Sci.* **367**, 850–859 (2012).
9. Koch, A. & Mizrahi, V. *Mycobacterium tuberculosis*. *Trends Microbiol.* **26**, 555–556 (2018).
10. Pai, M. *et al.* Tuberculosis. *Nat. Rev. Dis. Primer* **2**, 16076 (2016).
11. Russell, D. G. *Mycobacterium tuberculosis* and the intimate discourse of a chronic infection. *Immunol. Rev.* **240**, 252–268 (2011).
12. Zumla, A., Raviglione, M., Hafner, R. & Fordham von Reyn, C. Tuberculosis. *N. Engl. J. Med.* **368**, 745–755 (2013).
13. Rivas-Garcia, A., Sarria-Estrada, S., Torrents-Odin, C., Casas-Gomila, L. & Franquet, E. Imaging findings of Pott’s disease. *Eur. Spine J.* **22**, 567–578 (2013).

14. WHO. *Rapid communication: key changes to treatment of multidrug- and rifampicin-resistant tuberculosis (MDR/RR-TB)* (World Health Organisation, Geneva, 2018).
15. Ma, Z., Lienhardt, C., McIlleron, H., Nunn, A. J. & Wang, X. Global tuberculosis drug development pipeline: the need and the reality. *The Lancet* **375**, 2100–2109 (2010).
16. Trunz, B. B., Fine, P. & Dye, C. Effect of BCG vaccination on childhood tuberculous meningitis and miliary tuberculosis worldwide: a meta-analysis and assessment of cost-effectiveness. *The Lancet* **367**, 1173–1180 (2006).
17. Zhu, B., Dockrell, H. M., Ottenhoff, T. H. M., Evans, T. G. & Zhang, Y. Tuberculosis vaccines: Opportunities and challenges. *Respirology* **23**, 359–368 (2018).
18. Spertini, F. *et al.* Safety of human immunisation with a live-attenuated *Mycobacterium tuberculosis* vaccine: a randomised, double-blind, controlled phase I trial. *Lancet Respir. Med.* **3**, 953–962 (2015).
19. Gengenbacher, M., Nieuwenhuizen, N. & Kaufmann, S. BCG — old workhorse, new skills. *Curr. Opin. Immunol.* **47**, 8–16 (2017).
20. Daniel, T. M. The history of tuberculosis. *Respir. Med.* **100**, 1862–1870 (2006).
21. Pai, M. *et al.* Gamma interferon release assays for detection of *Mycobacterium tuberculosis* infection. *Clin. Microbiol. Rev.* **27**, 3–20 (2014).
22. Kik, S. V., Denkinger, C. M., Chedore, P. & Pai, M. Replacing smear microscopy for the diagnosis of tuberculosis: what is the market potential? *Eur. Respir. J.* **43**, 1793–1796 (2014).
23. Steingart, K. R. *et al.* Xpert® MTB/RIF assay for pulmonary tuberculosis and rifampicin resistance in adults. *Cochrane Database Syst. Rev.* **1**, CD009593 (2014). doi:10.1002/14651858.CD009593.pub3
24. Pande, T., Pai, M., Khan, F. A. & Denkinger, C. M. Use of chest radiography in the 22 highest tuberculosis burden countries. *Eur. Respir. J.* **46**, 1816–1819 (2015).
25. Chen, R. Y. *et al.* PET/CT imaging correlates with treatment outcome in patients with multidrug-resistant tuberculosis. *Sci. Transl. Med.* **6**, 265ra166 (2014).
26. Lechartier, B., Rybniker, J., Zumla, A. & Cole, S. T. Tuberculosis drug discovery in the post-post-genomic era. *EMBO Mol. Med.* **6**, 158–168 (2014).

27. Sala, C. & Hartkoorn, R. C. Tuberculosis drugs: new candidates and how to find more. *Future Microbiol.* **6**, 617–633 (2011).
28. Manjunatha, U. H. & Smith, P. W. Perspective: Challenges and opportunities in TB drug discovery from phenotypic screening. *Bioorg. Med. Chem.* **23**, 5087–5097 (2015).
29. Makarov, V. *et al.* Benzothiazinones kill *Mycobacterium tuberculosis* by blocking arabinan synthesis. *Science* **324**, 801–804 (2009).
30. Trefzer, C. *et al.* Benzothiazinones: prodrugs that covalently modify the decaprenylphosphoryl- β -D-ribose 2'-epimerase DprE1 of *Mycobacterium tuberculosis*. *J. Am. Chem. Soc.* **132**, 13663–13665 (2010).
31. Trefzer, C. *et al.* Benzothiazinones are suicide inhibitors of mycobacterial decaprenylphosphoryl- β -D-ribofuranose 2'-oxidase DprE1. *J. Am. Chem. Soc.* **134**, 912–915 (2012).
32. Foo, C. S.-Y. *et al.* Characterization of DprE1-mediated benzothiazinone resistance in *Mycobacterium tuberculosis*. *Antimicrob. Agents Chemother.* **60**, 6451–6459 (2016).
33. Makarov, V. *et al.* Towards a new combination therapy for tuberculosis with next generation benzothiazinones. *EMBO Mol. Med.* **6**, 372–383 (2014).
34. Lechartier, B. & Cole, S. T. Mode of action of clofazimine and combination therapy with benzothiazinones against *Mycobacterium tuberculosis*. *Antimicrob. Agents Chemother.* **59**, 4457–4463 (2015).
35. Sommer, R. *et al.* Fluorescent benzothiazinone analogues efficiently and selectively label DprE1 in mycobacteria and actinobacteria. *ACS Chem. Biol.* **13**, 3184–3192 (2018).
36. Andries, K. *et al.* A diarylquinoline drug active on the ATP synthase of *Mycobacterium tuberculosis*. *Science* **307**, 223–227 (2005).
37. Mahajan, R. Bedaquiline: First FDA-approved tuberculosis drug in 40 years. *Int. J. Appl. Basic Med. Res.* **3**, 1–2 (2013).
38. Dupont, C. *et al.* Bedaquiline inhibits the ATP synthase in *Mycobacterium abscessus* and is effective in infected zebrafish. *Antimicrob. Agents Chemother.* **61**, e01225-17 (2017).

39. WHO Regional Office for South-East Asia. *Guidelines for the diagnosis, treatment and prevention of leprosy*. (World Health Organization, Regional Office for South-East Asia, 2018).
40. Van Deun, A. *et al.* Short, highly effective, and inexpensive standardized treatment of multidrug-resistant tuberculosis. *Am. J. Respir. Crit. Care Med.* **182**, 684–692 (2010).
41. Williams, A. & Orme, I. M. Animal models of tuberculosis: an overview in *Tuberculosis and the Tubercle Bacillus, Second Edition* (eds. Jacobs, Jr., William R., McShane, Helen, Mizrahi, Valerie and Orme, Ian M.) 131–142 (ASM Press, Washington, DC, 2017).
42. Orme, I. M. & Ordway, D. J. Mouse and guinea pig models of tuberculosis in *Tuberculosis and the Tubercle Bacillus, Second Edition* (eds. Jacobs, Jr., William R., McShane, Helen, Mizrahi, Valerie and Orme, Ian M.) 143–162 (ASM Press, Washington, DC, 2017).
43. Ordway, D. J. & Orme, I. M. Animal models of mycobacteria infection. *Curr. Protoc. Immunol.* **94**, 19.5.1-19.5.50 (2011).
44. Medina, E. & North, R. J. Resistance ranking of some common inbred mouse strains to *Mycobacterium tuberculosis* and relationship to major histocompatibility complex haplotype and Nramp1 genotype. *Immunology* **93**, 270–274 (1998).
45. Cooper, A. M. *et al.* Disseminated tuberculosis in interferon gamma gene-disrupted mice. *J. Exp. Med.* **178**, 2243–2247 (1993).
46. Flynn, J. L. *et al.* Tumor necrosis factor-alpha is required in the protective immune response against *Mycobacterium tuberculosis* in mice. *Immunity* **2**, 561–572 (1995).
47. Gonzalez-Juarrero, M. *et al.* Disruption of granulocyte macrophage-colony stimulating factor production in the lungs severely affects the ability of mice to control *Mycobacterium tuberculosis* infection. *J. Leukoc. Biol.* **77**, 914–922 (2005).
48. North, R. J. Importance of thymus-derived lymphocytes in cell-mediated immunity to infection. *Cell. Immunol.* **7**, 166–176 (1973).
49. Dharmadhikari, A. S. & Nardell, E. A. What animal models teach humans about tuberculosis. *Am. J. Respir. Cell Mol. Biol.* **39**, 503–508 (2008).

50. Zelmer, A. *et al.* A new *in vivo* model to test anti-tuberculosis drugs using fluorescence imaging. *J. Antimicrob. Chemother.* **67**, 1948–1960 (2012).
51. Andreu, N. *et al.* Rapid *in vivo* assessment of drug efficacy against *Mycobacterium tuberculosis* using an improved firefly luciferase. *J. Antimicrob. Chemother.* **68**, 2118–2127 (2013).
52. van Leeuwen, L. M., van der Sar, A. M. & Bitter, W. Animal models of tuberculosis: zebrafish. *Cold Spring Harb. Perspect. Med.* **5**, a018580 (2014).
53. Renshaw, S. A. & Trede, N. S. A model 450 million years in the making: zebrafish and vertebrate immunity. *Dis. Model. Mech.* **5**, 38–47 (2012).
54. Davis, J. M. *et al.* Real-time visualization of mycobacterium-macrophage interactions leading to initiation of granuloma formation in zebrafish embryos. *Immunity* **17**, 693–702 (2002).
55. Ramakrishnan, L. Looking within the zebrafish to understand the tuberculous granuloma. *Adv. Exp. Med. Biol.* **783**, 251–266 (2013).
56. Clay, H. *et al.* Dichotomous role of the macrophage in early *Mycobacterium marinum* infection of the zebrafish. *Cell Host Microbe* **2**, 29–39 (2007).
57. Meijer, A. H. *et al.* Identification and real-time imaging of a myc-expressing neutrophil population involved in inflammation and mycobacterial granuloma formation in zebrafish. *Dev. Comp. Immunol.* **32**, 36–49 (2008).
58. Yang, C.-T. *et al.* Neutrophils exert protection in the early tuberculous granuloma by oxidative killing of mycobacteria phagocytosed from infected macrophages. *Cell Host Microbe* **12**, 301–312 (2012).
59. Stoop, E. J. M. *et al.* Zebrafish embryo screen for mycobacterial genes involved in the initiation of granuloma formation reveals a newly identified ESX-1 component. *Dis. Model. Mech.* **4**, 526–536 (2011).
60. Phan, T. H. *et al.* EspH is a hypervirulence factor for *Mycobacterium marinum* and essential for the secretion of the ESX-1 substrates EspE and EspF. *PLoS Pathog.* **14**, e1007247 (2018).

61. Stoop, E. J. M. *et al.* Mannan core branching of lipo(arabino)mannan is required for mycobacterial virulence in the context of innate immunity. *Cell. Microbiol.* **15**, 2093–2108 (2013).
62. van der Woude, A. D. *et al.* Analysis of SecA2-dependent substrates in *Mycobacterium marinum* identifies protein kinase G (PknG) as a virulence effector. *Cell. Microbiol.* **16**, 280–295 (2014).
63. Takaki, K., Davis, J. M., Winglee, K. & Ramakrishnan, L. Evaluation of the pathogenesis and treatment of *Mycobacterium marinum* infection in zebrafish. *Nat. Protoc.* **8**, 1114–1124 (2013).
64. Takaki, K., Cosma, C. L., Troll, M. A. & Ramakrishnan, L. An *in vivo* platform for rapid high-throughput antitubercular drug discovery. *Cell Rep.* **2**, 175–184 (2012).
65. Adams, K. N. *et al.* Drug tolerance in replicating mycobacteria mediated by a macrophage-induced efflux mechanism. *Cell* **145**, 39–53 (2011).
66. Peña, J. C. & Ho, W.-Z. Non-human primate models of tuberculosis in *Tuberculosis and the Tubercle Bacillus, Second Edition* (eds. Jacobs, Jr., William R., McShane, Helen, Mizrahi, Valerie and Orme, Ian M.) 163–176 (ASM Press, Washington, DC, 2017).
67. Scanga, C. A. & Flynn, J. L. Modeling tuberculosis in nonhuman primates. *Cold Spring Harb. Perspect. Med.* **4**, a018564 (2014).
68. Via, L. E. *et al.* Differential virulence and disease progression following *Mycobacterium tuberculosis* complex infection of the common marmoset (*Callithrix jacchus*). *Infect. Immun.* **81**, 2909–2919 (2013).
69. Lin, P. L. *et al.* Radiologic responses in cynomolgus macaques for assessing tuberculosis chemotherapy regimens. *Antimicrob. Agents Chemother.* **57**, 4237–4244 (2013).
70. Coleman, M. T. *et al.* PET/CT imaging reveals a therapeutic response to oxazolidinones in macaques and humans with tuberculosis. *Sci. Transl. Med.* **6**, 265ra167 (2014).
71. McMurray, D. N., Collins, F. M., Dannenberg, A. M. & Smith, D. W. Pathogenesis of experimental tuberculosis in animal models in *Tuberculosis* (ed. Shinnick, T. M.) 157–179 (Springer Spektrum, Berlin, 1996).

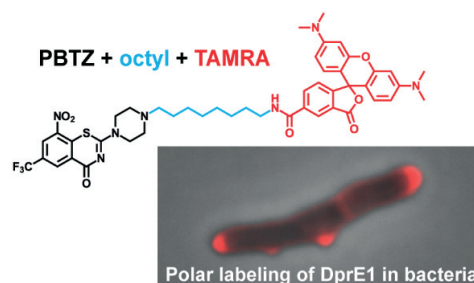
72. Wakamoto, Y. *et al.* Dynamic persistence of antibiotic-stressed mycobacteria. *Science* **339**, 91–95 (2013).
73. Andreu, N., Elkington, P. T. & Wiles, S. Molecular imaging in TB: from the bench to the clinic in *Understanding Tuberculosis - Global Experiences and Innovative Approaches to the Diagnosis* (ed. Cardona, Pere-Joan). 307–332 (INTECH, 2012). doi:10.5772/30595
74. Andreu, N., Zelmer, A. & Wiles, S. Noninvasive biophotonic imaging for studies of infectious disease. *FEMS Microbiol. Rev.* **35**, 360–394 (2011).
75. Hall, M. P. *et al.* Engineered luciferase reporter from a deep sea shrimp utilizing a novel imidazopyrazinone substrate. *ACS Chem. Biol.* **7**, 1848–1857 (2012).
76. Coutant, E. P. & Janin, Y. L. Synthetic routes to coelenterazine and other imidazo[1,2- α]pyrazin-3-one luciferins: essential tools for bioluminescence-based investigations. *Chem. Eur. J.* **21**, 17158–17171 (2015).
77. Ando, Y. *et al.* Firefly bioluminescence quantum yield and colour change by pH-sensitive green emission. *Nat. Photonics* **2**, 44–47 (2008).
78. Craney, A. *et al.* A synthetic *luxCDABE* gene cluster optimized for expression in high-GC bacteria. *Nucleic Acids Res.* **35**, e46 (2007).
79. Andreu, N. *et al.* Optimisation of bioluminescent reporters for use with mycobacteria. *Plos One* **5**, e10777 (2010).
80. Sharma, S. *et al.* Simple and rapid method to determine antimycobacterial potency of compounds by using autoluminescent *Mycobacterium tuberculosis*. *Antimicrob. Agents Chemother.* **58**, 5801–5808 (2014).
81. Zhang, T., Li, S.-Y. & Nuermberger, E. L. Autoluminescent *Mycobacterium tuberculosis* for rapid, real-time, non-invasive assessment of drug and vaccine efficacy. *Plos One* **7**, e29774 (2012).
82. Filonov, G. S. *et al.* Bright and stable near-infrared fluorescent protein for *in vivo* imaging. *Nat. Biotechnol.* **29**, 757–761 (2011).

PART I

FLUORESCENT BENZOTHIAZINONES

Chapter 2.

Fluorescent Benzothiazinone Analogues Efficiently and Selectively Label DprE1 in Mycobacteria and Actinobacteria



This chapter is a post-print version of an article published in ACS Chemical Biology as:

Sommer, R., Neres, J., Piton, J., Dhar, N., van der Sar, A., Mukherjee, R., Laroche, T., Dyson, P. J., McKinney, J. D., Bitter, W., Makarov, V., and Cole, S. T. Fluorescent Benzothiazinone Analogues Efficiently and Selectively Label DprE1 in Mycobacteria and Actinobacteria. *ACS Chem. Biol.* **13**, 3184–92 (2018). DOI: [10.1021/acscchembio.8b00790](https://doi.org/10.1021/acscchembio.8b00790)

Contributions: optimization of staining procedures on live bacteria, microscopy (wide field, high resolution, super-resolution), image analysis and figure construction, MICs, generation of BTZ-resistant mutants, *in vivo* staining on infected zebrafish embryos and mice (unpublished data).

ABSTRACT

Benzothiazinones (BTZ) are highly potent bactericidal inhibitors of mycobacteria and the lead compound, BTZ043, and the optimized drug candidate, PBTZ169, have potential for the treatment of tuberculosis. Here, we exploited the tractability of the BTZ scaffold by attaching a range of fluorophores to the 2-substituent of the BTZ ring via short linkers. We show by means of fluorescence imaging that the most advanced derivative, **JN108**, is capable of efficiently labeling its target, the essential flavoenzyme DprE1, both in cell-free extracts and after purification as well as in growing cells of different actinobacterial species. DprE1 displays a polar localization in *Mycobacterium tuberculosis*, *M. marinum*, *M. smegmatis*, and *Nocardia farcinica* but not in *Corynebacterium glutamicum*. Finally, mutation of the cysteine residue in DprE1 in these species, to which BTZ covalently binds, abolishes completely the interaction with **JN108**, thereby highlighting the specificity of this fluorescent probe.

INTRODUCTION

Tuberculosis (TB), an infectious disease caused by *Mycobacterium tuberculosis*, has reemerged in recent decades as an important global health problem and was responsible for 1.8 million deaths in 2015.^{1,2} The main reasons for this alarming situation are the appearance of multidrug-resistant (MDR-TB) and extensively drug-resistant (XDR-TB) strains with high mortality rates, the synergy with the HIV/AIDS pandemic, and increased poverty.²⁻⁴ The fruits of substantially increased investment in the research on novel anti-TB drugs in the past decade led to replenishment of the drug discovery pipeline with drug candidates in different stages of development.^{5,6} Among these novel, promising anti-TB drugs are the 8-nitro-benzothiazinones (BTZs) BTZ043 with an MIC₉₉ of 1 ng/mL (Figure 1) and PBTZ169, an improved BTZ analogue with an even lower MIC₉₉ against *M. tuberculosis* (0.3 ng/mL) and improved solubility, which is currently in clinical trials.^{7,8} The BTZs are among the most potent antitubercular agents known to date and act by inhibiting the enzyme decaprenyl-phospho- β -D-ribose oxidase (DprE1), which is one of the most attractive targets for anti-TB drug discovery.^{8,9} DprE1 and DprE2 (decaprenylphosphoryl-D-2-keto erythro pentose reductase) catalyze the epimerization of decaprenylphosphoryl- β -D-ribose (DPR) to its arabinose isomer DPA. DPA is the sole donor of arabinose sugars that are essential for cell wall biosynthesis in *M. tuberculosis*.¹⁰

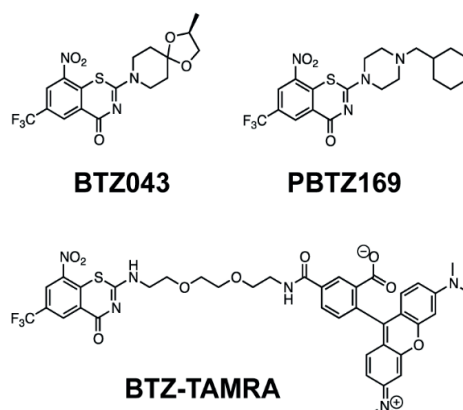


Figure 1. Structures of BTZ043, PBTZ169 and BTZ-TAMRA.

BTZs are suicide inhibitors of DprE1, selectively forming irreversible covalent adducts with Cys387 in the active site of this enzyme, as previously demonstrated by biochemical and structural methods.^{11,12} A nitroso species is produced by nitroreduction, and this reacts with the thiol side chain of Cys387 to form a semimercaptal covalent adduct with DprE1. The nitro group of the BTZs is crucial for their mechanism of inhibition, as its replacement by amine, hydroxylamine, pyrrole, or many other functional groups invariably led to near complete loss of antimycobacterial activity.^{8,12,13}

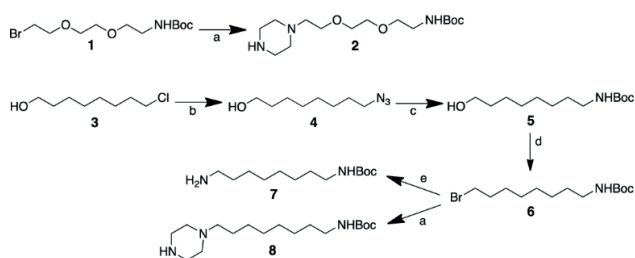
We recently showed that a fluorescently labeled BTZ analogue (BTZ-TAMRA, Figure 1) retained modest antimycobacterial activity ($MIC_{99} = 6 \mu\text{g/mL}$) and selectively labeled the poles of *M. tuberculosis in vitro* as observed by fluorescence microscopy, pointing to a polar localization of DprE1 in mycobacteria.¹¹ Given these results, we investigated the SAR of the fluorescently labeled BTZs further to improve their antimycobacterial activity and explore their potential as imaging agents for *in vitro* and *in vivo* studies with actinobacteria. Here, we report the development of a highly active and selective fluorescent BTZ analogue that covalently labels DprE1 and its application for imaging purposes. We exploited its properties to visualize the subcellular localization of DprE1 in several BTZ-sensitive actinobacteria and track the behavior of mycobacteria in time-lapse fluorescence microscopy.

RESULTS AND DISCUSSION

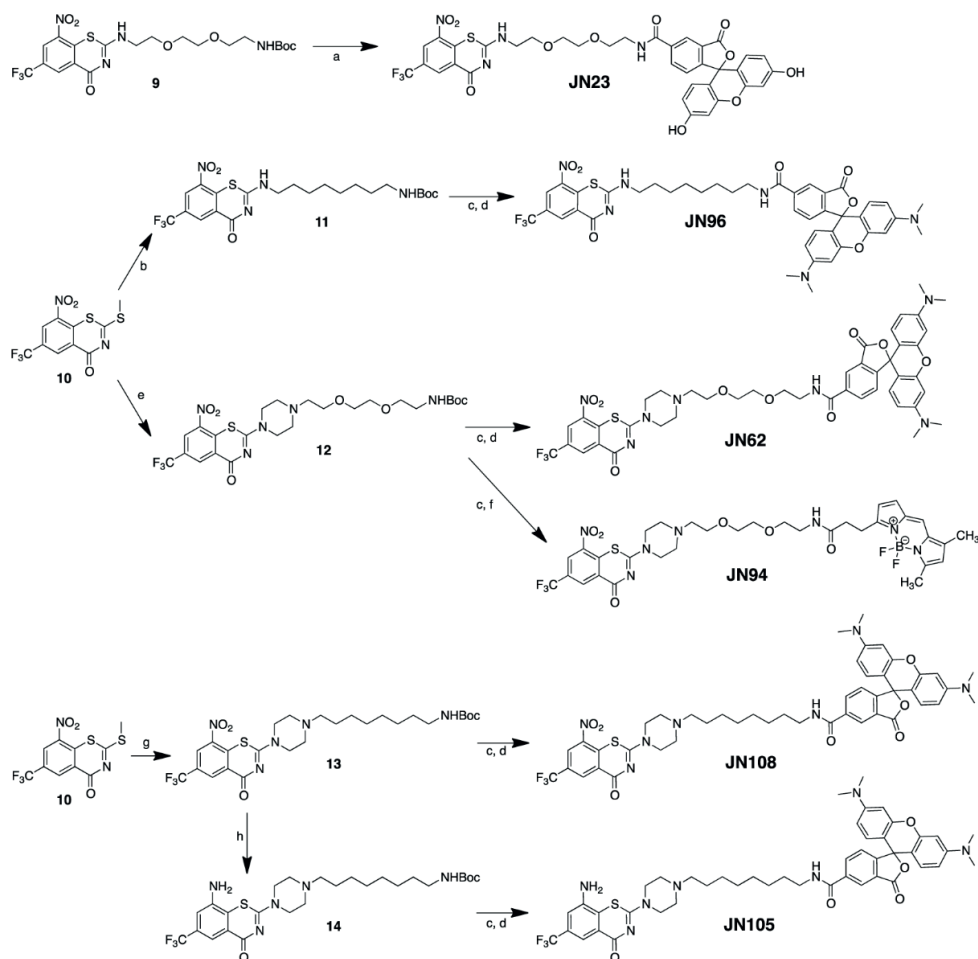
Design and Synthesis of Fluorescent BTZ Analogues

The first fluorescent BTZ synthesized, BTZ-TAMRA, showed a promising MIC₉₉ of 6 µg/mL against *M. tuberculosis*¹¹ and was used as a starting point for further optimization. Previously reported SAR studies on the BTZ and PBTZ series of DprE1 inhibitors showed that when the 8-nitro-6-trifluoromethylbenzothiazinone core was conserved, the moiety on position 2 could accommodate a range of substituents retaining or even improving the MIC₉₉ against *M. tuberculosis*.^{7,8,14,15} The crystal structures of DprE1 in complex with BTZ043 and PBTZ169 provided further insight into the SAR results, as the BTZ core is located inside the active site forming a covalent bond with Cys387, but the 2-substituent of the BTZ ring is on the protein surface and makes few interactions with DprE1 residues.^{7,11} This explains how the presence of a tri-PEG linker between the BTZ core and the bulky fluorophore in BTZ-TAMRA provided enough space to allow correct binding.

We designed six new fluorescent BTZ and PBTZ analogues testing different fluorophores and spacers. The synthesis of the required tri-PEG and octyl linkers was performed through the synthetic route shown in Scheme 1, following published procedures. 2-(2-(2-Chloroethoxy)ethoxy)ethanol or 8-chlorooctan-1-ol (**3**) were converted to the respective azides, which were reduced with triphenylphosphine to the respective amines. The amines were Boc-protected and the respective alcohol groups converted to the bromides **1** and **6**. The Boc-protected linkers were then reacted with piperazine forming the required Boc-protected piperazine-linkers **2** and **8** for subsequent coupling to form the PBTZ-linker molecules. In addition, the Boc-protected 8-bromo-octylamine **6** was converted to Boc-protected 8-amino-octylamine **7** to synthesize the alkyl linker version of BTZ-TAMRA.



Scheme 1. Synthesis of linkers. (a) Piperazine, EtOH, 60 °C, NaN₃; (b) DMF, 100 °C; (c) (1) PPh₃, H₂O, THF, rt, (2) Boc₂O, NaOH, ACN, H₂O; (d) CBr₄, K₂CO₃, PPh₃, DCM, rt; (e) NH₃, H₂O, DME, 75 °C.



Scheme 2. Synthesis of fluorescent BTZ analogues. (a) 5-Carboxyfluorescein NHS ester, DIPEA, DMF, rt; (b) compound **7**, EtOH, 50 °C; (c) TFA, DCF, rt; (d) 5-carboxy-TAMRA NHS ester, DIPEA, DMF, rt; (e) compound **5**, EtOH, 50 °C; (f) BODIPY-FL NHS ester, DIPEA, DMF, rt; (g) compound **8**, EtOH, 50 °C; (h) NH₄Cl, NaHS, EtOH, H₂O, rt.

The fluorescein analogue of BTZ-TAMRA was synthesized from intermediate **9** (previously described¹¹) by coupling with the NHS ester of 5-carboxyfluorescein, affording **JN23** (Scheme 2). The synthesis of the remaining analogues was started by coupling the key 3-methylthio-benzothiazinone intermediate **10**¹⁶ with each of the linkers described above, providing the Boc-protected intermediates **11**, **12** and **13**. Boc hydrolysis, followed by coupling with the desired fluorophore NHS esters in the presence of diisopropylethylamine, afforded the final compounds **JN96**, **JN62**, **JN94**, and **JN108**. To obtain the 8-amine version of **JN108**, the 8-nitro group of intermediate **13** was reduced using sodium hydrosulfite to give compound **14**, which was then subjected to Boc hydrolysis and coupling with the NHS ester of 5-carboxy-TAMRA, to afford **JN105**. The propyl-TAMRA control compound **JN111** was prepared by coupling *n*-propylamine with the NHS ester of 5-carboxy-TAMRA.

Antimycobacterial Activity of Novel Fluorescent BTZs

The antimycobacterial potency of the various fluorescent BTZ analogues synthesized was evaluated using the standard REMA assay (Table 1). The data show that fluorescein-labeled **JN23** was inactive against both *M. tuberculosis* and *M. smegmatis*, in contrast to its TAMRA-labeled BTZ-TAMRA analogue. Therefore, further SAR was mostly focused on TAMRA-labeled analogues. A BTZ-TAMRA analogue with a hydrophobic octyl linker (**JN96**), prepared to assess the influence of the spacer hydrophobicity on the antimycobacterial activity, presented a *M. tuberculosis* MIC₉₉ 25-fold lower than that of BTZ-TAMRA. Similarly, the compound **JN108** with an octyl linker between a PBTZ core and TAMRA had an MIC₉₉ against *M. tuberculosis* 400-fold lower than **JN62**, the PBTZ analogue with a tri-PEG linker. **JN108** also presented an MIC₉₉ fourfold lower than its simpler BTZ analogue **JN96**. The smaller BODIPY-FL fluorophore was also evaluated in compound **JN94** and led to a fourfold improvement in potency when compared to its TAMRA analogue **JN62**. Compound **JN105**, an 8-amino version of the PBTZ-TAMRA compound **JN108**, was 100-fold less potent (MIC₉₉ 6.2 µg/mL) than the latter, as expected (Table 1). Compounds **JN105**, the inactive NH₂-derivative of **JN108**, and **JN111**, a propyl-TAMRA analogue inactive against mycobacteria, were synthesized for use as negative controls to assess the possible effect of nonspecific binding. From the SAR studies, **JN108** was the best fluorescently labeled BTZ analogue, and this was confirmed in further work, described below.

	MIC ₉₉ (μg/mL)		
	<i>M. tuberculosis</i> H37Rv	<i>M. smegmatis</i> mc ² 155	<i>M. marinum</i> E11
BTZ-TAMRA	6.2	50	ND
JN23	>50	>50	40
JN62	25	>50	>50
JN94	6.2	6.2	ND
JN96	0.25	0.75	3.5
JN108	0.06	0.08	0.1
JN105	6.2	12.5	>25
JN111	>50	>50	ND

Table 1. Minimum inhibitory concentrations of fluorescent BTZs against mycobacteria.
ND: not determined.

***In vitro* Labeling of Recombinant DprE1**

Our previous study reported successful covalent labeling of recombinant *M. smegmatis* DprE1 by a BODIPY-X labeled BTZ.¹² Using a similar strategy, we tested the new fluorescent BTZs synthesized here for their ability to label recombinant *M. tuberculosis* DprE1, produced as described elsewhere,¹⁷ and analyzed the reaction products by SDS-PAGE and fluorescence scanning. Both the fluorescein- and TAMRA-labeled BTZ analogues bound to DprE1 irrespective of the linker used in their construction. All the nitro-BTZ fluorescent derivatives (**JN23**, **JN94**, **JN29**, **JN62**, **JN96**, and **JN108**) bound strongly to purified DprE1 (Figure 2). **JN29**, **JN62**, **JN96**, and **JN108** were detected in the TAMRA channel, whereas **JN23** and **JN94** were detected in the fluorescein channel. The noncovalent fluorescent BTZ derivative, **JN105**, with an amino instead of the nitro group, bound much less strongly, as did **JN111**, a propyl-TAMRA derivative lacking the BTZ pharmacophore. Similarly, very weak labeling was seen when DprE1 was inactivated by heating for 10 min at 95 °C before adding **JN108** to the reaction, most likely due to nonspecific binding. Likewise, labeling was abolished when the reducing agent DTT was included. These findings are consistent with the known mechanism of action of the BTZ^{12,18} and suggest that the lack of antimycobacterial activity of several derivatives, such as **JN62**, may be due to its inability to reach DprE1 in the periplasm.¹⁹

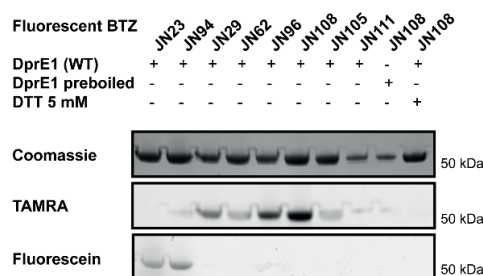


Figure 2. Labeling purified DprE1 with different fluorescent BTZ derivatives. The reactions were performed as outlined in the Methods section and contained recombinant wild-type (WT) DprE1, boiled DprE1, DTT, and the fluorescent BTZ derivatives indicated at top. After SDS-PAGE electrophoresis, the gels were Coomassie blue stained (top panel), scanned using the TAMRA channel (excitation 523 nm/emission 580 nm, middle panel) of the Typhoon scanner, or scanned in the fluorescein channel (excitation 488 nm/emission 520 nm, lower panel). The size of the bands is about 50 kDa.

Labeling of DprE1 in *M. tuberculosis* Cell-Free Extracts

To further investigate the interaction of **JN108** with its target DprE1 and to assess the extent of binding to other proteins in *M. tuberculosis*, **JN108** was incubated with cell-free extracts and then analyzed by SDS-PAGE and fluorescence scanning. Because DprE1 is not an abundant protein, in most but not all cases the extracts were supplemented with purified DprE1 or with its variants, in which Cys387 had been replaced by Ser or Gly.²⁰ As can be seen from Figure 3, in addition to DprE1, **JN108** only labeled two highly *M. tuberculosis* abundant proteins with apparent molecular weights of 60 and 15 kDa. The 15 kDa band was identified by mass spectrometry as GroES. The signal strength of the target-specific labeling was proportional to the amount of DprE1 present, and the enzyme could be detected at 0.5 μ M but not at 0.1 μ M. No labeling occurred when BTZ-resistant DprE1 variants were used bearing C387S or C387G substitutions and, again, this is consistent with the mechanism of action of BTZ and with prior findings.^{7,8,11,20}

Exploring Human Hepatocyte Extracts

To establish whether **JN108** could label any human proteins the compound was incubated with an extract of the human hepatocyte cell line HepG2 supplemented with or without DprE1. From Figure 3 it is apparent that no labeling of human proteins was observed whereas DprE1 was once again detectable at the 0.5 μ M level. The combined results indicate that if off-target covalent labeling of human proteins occurs it must be below the limit of detection of this assay.

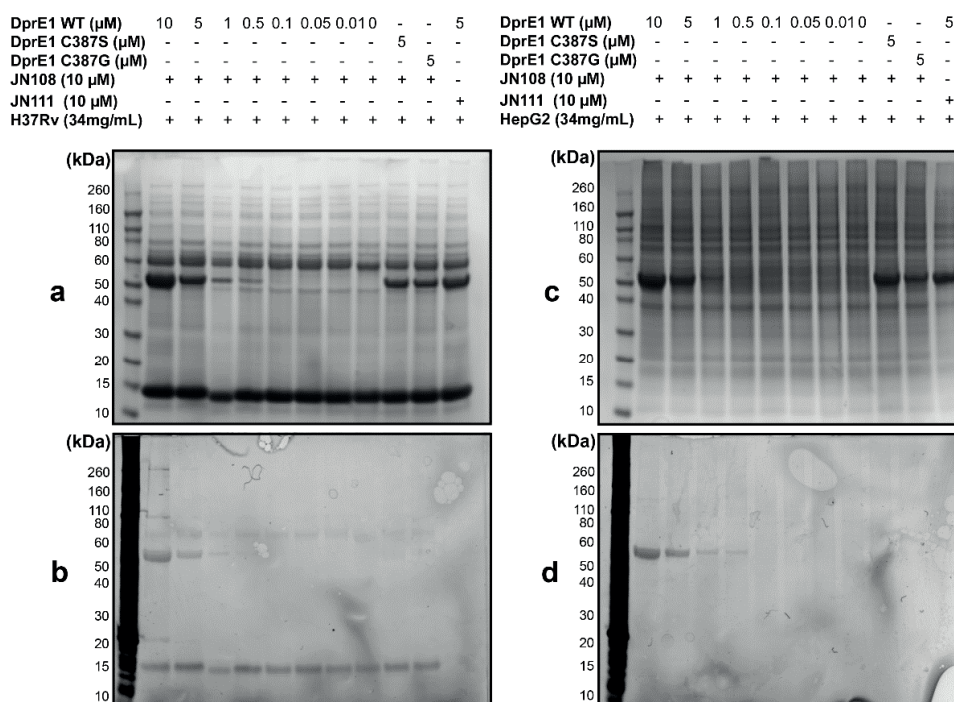


Figure 3. Labeling cell-free extracts of *M. tuberculosis* (a, b) or HepG2 (c, d) cells with **JN108**. The reactions were performed as outlined in the Methods section and contained **JN108**, **JN111**, or the DprE1 enzymes, as indicated at top. After SDS-PAGE electrophoresis the gels were (a, c) Coomassie blue stained and (b, d) scanned using the TAMRA channel.

Single Cell Analysis and Labeling of Living Mycobacteria

To visualize the effect and specificity of fluorescently labeled BTZ-derivatives on mycobacteria in real time, *M. smegmatis* cells constitutively expressing GFP were grown in a microfluidic device and monitored using time-lapse microscopy.²¹ The culture medium was supplemented with either 700 ng/mL **JN108** or its inactive NH_2 -derivative (**JN105**, 700 ng/mL), and the results were compared. When **JN105** was used, no growth inhibition was observed, and all bacterial cells were weakly stained on the surface although the stain could be removed by flowing **JN105**-free 7H9 medium through the device (Supplementary Figure 1a and Supplementary Movie 2). By contrast, when **JN108** was employed growth ceased within a few hours of exposure, and polar localization of the fluorophore was clearly visible in most of the cells (Supplementary Figure 1a and Supplementary Movie 1). On continuing exposure to **JN108**, some cells started to lyse (indicated by loss of GFP signal), and some cells started leaking cellular material, which was also stained with the fluorophore.

Similar staining was also performed using *M. tuberculosis* cells constitutively expressing GFP protein. Bacteria that were grown in a microfluidic device were exposed to either **JN105** or **JN108** (400 ng/mL), and staining was monitored by time-lapse microscopy. As was seen in the case of *M. smegmatis*, the active derivative, **JN108**, exhibited clear polar localization with a large fraction of the cells subsequently lysing (Supplementary Figure 1b and Supplementary Movie 3). In contrast, when exposed to **JN105**, most of the cells exhibited faint staining of the whole cell surface, which was probably indicative of nonspecific binding (Supplementary Figure 1b).

Subcellular Localization of DprE1

The Wag31-GFP fusion protein is an additional independent marker for the poles of *M. smegmatis*.²² When **JN108** was used to stain DprE1 in this bacterium, strong colocalization of the GFP and TAMRA signals could be observed at the poles using high-resolution microscopy (Supplementary Figure 2). When the Rv3789-GFP fusion protein²³ was used to label the plasma membrane of *M. smegmatis* or *M. marinum*, **JN108** also displayed bright foci at the poles of the bacilli and beyond the GFP-labeled membrane, indicating that the localization of DprE1 is similar in *M. smegmatis* and *M. marinum* (Figures 4a and b, Supplementary Figure 3a). Structured illumination microscopy (SIM) with **JN108**-stained *M. smegmatis* confirmed these previous observations at the super-resolution level (Figures 4a and b).

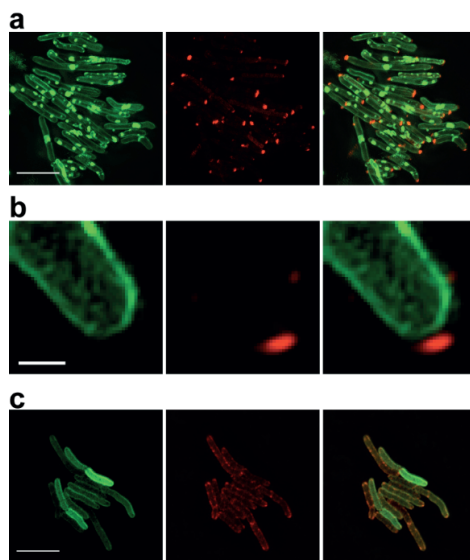


Figure 4. SIM imaging of *M. smegmatis* producing Rv3789-GFP (membrane, green channel) stained with **JN108** (red channel). (a) BTZ-sensitive bacteria stained with **JN108** show bright spots at their tips in the red channel. (b) Magnification of the tip on a single cell from panel a showing **JN108**-stained DprE1 beyond the membrane. (c) BTZ-resistant bacteria bearing a C394S mutation in DprE1 display only background staining when exposed to **JN108**, but no polar foci are observed. Scale bars: 5 μ m in panels a and c, 500 nm in panel b.

Labeling Other Actinobacteria

Many actinobacteria are susceptible to BTZ, including certain species of the genera *Corynebacterium* and *Nocardia*.^{8,24} This prompted us to investigate whether DprE1 could also be localized with **JN108** at the poles of species from these genera. The MIC₉₉ of *N. farcinica* for **JN108** was evaluated at 0.01 µg/mL by standard REMA techniques, confirming its general susceptibility to benzothiazinones. On staining *N. farcinica* with **JN108** bright foci were visible at the poles of the cells and at the branching points, which are characteristic of *Nocardia* spp., thereby suggesting that DprE1 plays a role during tip extension not only at the poles of bacilli but also at budding locations in branching bacteria (Figure 5a).

The MIC₉₉ of *C. glutamicum* for **JN108** was found to be 1.1 µg/mL. A mixture of *M. smegmatis* expressing a GFP-labeled membrane protein²³ and *C. glutamicum* was incubated with **JN108** and examined by wide field fluorescence microscopy. In this experiment, polar labeling of *M. smegmatis* was seen, as expected, but *C. glutamicum* cells appeared to be uniformly labeled suggesting that, unlike mycobacteria, DprE1 is not located at the poles (Figure 5b). To determine whether this result was a general property of *Corynebacteria* spp., we repeated the experiment using *Corynebacterium diphtheriae* and again observed that **JN108** stained cells uniformly (data not shown). Thus, for *Mycobacterium* and *Nocardia* spp. but not for *Corynebacterium* spp., the localization of DprE1 indicated by **JN108** staining coincides with the sites of cell wall synthesis, as can be observed by nascent peptidoglycan staining (Supplementary Figure 4). Interestingly, when **JN108** staining was performed on nonreplicating, streptomycin-starved *M. tuberculosis* 18b (SS18b), a model system for latent TB,^{25,26} polar labeling could still be observed (Supplementary Figure 5). Since SS18b is not susceptible to BTZ, nor to other mycobacterial cell wall inhibitors, this suggests that **JN108** can still interact with its target, DprE1, in nonreplicating cells and that in growing mycobacteria the bactericidal effect follows this interaction.

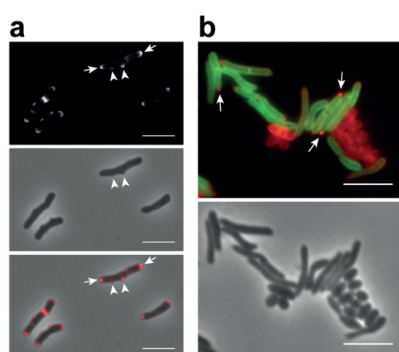


Figure 5. Labeling whole cells of *N. farcinica*, *M. smegmatis*, and *C. glutamicum* with **JN108**. (a) Staining of *N. farcinica* with **JN108** localizes DprE1 at the poles of the cells and at nascent branching points. Top panel, TAMRA channel fluorescence image of **JN108**-labeled *N. farcinica*. Middle panel, corresponding phase contrast image. Lower panel, merged channels. Arrows indicate the polar localization of the TAMRA signal, and the arrowheads show foci at nascent branching points. (b) Staining of a mixture of *M. smegmatis* and *C. glutamicum* with **JN108**. The top panel shows the fluorescence image, and the lower panel is the corresponding phase contrast micrograph. Arrows indicate polar localization of DprE1 in *M. smegmatis* expressing GFP-labeled membrane protein Rv3789, whereas no such polar labeling was seen with *C. glutamicum*. Scale bars: 5 µm.

BTZ-Resistant Bacteria Do Not Display Polar Labeling

The mechanism of action of BTZ and PBTZ involves the covalent binding of the drug to a conserved cysteine in the substrate-binding site of DprE1.^{11,12} *In vitro*, mutated versions of the enzyme were not labeled by **JN108** (Figure 3), and we sought to validate that the same happens when staining living bacteria. BTZ-resistant mutants of *M. tuberculosis* and *M. smegmatis* were previously described.⁸ Spontaneous BTZ-resistant mutants of *M. marinum* and *N. farcinica* were selected on 7H10 medium containing 300 ng/mL or 1 µg/mL PBTZ169, respectively. The presence of the mutations C389S and C419S in DprE1 were confirmed by PCR sequencing of *mmar5352* and *nfa1970*, the *dprE1* orthologues in *M. marinum* and *N. farcinica*, respectively. MICs for PBTZ169 were >1000 and >10 000 ng/mL for resistant *M. marinum* and *N. farcinica*, respectively, while the BTZ-sensitive parent strains had MICs of 0.3 and 0.6 ng/mL. As expected, **JN108** staining of the BTZ-resistant *N. farcinica* did not display polar localization but only a faint background (Figure 6). Similarly, BTZ-resistant *M. smegmatis* (Figure 4c), *M. marinum* (Supplementary Figure 3b), and *M. tuberculosis* (Supplementary Figure 6) do not display polar foci, unlike their wild-type counterparts. This confirms that labeling by **JN108** in all the tested actinobacterial species is highly specific for DprE1 and follows the same mode of action as benzothiazinone-based antimycobacterials.

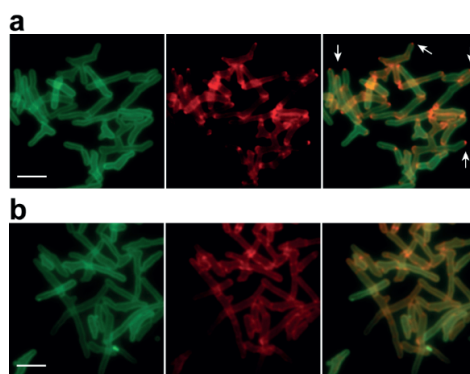


Figure 6. Labeling *N. farcinica* carrying Rv3789-mNeonGreen as a membrane marker. (a) BTZ-sensitive bacteria show polar DprE1 labeling (arrows). (b) BTZ-resistant bacteria do not display polar labeling but only faint background staining. The left panel shows fluorescence in the green channel (membrane); the middle panel shows red fluorescence (**JN108**), and the right panel is a merge of the green and red channels. Scale bars: 5 µm.

CONCLUDING REMARKS

Here, we exploited the tractability of the 2-substituent of the BTZ and PBTZ scaffolds to attach a range of fluorophores via an alkyl linker, thereby creating tool compounds for detecting mycobacteria in different settings. We demonstrate that the most advanced derivative, **JN108**, which is TAMRA-labeled, retains significant antimycobacterial activity and can efficiently label its target DprE1 *in vitro* and at the poles of live mycobacteria in culture. The high specificity of **JN108** is confirmed by the absence of labeling on BTZ-resistant mutant bacteria carrying Cys → Ser mutation in DprE1. This exciting result shows the potential of fluorescent PBTZ analogues to detect mycobacteria in more complex settings, such as for *in vivo* imaging. We are currently exploring these avenues with **JN108** in the zebrafish model of mycobacterial infection and plan to evaluate additional **JN108** analogues with near-infrared range (NIR) fluorophores for their ability to detect *M. tuberculosis* in infected mice by *in vivo* imaging techniques. Although BTZ-derived probes display weak bactericidal activity on BTZ-sensitive bacteria that might limit precise quantitative applications, they nonetheless have the potential to detect *M. tuberculosis* in infected tissues or in sputum samples.

METHODS

Chemistry: General Methods and Materials

All commercial reagents (Sigma-Aldrich, Acros, Alfa-Aesar) were used as provided. All reactions were performed under an inert atmosphere of dry N₂ in oven-dried (150 °C) glassware. Column chromatography was performed with a Varian 971-FP Flash purification system with prepacked silica gel cartridges supplied by Luknova, with the indicated solvent system. ¹H and ¹³C NMR spectra were recorded on Bruker Avance 400 MHz spectrometer. ¹H chemical shifts are reported in ppm from an internal standard of residual chloroform (7.26 ppm) or methanol (3.31 ppm), and ¹³C chemical shifts are reported using an internal standard of residual chloroform (77.1 ppm), or methanol (49.0 ppm). Proton chemical data are reported as follows: chemical shift, multiplicity (s = singlet, d = doublet, t = triplet, m = multiplet, br = broad), coupling constant, and integration. High-resolution mass spectra were obtained on a Waters Q-TOF Ultima instrument equipped with an ESI interface. Details of the synthetic routes used to produce the compounds outlined in Schemes 1 and 2 are given in the Supporting Information.

Bacterial Strains, Cell Lines, Cell Extracts, and Culture Conditions

All mycobacterial strains, BTZ-resistant mycobacterial mutants, and *M. tuberculosis* strain H37Rv were grown at 37 °C with shaking in Middlebrook 7H9 (Difco) broth supplemented with 10% albumin–dextrose–catalase (ADC) enrichment, 0.2% glycerol, and 0.05% Tween 80. *M. marinum* strains E11 and M were grown in the same medium at 30 °C. *C. glutamicum* (ATCC13032) and *N. farcinica* (ATCC3318) were grown in brain–heart infusion medium (Difco) at 30 °C. Plasmids based on *mNeonGreen*^{27,28} were constructed by PCR amplification and subcloning in appropriate vectors. DNA was transformed in competent bacteria by electroporation. To prepare proteins, H37Rv was grown and processed as described previously.²⁹ Briefly, cell lysates were prepared by resuspending cell pellets in lysis buffer (PBS containing Roche protease inhibitor cocktail tablets), bead-beating with 100 µm glass beads, and were then clarified by centrifugation. The human hepatocyte cell line HepG2 was grown in DMEM medium supplemented with fetal bovine serum (heat inactivated). After trypsin–EDTA treatment, ~10⁸ cells were lysed by bead-beating, and the extract was clarified by centrifugation. Protein concentrations were determined using the bicinchoninic acid (BCA) assay (Pierce BCA protein assay kit; Thermo Scientific).

Drug Susceptibility Testing

The *in vitro* activities against bacterial strains were measured by the resazurin reduction microplate assay (REMA) by performing 2× serial dilutions of compounds in the working bacterial culture in 96-well plates (100 µL final volume). Bacterial viability was determined by adding sterile resazurin (10 µL, 0.025% w/v), incubating, and measuring resazurin turnover by fluorescence (excitation 560 nm/emission 590 nm) using a TECAN Infinite M200 microplate reader. For *M. marinum*, the strains carried an integrative plasmid containing the Lux operon encoding luciferase,³⁰ and cell viability was evaluated by measuring luminescence after 3 days of exposure to the drug.

Fluorescent Labeling of Purified DprE1

Purified *M. tuberculosis* DprE1 (5 µM) was incubated at 30 °C for 2 h with different fluorescent compounds (10 µM), farnesyl-phosphoryl-β-D-ribofuranose (FPR; 200 µM), and FAD (5 µM) in enzyme assay buffer (50 mM glycylglycine pH 8.0, 200 mM potassium glutamate, 0.002% Brij-35) in a final volume of 20 µL. Reactions were stopped by addition of SDS-PAGE buffer without reducing agent and heating 5 min at 95 °C before loading on an SDS-PAGE gel. After electrophoresis, gels were scanned using a GE Typhoon Trio scanner, and fluorescence was measured in the fluorescein channel for **JN23** and **JN94** (excitation 488 nm/emission 520 nm) or TAMRA channel for **JN29**, **JN62**, **JN96**, **JN108**, **JN105**, and **JN111** (excitation 523 nm/emission

580 nm). Finally, gels were stained with Coomassie blue. To denature DprE1, the purified enzyme was heated at 95 °C for 10 min before adding **JN108** to the reaction.

Labeling of Cell-Free Extracts of *M. tuberculosis* or Hepatocytes

Cell-free extracts of *M. tuberculosis* and HepG2 cells were prepared by bead-beating as described above. Proteins (68 µg) from cell-free extracts were added to the reaction mixture containing FPR (200 µM), FAD (5 µM), glycylglycine (50 mM pH 8.0), potassium glutamate (200 mM), and Brij-35 (0.002%) in a final volume of 20 µL. Reactions were stopped, and proteins were processed for fluorescence scanning as outlined above. In some cases, purified recombinant *M. tuberculosis* DprE1 was added to the protein extracts as a positive control for labeling.

Time-Lapse Imaging

Time-lapse microscopy of bacteria was carried out as described before.^{21,31} Briefly, bacteria from exponentially growing cultures of *M. smegmatis* or *M. tuberculosis* were implanted in a custom-fabricated microfluidic device,³¹ and imaging was carried out using a 100× objective (Olympus UPLFL 100× PH, 1.3 NA) on a personal DV microscope system (GE Healthcare Life Sciences). Images were acquired every 15 min (*M. smegmatis*) or every 60 min (*M. tuberculosis*) on the FITC (excitation 490/20, emission 528/38), RD-TR-PE (excitation 542/27, emission 585/29), and phase channels. Complete 7H9 medium with or without the fluorophores (**JN108** or **JN105**, 400 ng/mL for *M. tuberculosis*, 700 ng/mL for *M. smegmatis*) was pumped through the device at a flow rate of 15–20 µL/min. The images were subsequently processed and analyzed using Deltavision SoftWorx 4.1 (GE Healthcare Life Sciences) and ImageJ v 1.47a (<http://rsb.info.nih.gov/ij/>).

Subcellular Localization of DprE1

To visualize **JN108** labeling at the subcellular level, the bacteria were incubated with 8 µM **JN108** in complete 7H9 medium, washed twice with PBS containing 0.05% Tween-80, resuspended, adsorbed on an agarose pad, and covered by a glass coverslip. The specimen was then observed with an Olympus IX81 inverted microscope or an LSM 700 inverted confocal microscope (Zeiss). For super-resolution imaging (structured illumination microscopy), 1 µL of bacterial suspension was spotted between two coverslips and imaged with a Nikon Eclipse Ti inverted setup, and images were reconstructed with NIS-Elements software.

AUTHOR PRESENT ADDRESS

J.N.: UCB Biopharma, Braine l'Alleud 1420, Belgium.

S.T.C.: Institut Pasteur, 25–28 rue du Docteur Roux, 75015 Paris, France.

AUTHOR CONTRIBUTIONS

J.N., R.S., N.D., and S.T.C. wrote the paper. R.S. and J.N. contributed equally to this work.

The authors declare no competing financial interest.

ACKNOWLEDGEMENTS

We thank A. Vocat and S. Boy-Röttger for technical assistance, L. Vera-Cabrera for providing strains, C. Trefzer and K. Johnsson for useful discussions and L. Reymond for the synthesis of compounds. The research leading to these results received funding from the European Community's Seventh Framework Programme (MM4TB, Grant 260872) and from an International Incoming Marie Curie fellowship from the European Commission to J.N. (DPRETB, Grant 252802). R.S. was supported by a grant from the Fondation Jacqueline Beytout. V.M. and S.T.C. are named inventors on patents related to this work.

REFERENCES

1. Migliori, G. B., Loddenkemper, R., Blasi, F., and Raviglione, M. C. (2007) 125 years after Robert Koch's discovery of the tubercle bacillus: the new XDR-TB threat. Is "science" enough to tackle the epidemic?. *Eur. Respir. J.* 29, 423– 427, DOI: 10.1183/09031936.00001307
2. WHO. (2016) Global Tuberculosis Report 2015. World Health Organization, Geneva.
3. Green, K. D. and Garneau-Tsodikova, S. (2013) Resistance in tuberculosis: what do we know and where can we go?. *Front. Microbiol.* 4, 208, DOI: 10.3389/fmicb.2013.00208
4. Koul, A., Arnoult, E., Lounis, N., Guillemont, J., and Andries, K. (2011) The challenge of new drug discovery for tuberculosis. *Nature* 469, 483– 490, DOI: 10.1038/nature09657
5. Zumla, A., Nahid, P., and Cole, S. T. (2013) Advances in the development of new tuberculosis drugs and treatment regimens. *Nat. Rev. Drug Discovery* 12, 388– 404, DOI: 10.1038/nrd4001
6. Zumla, A. I., Gillespie, S. H., Hoelscher, M., Philips, P. P. J., Cole, S. T., Abubakar, I., McHugh, T. D., Schito, M., Maeurer, M., and Nunn, A. J. (2014) New antituberculosis drugs, regimens, and adjunct therapies: needs, advances, and future prospects. *Lancet Infect. Dis.* 14, 327– 340, DOI: 10.1016/S1473-3099(13)70328-1
7. Makarov, V., Lechartier, B., Zhang, M., Neres, J., van der Sar, A. M., Raadsen, S. A., Hartkoorn, R. C., Ryabova, O. B., Vocat, A., Decosterd, L. A., Widmer, N., Buclin, T., Bitter, W., Andries, K., Pojer, F., Dyson, P. J., and Cole, S. T. (2014) Towards a new combination therapy for tuberculosis with next generation benzothiazinones. *EMBO Mol. Med.* 6, 372– 383, DOI: 10.1002/emmm.201303575
8. Makarov, V., Manina, G., Mikusova, K., Möllmann, U., Ryabova, O., Saint-Joanis, B., Dhar, N., Pasca, M. R., Buroni, S., Lucarelli, A. P., Milano, A., De Rossi, E., Belanova, M., Bobovska, A., Dianiskova, P., Kordulakova, J., Sala, C., Fullam, E., Schneider, P., McKinney, J. D., Brodin, P., Christophe, T., Waddell, S., Butcher, P., Albrethsen, J., Rosenkrands, I., Brosch, R., Nandi, V., Bharath, S., Gaonkar, S., Shandil, R. K., Balasubramanian, V., Balganes, T., Tyagi, S., Grosset, J., Riccardi, G., and Cole, S. T. (2009) Benzothiazinones kill Mycobacterium tuberculosis by blocking arabinan synthesis. *Science* 324, 801– 804, DOI: 10.1126/science.1171583

9. Mikusová, K., Makarov, V., and Neres, J. (2013) DprE1--from the discovery to the promising tuberculosis drug target. *Curr. Pharm. Des.* 20, 4379– 4403, DOI: 10.2174/138161282027140630122724
10. Mikusová, K., Huang, H., Yagi, T., Holsters, M., Vereecke, D., D’Haeze, W., Scherman, M. S., Brennan, P. J., McNeil, M. R., and Crick, D. C. (2005) Decaprenylphosphoryl arabinofuranose, the donor of the D-arabinofuranosyl residues of mycobacterial arabinan, is formed via a two-step epimerization of decaprenylphosphoryl ribose. *J. Bacteriol.* 187, 8020–8025, DOI: 10.1128/JB.187.23.8020-8025.2005
11. Neres, J., Pojer, F., Molteni, E., Chiarelli, L. R., Dhar, N., Boy-Röttger, S., Buroni, S., Fullam, E., Degiacomi, G., Lucarelli, A. P., Read, R. J., Zanoni, G., Edmondson, D. E., De Rossi, E., Pasca, M. R., McKinney, J. D., Dyson, P. J., Riccardi, G., Mattevi, A., Cole, S. T., and Binda, C. (2012) Structural basis for benzothiazinone-mediated killing of *Mycobacterium tuberculosis*. *Sci. Transl. Med.* 4, 150ra121, DOI: 10.1126/scitranslmed.3004395
12. Trefzer, C., Škovierová, H., Buroni, S., Bobovská, A., Nenci, S., Molteni, E., Pojer, F., Pasca, M. R., Makarov, V., Cole, S. T., Riccardi, G., Mikušová, K., and Johnsson, K. (2012) Benzothiazinones are suicide inhibitors of mycobacterial decaprenylphosphoryl- β -D-ribofuranose 2'-oxidase DprE1. *J. Am. Chem. Soc.* 134, 912– 915, DOI: 10.1021/ja211042r
13. Makarov, V., Neres, J., Hartkoorn, R. C., Ryabova, O. B., Kazakova, E., Šarkan, M., Huszár, S., Piton, J., Kolly, G. S., Vocat, A., Conroy, T. M., Mikušová, K., and Cole, S. T. (2015) The 8-Pyrrole-Benzothiazinones Are Noncovalent Inhibitors of DprE1 from *Mycobacterium tuberculosis*. *Antimicrob. Agents Chemother.* 59, 4446– 4452, DOI: 10.1128/AAC.00778-15
14. Karoli, T., Becker, B., Zuegg, J., Möllmann, U., Ramu, S., Huang, J. X., and Cooper, M. A. (2012) Identification of antitubercular benzothiazinone compounds by ligand-based design. *J. Med. Chem.* 55, 7940– 7944, DOI: 10.1021/jm3008882
15. Tiwari, R., Möllmann, U., Cho, S., Franzblau, S. G., Miller, P. A., and Miller, M. J. (2014) Design and Syntheses of Anti-Tuberculosis Agents Inspired by BTZ043 Using a Scaffold Simplification Strategy. *ACS Med. Chem. Lett.* 5, 587– 591, DOI: 10.1021/ml500039g
16. Makarov, V. A. (2011) Process for the preparation of 2-amino-substituted 1,3-benzothiazine-4-ones; patent WO2011132070A1.
17. Neres, J., Hartkoorn, R. C., Chiarelli, L. R., Gadupudi, R., Pasca, M. R., Mori, G., Venturelli, A., Savina, S., Makarov, V., Kolly, G. S., Molteni, E., Binda, C., Dhar, N., Ferrari, S., Brodin,

- P., Delorme, V., Landry, V., de Jesus Lopes Ribeiro, A. L., Farina, D., Saxena, P., Pojer, F., Carta, A., Luciani, R., Porta, A., Zanoni, G., De Rossi, E., Costi, M. P., Riccardi, G., and Cole, S. T. (2015) 2-Carboxyquinoxalines kill mycobacterium tuberculosis through noncovalent inhibition of DprE1. *ACS Chem. Biol.* *10*, 705–714, DOI: 10.1021/cb5007163
18. Trefzer, C., Rengifo-Gonzalez, M., Hinner, M. J., Schneider, P., Makarov, V., Cole, S. T., and Johnsson, K. (2010) Benzothiazinones: prodrugs that covalently modify the decaprenylphosphoryl- β -D-ribose 2'-epimerase DprE1 of *Mycobacterium tuberculosis*. *J. Am. Chem. Soc.* *132*, 13663–13665, DOI: 10.1021/ja106357w
19. Brecik, M., Centárová, I., Mukherjee, R., Kolly, G. S., Huszár, S., Bobovská, A., Kilacsková, E., Mokošová, V., Svetlíková, Z., Šarkan, M., Neres, J., Korduláková, J., Cole, S. T., and Mikušová, K. (2015) DprE1 Is a Vulnerable Tuberculosis Drug Target Due to Its Cell Wall Localization. *ACS Chem. Biol.* *10*, 1631–1636, DOI: 10.1021/acscchembio.5b00237
20. Foo, C. S.-Y., Lechartier, B., Kolly, G. S., Boy-Röttger, S., Neres, J., Rybniker, J., Lupien, A., Sala, C., Piton, J., and Cole, S. T. (2016) Characterization of DprE1-Mediated Benzothiazinone Resistance in *Mycobacterium tuberculosis*. *Antimicrob. Agents Chemother.* *60*, 6451–6459, DOI: 10.1128/AAC.01523-16
21. Wakamoto, Y., Dhar, N., Chait, R., Schneider, K., Signorino-Gelo, F., Leibler, S., and McKinney, J. D. (2013) Dynamic persistence of antibiotic-stressed mycobacteria. *Science* *339*, 91–95, DOI: 10.1126/science.1229858
22. Santi, I., Dhar, N., Bousbaine, D., Wakamoto, Y., and McKinney, J. D. (2013) Single-cell dynamics of the chromosome replication and cell division cycles in mycobacteria. *Nat. Commun.* *4*, 2470, DOI: 10.1038/ncomms3470
23. Kolly, G. S., Mukherjee, R., Kilacsková, E., Abriata, L. A., Raccaud, M., Blaško, J., Sala, C., Dal Peraro, M., Mikušová, K., and Cole, S. T. (2015) GtrA Protein Rv3789 Is Required for Arabinosylation of Arabinogalactan in *Mycobacterium tuberculosis*. *J. Bacteriol.* *197*, 3686–3697, DOI: 10.1128/JB.00628-15
24. González-Martínez, N. A., Lozano-Garza, H. G., Castro-Garza, J., De Osio-Cortez, A., Vargas-Villarreal, J., Cavazos-Rocha, N., Ocampo-Candiani, J., Makarov, V., Cole, S. T., and Vera-Cabrera, L. (2015) In Vivo Activity of the Benzothiazinones PBTZ169 and BTZ043 against *Nocardia brasiliensis*. *PLoS Neglected Trop. Dis.* *9*, e0004022, DOI: 10.1371/journal.pntd.0004022

25. Sala, C., Dhar, N., Hartkoorn, R. C., Zhang, M., Ha, Y. H., Schneider, P., and Cole, S. T. (2010) Simple Model for Testing Drugs against Nonreplicating Mycobacterium tuberculosis. *Antimicrob. Agents Chemother.* *54*, 4150–4158, DOI: 10.1128/AAC.00821-10
26. Zhang, M., Sala, C., Hartkoorn, R. C., Dhar, N., Mendoza-Losana, A., and Cole, S. T. (2012) Streptomycin-Starved Mycobacterium tuberculosis 18b, a Drug Discovery Tool for Latent Tuberculosis. *Antimicrob. Agents Chemother.* *56*, 5782–5789, DOI: 10.1128/AAC.01125-12
27. Hostettler, L., Grundy, L., Käser-Pébernard, S., Wicky, C., Schafer, W. R., and Glauser, D. A. (2017) The Bright Fluorescent Protein mNeonGreen Facilitates Protein Expression Analysis In Vivo. *G3: Genes, Genomes, Genet.* *7*, 607–615, DOI: 10.1534/g3.116.038133
28. Shaner, N. C., Lambert, G. G., Chammas, A., Ni, Y., Cranfill, P. J., Baird, M. A., Sell, B. R., Allen, J. R., Day, R. N., Israelsson, M., Davidson, M. W., and Wang, J. (2013) A bright monomeric green fluorescent protein derived from Branchiostoma lanceolatum. *Nat. Methods* *10*, 407–409, DOI: 10.1038/nmeth.2413
29. Chen, J. M., Boy-Röttger, S., Dhar, N., Sweeney, N., Buxton, R. S., Pojer, F., Rosenkrands, I., and Cole, S. T. (2012) EspD Is Critical for the Virulence-Mediating ESX-1 Secretion System in Mycobacterium tuberculosis. *J. Bacteriol.* *194*, 884–893, DOI: 10.1128/JB.06417-11
30. Sharma, S., Gelman, E., Narayan, C., Bhattacharjee, D., Achar, V., Humnabadkar, V., Balasubramanian, V., Ramachandran, V., Dhar, N., and Dinesh, N. (2014) Simple and Rapid Method To Determine Antimycobacterial Potency of Compounds by Using Autoluminescent Mycobacterium tuberculosis. *Antimicrob. Agents Chemother.* *58*, 5801–5808, DOI: 10.1128/AAC.03205-14
31. Dhar, N. and Manina, G. (2015) Single-cell analysis of mycobacteria using microfluidics and time-lapse microscopy. *Methods Mol. Biol.* *1285*, 241–256, DOI: 10.1007/978-1-4939-2450-9_14

SUPPORTING INFORMATION

Synthesis of compounds from Scheme 1:

***tert*-Butyl (2-(2-(2-(piperazin-1-yl)ethoxy)ethoxy)ethyl)carbamate (2).** To a solution of piperazine (0.41 g, 4.80 mmol) in DMF (20 mL) was added *tert*-butyl (2-(2-(2-bromoethoxy)ethoxy)ethyl)carbamate **1** (0.5 g, 1.60 mmol, synthesized according to a literature procedure¹), and the reaction mixture was stirred at 60 °C for 4 h. The solvent was removed under vacuum, the residue resuspended in EtOAc (30 mL) and extracted with 1 N NaOH (20 mL). The aqueous layer was back-extracted with 2 x 20 mL EtOAc. The combined organic layers were washed with brine, dried with anhydrous MgSO₄ and the solvent removed under vacuum. The residue was purified by column chromatography with a DCM/[MeOH/Ammonia 9:1] gradient, affording the title product (0.50 g, 99%) as a pale yellow oil: *R*_f 0.73 (EtOAc); ¹H NMR (400 MHz, CDCl₃) δ 1.43 (s, 9H), 1.83 (br s, 1H), 2.46 (br s, 4H), 2.58 (t, *J*=6.0 Hz, 2H), 2.88 (t, *J*=4.9 Hz, 4H), 3.28-3.31 (m, 2H), 3.52(t, *J*=5.0 Hz, 2H), 3.58-3.62 (m, 6H). ¹³C NMR (100 MHz, CDCl₃) δ 28.5, 40.5, 55.1, 58.5, 68.9, 70.35 (2C), 7.40, 79.2, 156.1. MS (ESI+) calcd for C₁₁H₂₂BrNO₄ [M + H]⁺, 318.2; found 318.3.

8-Azidoctan-1-ol (4). 8-Chlorooctan-1-ol **3** (2 g, 12.1 mmol) and sodium azide (1.18 g, 18.2 mmol) were suspended in DMF (40 mL) and stirred at 100 °C for 4h. The reaction mixture was cooled to room temperature and the solid in suspension removed by filtration. The solvent was removed under vacuum. The residue was resuspended in dichloromethane, filtered through celite and the solvent removed under vacuum, affording the title compound (2.1 g, 100%) as a clear oil: *R*_f 0.26 (EtOAc); ¹H NMR (400 MHz, CDCl₃) δ 1.27-1.40 (m, 8H), 1.50-1.61 (m, 4H), 1.79 (s, 1H), 3.23 (t, *J*=7.0 Hz, 2 H), 3.60 (t, *J*=6.6 Hz, 2 H). ¹³C NMR (100 MHz, CDCl₃) δ 25.7, 26.7, 28.9, 29.2, 29.3, 32.7, 51.5, 62.9.

***tert*-Butyl (8-hydroxyoctyl)carbamate (5).** To a solution of 8-azidoctan-1-ol **4** (2.1 g, 12.1 mmol) in THF (40 mL) was added triphenylphosphine (3.49 g, 13.3 mmol) followed by stirring for 3 h at room temperature. Water (40 mL) was added to the reaction mixture and stirring continued for 20 h. The resulting solution was concentrated under vacuum to remove most of the THF, affording a suspension of 2-(2-(2-aminoethoxy)ethoxy)ethanol in water, which was diluted with acetonitrile (40 mL). To the resulting solution was added Boc₂O (2.63 g, 12.1 mmol) and NaOH (10 mL 1 N solution). The reaction mixture was stirred for 3 h at room temperature and the solvent was removed under vacuum. Purification by column chromatography with an *n*-hexane/EtOAc gradient afforded the title product (2.64 g, 89%) as a white solid: *R*_f 0.48 (*n*-hexane/EtOAc 7:1); ¹H NMR (400 MHz, CDCl₃) δ 1.27-1.36 (m, 8H), 1.43 (s, 9H), 1.42-1.48 (m, 2H), 1.50-1.58 (m, 2H),

3.09 (t, $J=7.1$ Hz, 2 H), 3.62 (t, $J=6.6$ Hz, 2 H). ^{13}C NMR (100 MHz, CDCl_3) δ 25.8, 26.8, 28.6, 29.3, 29.4, 30.1, 32.8, 40.9, 63.1, 79.3, 156.2.

***tert*-Butyl (8-bromooctyl)carbamate (6).** To a solution of *tert*-butyl (8-hydroxyoctyl)carbamate **5** (2.59 g, 10.6 mmol) and carbon tetrabromide (4.39 g, 13.2 mmol) in dichloromethane (30 mL) was added potassium carbonate (2.2 g, 15.9 mmol). A solution of triphenylphosphine (4.2 g, 16.0 mmol) in dichloromethane (25 mL) was then slowly added over 15 min. with stirring at room temperature. Stirring continued for 4 h. The white solid in suspension was removed by filtration, the filtrate concentrated under vacuum and the residue purified by column chromatography (*n*-hexane/EtOAc gradient), affording the title compound (1.98 g, 61%) as a clear oil: R_f 0.76 (*n*-hexane/EtOAc 7:3); ^1H NMR (400 MHz, CDCl_3) δ 1.25-1.35 (m, 6H), 1.35-1.49 (m, 13H), 1.78-1.85 (m, 2H), 3.07 (t, $J=7.1$ Hz, 2 H), 3.37 (t, $J=6.8$ Hz, 2 H). ^{13}C NMR (100 MHz, CDCl_3) δ 26.7, 28.1, 28.5, 28.7, 29.1, 30.1, 32.8, 34.0, 40.8, 79.1, 156.1.

***tert*-Butyl (8-aminooctyl)carbamate (7).** To a solution of *tert*-butyl (8-bromooctyl)carbamate **6** (90 mg, 0.29 mmol) in dimethoxyethane (10 mL) was added ammonia (1 mL, 35% solution in water) in a sealed vessel. The reaction mixture was heated to 75 °C for 6 h. The solvent was evaporated and the residue was purified by column chromatography (EtOAc/MeOH gradient), affording the title product (68 mg, 96%) as a pale yellow oil: R_f 0.23 (DCM/MeOH/Ammonia 9:0.9:0.1); ^1H NMR (400 MHz, CD_3OD) δ 1.30-1.51 (m, 19H), 1.63-1.71 (m, 2H), 2.92 (t, $J=7.6$ Hz, 2H), 3.01 (t, $J=7.0$ Hz, 2H). ^{13}C NMR (100 MHz, CD_3OD) δ 27.3, 27.7, 28.5, 28.8, 30.1 (2 carbons), 30.9, 40.8, 41.3, 79.8, 158.5. MS (ESI+) calcd for $\text{C}_{13}\text{H}_{29}\text{N}_2\text{O}_2$ [$\text{M} + \text{H}$] $^+$, 245.2; found 245.1.

***tert*-Butyl (8-(piperazin-1-yl)octyl)carbamate (8).** To a solution of piperazine (1.95 g, 22.7 mmol) in DMF (20 mL) was added *tert*-butyl (8-bromooctyl)carbamate **6**, and the reaction mixture was stirred at 60 °C for 4 h. The solvent was removed under vacuum, the residue re-suspended in EtOAc (30 mL) and extracted with 1 N NaOH (20 mL). The aqueous layer was back-extracted with 2 x 20 mL EtOAc. The combined organic layers were washed with brine, dried with anhydrous MgSO_4 and the solvent removed under vacuum. The residue was purified by column chromatography with a DCM/[MeOH/Ammonia 9:1] gradient, affording the title product (1.28 g, 90%) as a pale yellow oil: R_f 0.27 (DCM/MeOH/Ammonia 9:0.9:0.1); ^1H NMR (400 MHz, CD_3OD) δ 1.27-1.38 (m, 8H), 1.38-1.56 (m, 13H), 2.33-2.37 (m, 2H), 2.48 (br s, 4H), 2.88 (t, $J=4.8$ Hz, 4H), 3.01 (t, $J=6.9$ Hz, 2H), 4.92 (s, 1H). ^{13}C NMR (100 MHz, CDCl_3) δ 26.6, 26.8, 27.5, 28.5, 29.3, 29.5, 30.1, 40.6, 45.8, 54.2, 59.4, 79.0, 156.0. MS (ESI+) calcd for $\text{C}_{17}\text{H}_{36}\text{N}_3\text{O}_2$ [$\text{M} + \text{H}$] $^+$, 314.3; found 314.4.

Synthesis of compounds from Scheme 2:

General procedure 1: linker coupling with 2-(methylthio)-8-nitro-6-(trifluoromethyl)-4H-benzo[e][1,3]thiazin-4-one (10).

To a solution of 2-(methylthio)-8-nitro-6-(trifluoromethyl)-4H-benzo[e][1,3] thiazin-4-one **10**² (1.0 equiv.) in 5 mL EtOH was added the appropriate linker prepared above (1.03 equiv.). The reaction mixture was heated to 50°C with stirring and under N₂ for 18 h. The solvent was removed under vacuum and the residue purified by flash chromatography, to afford the desired product.

General procedure 2: Boc hydrolysis from coupled benzothiazinone-linker compounds, and amine coupling with fluorophores.

The benzothiazinone derivative obtained from coupling of **10** with the appropriate Boc-protected linker (1.2 equiv.) was dissolved in DCM/TFA (1:1, 2 mL) and the resulting solution was stirred at room temperature for 2 h. The reaction mixture was concentrated under vacuum and the residue dried under high-vacuum, affording the free amine product as a thick oil, which was used without further purification for the next step.

To a solution of the product obtained above in 2 mL anhydrous DMF was added diisopropylethylamine (6 equiv.) and the solution was stirred under N₂ for 15 min. The NHS ester of the desired fluorophore (1.0 equiv.) was added to the solution and stirring continued under N₂ at room temperature for 7 h. The solvent was removed under vacuum and the residue dried overnight under high-vacuum. Purification by column chromatography (DCM/[MeOH/Ammonia 9:1] gradient) afforded the title product as a solid.

3',6'-dihydroxy-N-(2-(2-(2-((8-nitro-4-oxo-6-(trifluoromethyl)-4H-benzo[e][1,3]thiazin-2-yl)amino)ethoxy)ethoxy)ethyl)-3-oxo-3H-spiro[isobenzofuran-1,9'-xanthene]-5-carboxamide (JN23). Prepared using general procedure 2, with compound **9** (22.5 mg, 0.042 mmol, previously described³) and the NHS ester of 5-carboxyfluorescein (16.6 mg, 0.035 mmol). The residue obtained after evaporation of the solvent from the reaction mixture was purified by preparative HPLC, affording the title product (4 mg, 15%) as an orange solid: *R_f* 0.25 (EtOAc/MeOH 9:1); ¹H NMR (400 MHz, CD₃OD) δ 3.62 (t, *J*=5.4 Hz, 2H), 3.69-3.77 (m, 10H), 6.55 (dd, *J*=2.1, 8.7 Hz, 2H), 6.61 (d, *J*=8.7 Hz, 2H), 6.68 (d, *J*=2.1 Hz, 2H), 7.33 (d, *J*=8.0 Hz, 1H), 8.19 (dd, *J*=1.6, 8.0 Hz, 1H), 8.42 (s, 1H), 8.82 (d, *J*=1.6 Hz, 1H), 8.88 (d, *J*=1.6 Hz, 1H). HRMS (ESI+) calcd for C₃₆H₂₈F₃N₄O₁₁S [M + H]⁺, 781.1422; found 781.1428 (error: 0.8 ppm).

tert-butyl (8-((8-nitro-4-oxo-6-(trifluoromethyl)-4H-benzo[e][1,3]thiazin-2-yl)amino)octyl)carbamate (11). Prepared using general procedure 1, with *tert*-butyl (8-

aminoethyl)carbamate **7** (90 mg, 0.28 mmol). Purification by flash chromatography (*n*-hexane/EtOAc gradient), afforded the title compound (77 mg, 53%) as a solid: R_f 0.5 (*n*-hexane/EtOAc, 1:1); ^1H NMR (400 MHz, CDCl_3) δ 1.23-1.50 (m, 19H), 1.64-1.70 (m, 2 H), 3.04-3.10 (m, 2H), 3.61-3.71 (m, 2H), 4.65 (br s, 1H), 7.70 (br s, 1H), 8.73 (s, 1H), 9.07 (s, 1H). ^{13}C NMR (100 MHz, CDCl_3) δ 26.6, 26.8 (2C), 28.5, 28.8, 29.1, 30.0, 40.7, 43.4, 79.4, 122.6, 126.1, 127.2, 129.3, 133.6, 135.7, 143.4, 156.3, 163.3, 167.3.

3',6'-bis(dimethylamino)-*N*-(8-((8-nitro-4-oxo-6-(trifluoromethyl)-4*H*-benzo[*e*][1,3]thiazin-2-yl)amino)octyl)-3-oxo-3*H*-spiro[isobenzofuran-1,9'-xanthene]-5-carboxamide (JN96).

Prepared using general procedure 2, from compound **11** (5.7 mg, 0.011 mmol) and the NHS ester of 5-carboxytetramethylrhodamine (5 mg, 0.0095 mmol), affording the title product (4.1 mg, 52%) as dark purple solid: R_f 0.61 (DCM/[MeOH/Ammonia 9:1] 9:1); ^1H NMR (400 MHz, CD_3OD) δ 1.30-1.50 (m, 8H), 1.60-1.72 (m, 2H), 3.27 (s, 12H), 3.45 (t, $J=6.5$ Hz, 2H), 3.57 (t, $J=6.8$ Hz, 2H), 6.87 (d, $J=2.5$ Hz, 2H), 7.01 (dd, $J=2.5, 9.5$ Hz, 2H), 7.25 (d, $J=9.5$ Hz, 2H), 7.37 (d, $J=7.9$ Hz, 1H), 8.04 (dd, $J=1.8, 7.9$ Hz, 1H), 8.49 (d, $J=1.8$ Hz, 1H), 8.84 (s, 1H), 8.91 (s, 1H). HRMS (ESI+) calcd for $\text{C}_{42}\text{H}_{42}\text{F}_3\text{N}_6\text{O}_7\text{S}$ [$\text{M} + \text{H}$] $^+$, 831.2782; found 831.2787 (error: 0.6 ppm).

***tert*-butyl (2-(2-(2-(4-(8-nitro-4-oxo-6-(trifluoromethyl)-4*H*-benzo[*e*][1,3]thiazin-2-yl)piperazin-1-yl)ethoxy)ethoxy)ethyl)carbamate (12).**

Prepared using general procedure 1, with *tert*-butyl (8-aminoethyl)carbamate **2** (82 mg, 0.26 mmol). Purification by flash chromatography (EtOAc/MeOH gradient), afforded the title compound (136 mg, 92%) as a solid: R_f 0.25 (EtOAc/MeOH, 9:1); ^1H NMR (400 MHz, CDCl_3) δ 1.37 (s, 9H), 2.60-2.65 (m, 6 H), 3.23-3.26 (m, 2H), 3.48 (t, $J=5.1$ Hz, 2H), 3.56 (s, 4H), 3.59 (t, $J=5.5$ Hz, 2H), 4.00 (br s, 4H), 8.68 (d, $J=2.0$ Hz, 1H), 9.00 (d, $J=2.0$ Hz, 1H). ^{13}C NMR (100 MHz, CDCl_3) δ 28.4, 40.3, 46.4, 52.9, 57.3, 68.7, 70.18, 70.22, 70.3, 79.2, 122.4, 126.0, 126.7, 129.5, 133.3, 134.1, 143.9, 155.9, 162.0, 166.4. MS (ESI+) calcd for $\text{C}_{24}\text{H}_{33}\text{F}_3\text{N}_5\text{O}_7\text{S}$ [$\text{M} + \text{H}$] $^+$, 592.2; found 592.0.

3',6'-bis(dimethylamino)-*N*-(2-(2-(2-(4-(8-nitro-4-oxo-6-(trifluoromethyl)-4*H*-benzo[*e*][1,3]thiazin-2-yl)piperazin-1-yl)ethoxy)ethoxy)ethyl)-3-oxo-3*H*-spiro[isobenzofuran-1,9'-xanthene]-5-carboxamide (JN62).

Prepared using general procedure 2, with compound **12** (12.4 mg, 0.021 mmol) and the NHS ester of 5-carboxytetramethylrhodamine (9 mg, 0.017 mmol), affording the title product (9 mg, 58%) as a dark purple solid: R_f 0.35 (DCM/[MeOH/Ammonia 9:1] 9:1); ^1H NMR (400 MHz, CD_3OD) δ 2.55-2.67 (m, 6H), 3.27 (s, 12H), 3.65-3.77 (m, 10H), 4.00 (br s, 4H), 6.67 (d, $J=2.4$ Hz, 2H), 6.99 (dd, $J=2.5, 9.4$ Hz, 2H), 7.23 (d, $J=9.4$ Hz, 2H), 7.56 (d, $J=7.9$ Hz, 1H), 8.15 (dd, $J=1.8, 7.9$ Hz, 1H), 8.57 (d, $J=1.8$ Hz, 1H), 8.84 (d, $J=2.0$ Hz, 1H), 8.90 (d, $J=2.0$ Hz, 1H). HRMS (ESI+) calcd for $\text{C}_{44}\text{H}_{45}\text{F}_3\text{N}_7\text{O}_9\text{S}$ [$\text{M} + \text{H}$] $^+$, 904.2941; found 904.2952 (error: 1.2 ppm).

5,5-difluoro-7,9-dimethyl-3-(3-((2-(2-(2-(4-(8-nitro-4-oxo-6-(trifluoromethyl)-4H-benzo[e][1,3]thiazin-2-yl)piperazin-1-yl)ethoxy)ethoxy)ethyl)amino)-3-oxopropyl)-5H-dipyrrolo[1,2-c:2',1'-f][1,3,2]diazaborinin-4-ium-5-uide (JN94). Prepared using general procedure 2, from compound **12** (5.6 mg, 0.0094 mmol) and the NHS ester of BODIPY-FL (3 mg, 0.0078 mmol), affording the title product (2.2 mg, 37%) as a light orange solid: R_f 0.48 (EtOAc); ^1H NMR (400 MHz, CD_3OD) δ 2.17 (s, 3H), 2.41 (s, 3H), 2.60-2.73 (m, 8H), 3.19 (t, $J=7.9$ Hz, 2H), 3.40 (t, $J=5.4$ Hz, 2H), 3.57 (t, $J=5.4$ Hz, 2H), 3.63 (s, 4H), 3.66 (t, $J=5.2$ Hz, 2H), 4.00 (br s, 4H), 6.06 (s, 1H), 6.31 (d, $J=4.0$ Hz, 1H), 6.93 (d, $J=4.0$ Hz, 1H), 7.24 (s, 1H), 8.82 (d, $J=1.9$ Hz, 1H), 8.88 (d, $J=1.9$ Hz, 1H). HRMS (ESI+) calcd for $\text{C}_{33}\text{H}_{38}\text{BF}_5\text{N}_7\text{O}_6\text{S}$ $[\text{M} + \text{H}]^+$, 766.2607; found 766.2623 (error: 2.0 ppm).

tert-butyl (8-(4-(8-nitro-4-oxo-6-(trifluoromethyl)-4H-benzo[e][1,3]thiazin-2-yl)piperazin-1-yl)octyl)carbamate (13). Prepared using general procedure 1, with *tert*-Butyl (8-(piperazin-1-yl)octyl)carbamate **8** (0.4 g, 1.28 mmol). Purification by flash chromatography (*n*-hexane/EtOAc gradient), afforded the title compound (0.52 g, 89%) as a solid: R_f 0.77 (EtOAc/MeOH, 9:1); ^1H NMR (400 MHz, CDCl_3) δ 1.28-1.32 (m, 8H), 1.41-1.51 (m, 13 H), 2.36-2.40 (m, 2H), 2.57 (br s, 4H), 3.07-3.12 (m, 2H), 3.88 (br s, 2H), 4.15 (br s, 2H), 4.50 (s, 1H), 8.75 (d, $J=2.0$ Hz, 1H), 9.09 (d, $J=2.0$ Hz, 1H). ^{13}C NMR (100 MHz, CDCl_3) δ 26.6, 26.7, 27.3, 28.4, 29.2, 29.4, 30.0, 40.6, 46.3, 52.6, 58.2, 79.0, 122.4, 126.0, 126.7, 129.7, 133.4, 134.1, 143.9, 156.0, 166.4.

3',6'-bis(dimethylamino)-N-(8-(4-(8-nitro-4-oxo-6-(trifluoromethyl)-4H-benzo[e][1,3]thiazin-2-yl)piperazin-1-yl)octyl)-3-oxo-3H-spiro[isobenzofuran-1,9'-xanthene]-5-carboxamide (JN108). Prepared using general procedure 2, from compound **13** (28 mg, 0.047 mmol) and the NHS ester of 5-carboxytetramethylrhodamine (20 mg, 0.038 mmol), affording the title product (11 mg, 32%) as dark purple solid: R_f 0.24 (DCM/[MeOH/Ammonia 9:1] 9:1); ^1H NMR (400 MHz, CD_3OD) δ 1.25-1.49 (m, 8H), 1.50-1.61 (m, 2H), 1.65-1.74 (m, 2H), 2.48 (t, $J=7.4$ Hz, 2H), 2.60 (br s, 4H), 3.26 (s, 12H), 3.48 (t, $J=6.5$ Hz, 2H), 4.00 (br s, 4H), 6.79 (d, $J=2.2$ Hz, 2H), 6.99 (dd, $J=2.2, 9.4$ Hz, 2H), 7.23 (d, $J=9.4$ Hz, 2H), 7.45 (d, $J=7.9$ Hz, 1H), 8.08 (d, $J=7.9$ Hz, 1H), 8.51 (s, 1H), 8.88 (s, 1H), 8.89 (s, 1H). HRMS (ESI+) calcd for $\text{C}_{46}\text{H}_{49}\text{F}_3\text{N}_7\text{O}_7\text{S}$ $[\text{M} + \text{H}]^+$, 900.3355; found 900.3366 (error: 1.2 ppm).

tert-Butyl (8-(4-(8-amino-4-oxo-6-(trifluoromethyl)-4H-benzo[e][1,3]thiazin-2-yl)piperazin-1-yl)octyl)carbamate (14). To a suspension of compound **13** (60 mg, 0.102 mmol) and ammonium chloride (1 mg, 0.019 mmol) in 8 mL EtOH was slowly added a solution of sodium hydrosulfide (0.114 mg, 2.04 mmol) in water (4 mL), with stirring at room temperature. Stirring continued for 18 h. The solvent was removed under vacuum and the residue purified by flash chromatography (EtOAc/MeOH gradient), affording the title compound (21 mg, 37%) as a sticky solid: R_f 0.29 (EtOAc/MeOH, 8:1); $^1\text{H NMR}$ (400 MHz, CDCl_3) δ 1.24-1.37 (m, 8H), 1.37-1.55 (m, 13 H), 2.35-2.39 (m, 2H), 2.54 (br s, 4H), 3.06-3.13 (m, 2H), 3.85 (br s, 4H), 4.08 (br s, 2H), 4.51 (s, 1H), 7.11 (s, 1H), 8.19 (s, 1H).

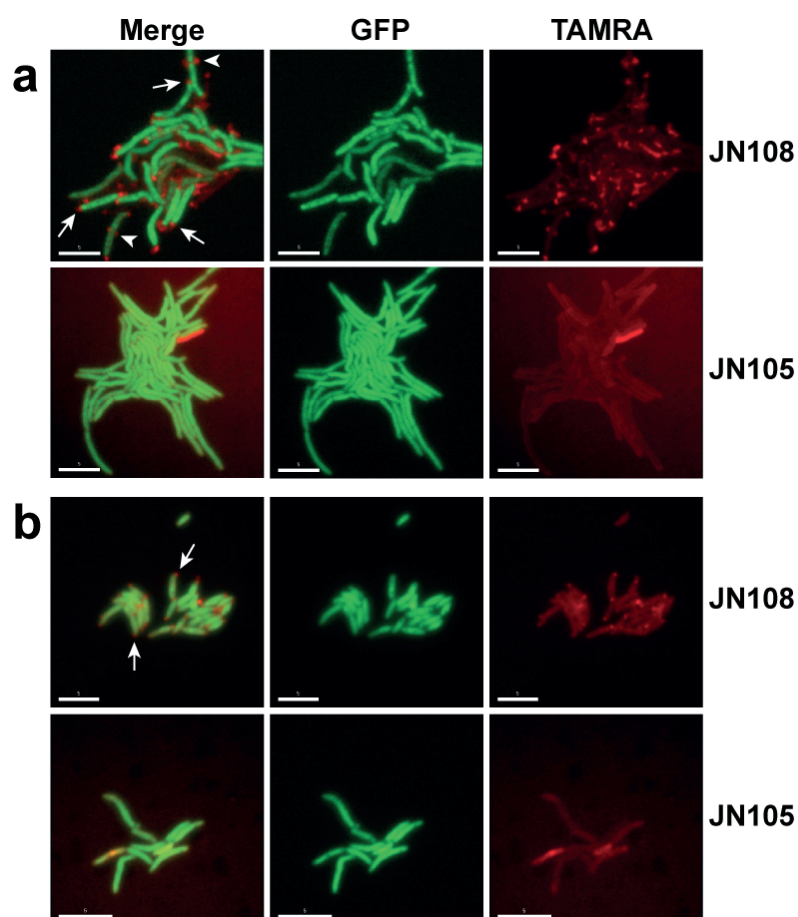
N-(8-(4-(8-amino-4-oxo-6-(trifluoromethyl)-4H-benzo[e][1,3]thiazin-2-yl)piperazin-1-yl)octyl)-3',6'-bis(dimethylamino)-3-oxo-3H-spiro[isobenzofuran-1,9'-xanthene]-5-carboxamide (JN105). Prepared using general procedure 2 from compound **14** (11 mg, 0.020 mmol) and the NHS ester of 5-carboxytetramethylrhodamine (9 mg, 0.017 mmol), affording the title product (7.5 mg, 43%) as a dark purple solid: R_f 0.64 (DCM/[MeOH/Ammonia 9:1] 5:1); $^1\text{H NMR}$ (400 MHz, CD_3OD) δ 1.36-1.58 (m, 10H), 1.69-1.76 (m, 2H), 2.37-2.42 (m, 2H), 2.51 (t, $J=4.7$ Hz, 4H), 3.26 (s, 12H), 3.52 (t, $J=6.5$ Hz, 2H), 3.90 (br s, 4H), 6.71 (d, $J=2.4$ Hz, 2H), 6.96 (dd, $J=2.4, 9.5$ Hz, 2H), 7.18 (d, $J=1.5$ Hz, 2H), 7.23 (d, $J=9.5$ Hz, 1H), 7.53 (d, $J=7.9$ Hz, 1H), 7.80 (d, $J=1.4$ Hz, 1H), 8.10 (dd, $J=1.8, 7.9$ Hz, 2H), 8.54 (d, $J=1.8$ Hz, 1H). HRMS (ESI+) calcd for $\text{C}_{46}\text{H}_{51}\text{F}_3\text{N}_7\text{O}_5\text{S}$ [$\text{M} + \text{H}$] $^+$, 870.3614; found 870.3624 (error: 1.1 ppm).

2-(6-(dimethylamino)-3-(dimethyliminio)-3H-xanthen-9-yl)-5-(propylcarbamoyl)benzoate (JN111). To a solution of the NHS ester of 5-carboxytetramethylrhodamine (4 mg, 0.076 mmol) in 0.5 mL anhydrous DMF was added propylamine (20 μL , 0.24 mmol), and the resulting solution was stirred for 3 h at room temperature. The solvent was evaporated and the residue purified by column chromatography (DCM/MeOH gradient) affording the title product (2.5 mg, 70%) as a dark purple solid: R_f 0.41 (DCM/MeOH 4:1); $^1\text{H NMR}$ (400 MHz, CD_3OD) δ 1.02 (t, $J=1.4$ Hz, 1H), 1.65-1.72 (m, 2H), 3.14 (s, 12H), 3.49 (br s, 2H), 6.68-6.68 (m, 4H), 6.94 (d, $J=7.9$ Hz, 1H), 7.23 (d, $J=7.3$ Hz, 1H), 8.20 (d, $J=7.3$ Hz, 1H), 8.53 (s, 1H). HRMS (ESI+) calcd for $\text{C}_{28}\text{H}_{30}\text{N}_3\text{O}_4$ [$\text{M} + \text{H}$] $^+$, 472.2231; found 472.2236 (error: 1.0 ppm).

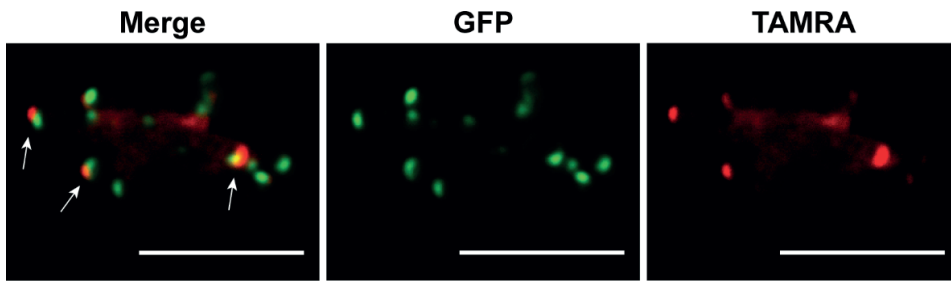
Staining of nascent peptidoglycan

Labeling of the sites of incorporation of new peptidoglycan in living bacteria was adapted from Siegrist *et al.*, 2013.⁴ Briefly, bacteria were grown in the presence of 5 mM of (R)- α -Propargylglycine, washed with PBS containing 0.05% Tween-80 and fixed in PFA. The click chemistry reaction was performed at room temperature for 1 h with 1 mM CuSO_4 , 1 mM Tris(3-hydroxypropyl)triazolylmethylamine, 20 μM of Rhodamine 110-azide and 1.2 mM sodium

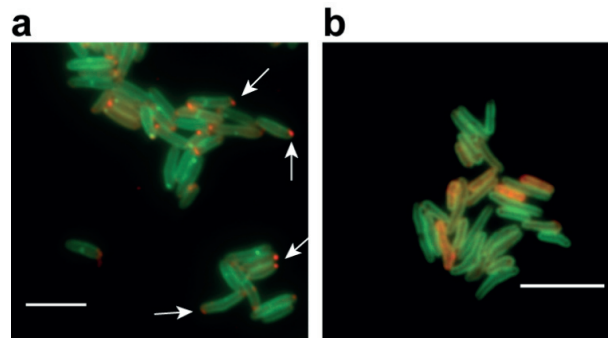
ascorbate in PBS. Finally, bacteria were washed, resuspended and mounted on an agarose pad. Micrographs were acquired with the FITC (excitation 490/20, emission 528/38) and phase or trans light channels and images processed with ImageJ software.



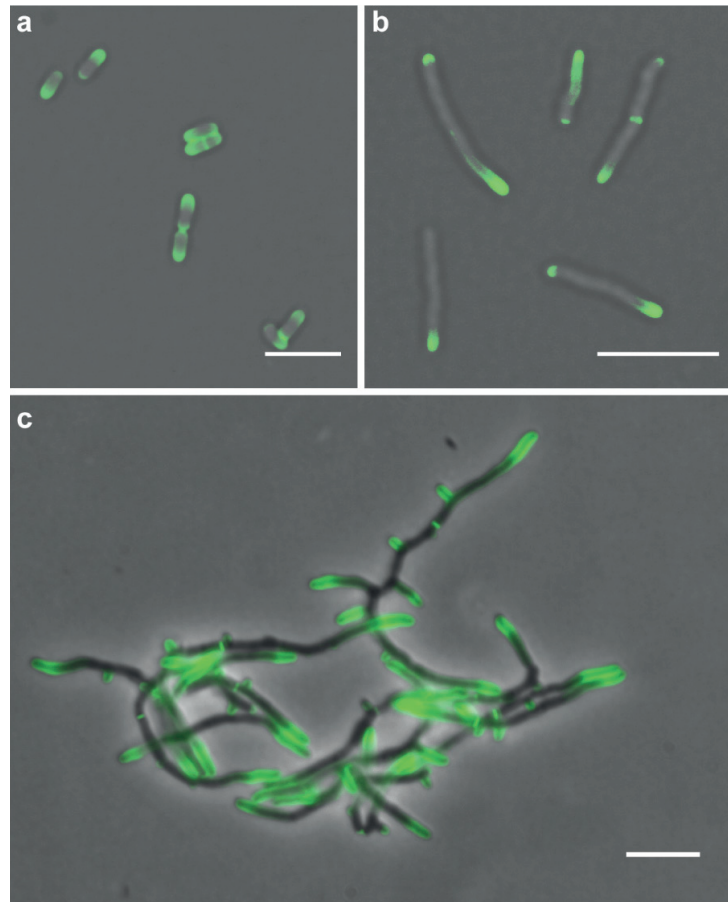
Supplementary Figure 1. The active fluorescent benzothiazinone analog **JN108** accumulates at mycobacterial cell poles. *M. smegmatis* (a) or *M. tuberculosis* (b) bacteria were cultured in microfluidic devices and were subsequently stained with **JN108** or the inactive form (**JN105**). The arrows point to the polar localization seen with **JN108**. The arrowheads indicate regions of non-polar labeling where the cellular material is leaking out. The white scale bar shown at bottom left represents 5 μm . Also see **Movies S1-S3**.



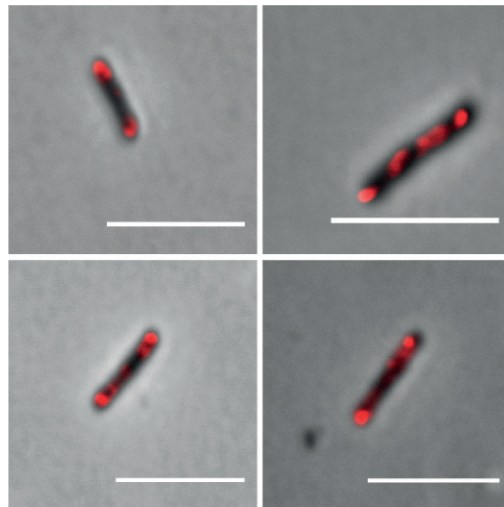
Supplementary Figure 2. Labeling *M. smegmatis* cells expressing Wag31-GFP with **JN108**. Arrows highlight cell poles where Wag31-GFP colocalizes with **JN108**. Scale bar 5 μ m.



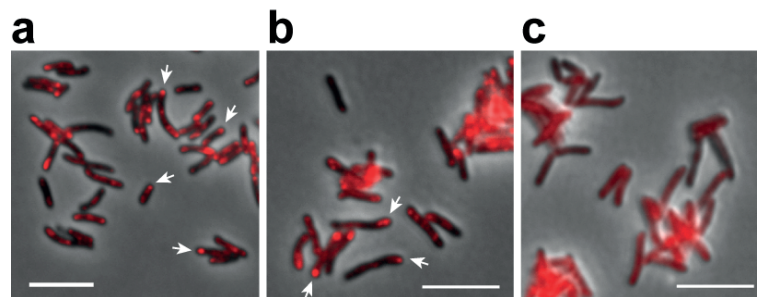
Supplementary Figure 3. Labeling *M. marinum* *in vitro* with **JN108**. BTZ-sensitive *M. marinum* carrying Rv3789-GFP (a) displays polar **JN108** labeling (arrows) while BTZ-resistant *M. marinum* carrying Rv3789-mNeonGreen (b) displays only a faint uniform **JN108** labeling. The green channel shows the plasma membrane and red channel shows **JN108** fluorescence. Scale bar 5 μ m.



Supplementary Figure 4. Staining of nascent peptidoglycan indicating growth by tip extension in (a) *C. glutamicum*, (b) *M. smegmatis* and (c) *N. farcinica*. Merge of phase contrast or trans-light micrographs with green fluorescence channel (Rhodamine-110). Scale bars 5 μm.



Supplementary Figure 5. Labeling non-growing *M. tuberculosis* (streptomycin-starved 18b) with **JN108**. *M. tuberculosis* strain 18b was passaged three times without streptomycin until the culture reached a stable OD. JN108 was added and bacteria were incubated for 24h before preparation for microscopy. Micrographs represent a merge of the phase contrast image (grey) and red fluorescence channel (red). Scale bars 5 μ m.



Supplementary Figure 6. Labeling *M. tuberculosis* with **JN108**. *M. tuberculosis* strain H37Rv wild-type (a, b) or BTZ-resistant (NTB1, c) were exposed overnight to **JN108**. (a) and (b) are micrographs from two independent experiments and display similar polar labeling while BTZ-resistant bacteria display uniform background staining. **JN108** fluorescence is shown in red and phase contrast in grey. Scale bars 5 μ m.

Supplementary Movie 1. Timelapse imaging of *M. smegmatis* exposed to JN108

Representative timelapse microscopy movie in which *M. smegmatis* bacteria expressing GFP were grown in the microfluidic device over a period of 50 h, under a constant flow of 7H9 medium. The bacteria were exposed to **JN108** from 10.25 h to 33 h. Images were recorded every 15 min, on the green (GFP) and red (TAMRA - **JN108**) channels. Time is indicated on the top right. Scale bar is shown on the bottom right. The signal on the red channel has been normalized over time to allow for better visualization against the background

Supplementary Movie 2. Timelapse imaging of *M. smegmatis* exposed to JN105

Representative timelapse microscopy movie in which *M. smegmatis* bacteria expressing GFP were grown in the microfluidic device over a period of 17 h, under a constant flow of 7H9 medium. The bacteria were exposed to JN105 from 5.75 h to 16.25 h. Images were recorded every 15 min, on the green (GFP) and red (TAMRA - **JN105**) channels. Time is indicated on the top right. Scale bar is shown on the bottom right. The signal on the red channel has been normalized over time to allow for better visualization against the background. Some out-of-focus images have been removed from the time-lapse series.

Supplementary Movie 3. Timelapse imaging of *M. tuberculosis* exposed to JN108

Representative timelapse microscopy movie in which *M. tuberculosis* bacteria expressing GFP were grown in the microfluidic device over a period of 232 h, under a constant flow of 7H9 medium. The bacteria were exposed to **JN108** from 1 h to 126 h. Images were recorded every 60 min, on the green (GFP) and red (TAMRA - **JN108**) channels. Time is indicated on the top right. Scale bar is shown on the bottom right. The signal on the red channel has been normalized over time to allow for better visualization against the background. Some out-of-focus images have been removed from the time-lapse series. The period of growth before addition of **JN108** is not shown.

The Supporting Information and the movies are available free of charge on the ACS Publications website at DOI: 10.1021/acscchembio.8b00790.

References

1. Hatanaka, Y., Hashimoto, M., and Kanaoka, Y. (1994) A novel biotinylated heterobifunctional cross-linking reagent bearing an aromatic diazine. *Bioorg. Med. Chem.* 2, 1367–1373.
2. Makarov, V. A. (2011) Process for the preparation of 2-amino-substituted 1,3-benzothiazine-4-ones; patent WO2011132070A1.
3. Neres, J., Pojer, F., Molteni, E., Chiarelli, L. R., Dhar, N., Boy-Röttger, S., Buroni, S., Fullam, E., Degiacomi, G., Lucarelli, A. P., Read, R. J., Zaroni, G., Edmondson, D. E., De Rossi, E., Pasca, M. R., McKinney, J. D., Dyson, P. J., Riccardi, G., Mattevi, A., Cole, S. T., and Binda, C. (2012) Structural basis for benzothiazinone-mediated killing of *Mycobacterium tuberculosis*. *Sci. Transl. Med.* 4, 150ra121.
4. Siegrist, M. S., Whiteside, S., Jewett, J. C., Aditham, A., Cava, F., and Bertozzi, C. R. (2013) (D)-Amino acid chemical reporters reveal peptidoglycan dynamics of an intracellular pathogen. *ACS Chem. Biol.* 8, 500–505.

Chapter 3.

Fluorescent Benzothiazinone Analogues to Detect Mycobacteria *in vivo*

This chapter explains the application of the probes described in the previous chapter in an attempt to detect mycobacteria in live infected zebrafish embryos and mice. Although written in a manuscript format, the following are unpublished data.

INTRODUCTION

The 8-nitro-benzothiazinones (BTZs) BTZ043¹ and PBTZ169² (macozinone) are promising new anti-tuberculosis (TB) drugs with an MIC₉₉ of 1 and 0.3 ng/mL, respectively. BTZs are potent inhibitors of decaprenyl-phospho- β -D-ribose oxidase (DprE1), an essential enzyme required for the synthesis of the cell wall in mycobacteria. BTZs form irreversible covalent adducts with Cys387 in DprE1^{3,4} and the 2-substituent of the BTZ core can be coupled with fluorophores without suppressing their anti-mycobacterial activity.⁵ **JN108**, a TAMRA-labelled PBTZ molecule has successfully been used to label DprE1 *in vitro* and in living BTZ-sensitive actinobacteria, highlighting the polar and periplasmic localization⁶ of DprE1. We further synthesized a PBTZ-molecule linked to the near-infrared (NIR) fluorophore Dy-750, which has a maximal excitation and emission at 747 and 776 nm, respectively. This fluorescent probe, named **JN139**, has an MIC₉₉ against *M. tuberculosis* of 80 ng/mL suggesting that despite coupling with Dy-750, the molecule can still bind to DprE1 and exhibit a bactericidal effect, as observed with **JN108**.

We sought to assess the feasibility of mycobacterial detection in two models of mycobacterial infection commonly used for *in vivo* studies of TB, namely, *M. marinum*-infected zebrafish embryos and *M. tuberculosis* in the lungs of living infected mice. For the latter, the utilization of **JN139** is recommended as NIR fluorophores permit deeper *in vivo* imaging, since the scattering and absorption of light by mammalian tissues drops above 700 nm.⁷ On the other hand, the transparency of zebrafish embryos permits the utilisation of **JN108** (TAMRA maximal emission is around 580 nm) and observation with confocal microscopy is sufficient to visualize the probe *in vivo*. The feasibility of these two approaches for mycobacterial detection is investigated in this chapter. The results obtained are presented and the limitations of the technique are discussed.

RESULTS

Visualization of *M. marinum* in zebrafish embryos with JN108

We previously described that **JN108**, a TAMRA-coupled PBTZ molecule, specifically labels DprE1 in several actinobacteria and mycobacteria, including *M. marinum*.⁵ We therefore aimed to test if **JN108** could detect *M. marinum* in infected zebrafish embryos. To do so, 24 h old zebrafish embryos were infected with green fluorescent *M. marinum* constitutively producing the mNeonGreen protein^{8,9} (*M. marinum* mNeon), via caudal vein microinjection. The bacteria were visible in the embryos by examination under a confocal microscope, as early as 24 h post infection (Figure 1). At this point, a solution of **JN108** was microinjected in the common cardinal vein

(CCV) of the embryos. Note that injection in the CCV is easier than injection in the caudal vein for embryos older than 30 h post fertilization. The fluorescent probe was uniformly distributed in the tissues of the fish 2 h after the injection of **JN108**, except in the notochord, as can be seen in the red channel in Figure 1a. This indicates that injection in the CCV permits a global distribution of the dye in the embryo via the circulatory system. No fluorescence was visible in the red and green channels for uninfected embryos that did not receive **JN108**, showing that red and green fluorescence is specific for **JN108** and *M. marinum* mNeon, respectively. Two hours after administration of **JN108**, red and green fluorescence did not co-localize, suggesting that the probe had not labelled the bacteria at this time point. Similar observations were performed 24 h post injection of **JN108**, where the red fluorescence intensity in muscular tissue had slightly decreased. Despite adjustment of contrast, **JN108** appeared to have remained uniformly distributed, whereas *M. marinum* mNeon formed clusters, visible in green fluorescence (Figure 1c). A view with a lower magnification 48 h post administration of **JN108** showed that the fluorescent probe had mainly accumulated in the yolk of the 4 d old embryos but still did not precisely co-localize with the mycobacteria. These observations suggest that despite an appropriate distribution of **JN108** following microinjection in *M. marinum*-infected zebrafish embryos, the probe cannot specifically detect *M. marinum* in this context.

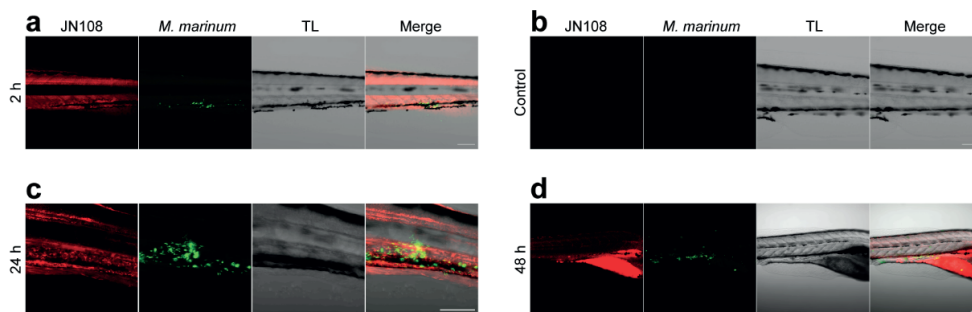


Figure 1. Visualization of *M. marinum* in infected zebrafish embryos. (a) Zebrafish embryo infected with *M. marinum* mNeon and receiving **JN108**, imaged 2 h after injection of the probe. (b) Non-infected embryos imaged without administration of **JN108**, validating specific fluorescent signals seen in panel a. (c, d) Infected embryos imaged 24 h (panel c) and 48 h (panel d) after injection of **JN108**. The contrast was adjusted for the red fluorescence channel to highlight the localization of **JN108**. Indications at left specify the time at which images were acquired, with respect to initial **JN108** injection. TL = trans-illumination. Scale bars: 100 μm .

Visualization of *M. tuberculosis* in infected mice with JN139, a near-infrared PBTZ derivative

The Photon Imager platform allows for multiplexing of fluorescence and bioluminescence imaging modalities for *in vivo* imaging in small animals. The aim of this study was to test whether the NIR fluorescent PBTZ analogue **JN139** could detect *M. tuberculosis* in the lungs of infected mice. If this were the case, NIR fluorescent (**JN139**) and bioluminescent (*M. tuberculosis* Lux, described in detail in chapter 5) signals should co-localize in the thoracic area of the infected animals.

Thirty five days after low dose aerosol infection of SCID Hairless Outbred (SHO) mice with *M. tuberculosis* Lux, an autobioluminescent reporter (see Chapter 5 of this thesis), the animals received several doses of **JN139** (one dose = 2 µg) via the intraperitoneal route. A group of non-infected mice was treated similarly to serve as comparison. Previous trials with intravenous (tail vein) injections resulted in a weak distribution of **JN139** in the body and a rapid accumulation of the probe in the liver, as measured by whole body fluorescence imaging (data not shown). Mice were imaged immediately after **JN139** injection and a bright fluorescent signal was observable on the entire abdominal area, confirming successful intraperitoneal injection. 16 h later, the mice were imaged again and the fluorescence had slightly decreased in the abdomen (Figure 2d) but no signal was visible in the thoracic area. A second dose of **JN139** was administered and subsequent imaging 17 h later led to similar observations. Finally, a double dose of **JN139** was injected. To allow additional time for the distribution of the probe and to eliminate the excess of **JN139**, mice were imaged 30 h after the last injection. As can be seen in Figure 1b and c, the fluorescence mainly focalized in the abdomen. However, luminescence measurements indicated a precise and clear signal in the thorax of infected mice (Figure 2c), absent in uninfected mice. The fluorescent and luminescent signals did not co-localize, suggesting that **JN139** had not labelled *M. tuberculosis in vivo*.

Quantitative *ex vivo* fluorescence and luminescence measurements were performed subsequently on excised lungs from mice receiving **JN139** (Figure 2e). An increase in luminescence intensity of more than two orders of magnitude was observed between lungs from uninfected and infected mice, suggesting that the *M. tuberculosis* Lux reporter permits quantitative evaluation of the bacterial load with luminescence measurements. An average of $1.128 \cdot 10^8$ CFU/lung was evaluated for these organs after plating and culture of lung homogenates. In contrast, NIR fluorescence intensities were similar between lungs from uninfected and infected mice. These observations indicate yet again that **JN139** cannot quantitatively label *M. tuberculosis* in the murine model of tuberculosis infection or that labeling is below the limit of detection.

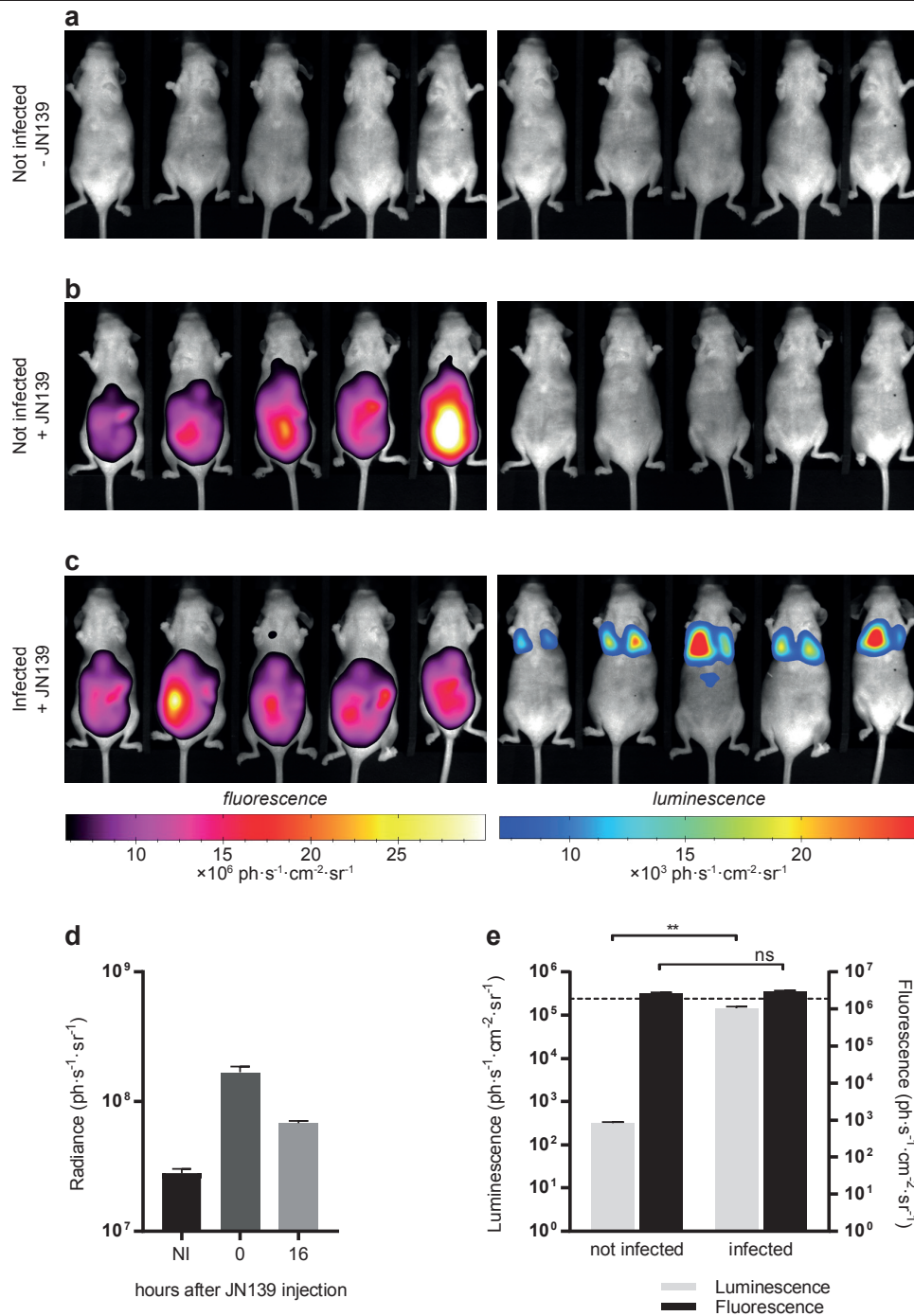


Figure 2. Multimodal imaging of tuberculosis infection. (a-c) The pictures were taken during the last imaging session (just before sacrifice) with mice receiving **JN139** (panels b and c) in comparison with control animals (panel a). Panels on the left show fluorescence (**JN139**) and panels on the right display luminescent signals (*M. tuberculosis* Lux). Only mice from panel c are infected with *M. tuberculosis* Lux. Images display black and white photographs and the fluorescent, respectively luminescent signals are overlaid in false colour. (d) Quantification of the fluorescence in the abdomen of mice receiving **JN139** via the intraperitoneal route at indicated time points and comparison with non-injected mice (NI). (e) *Ex vivo* luminescence and fluorescence quantification on excised lungs for mice receiving **JN139**. The dashed line represents the average fluorescence on lungs from control mice that did not receive **JN139**. Bars show averages and S.E.M. ns = non-significant, ** $P > 0.001$

DISCUSSION

We have recently demonstrated that several fluorophore-coupled benzothiazinone core molecules could specifically and covalently label DprE1 *in vitro* in bacterial lysates.⁵ **JN108**, a probe with a TAMRA fluorochrome attached on a PBTZ moiety via a hydrophobic linker, could label DprE1 at the poles of live BTZ-sensitive bacteria, such as *M. smegmatis*, *M. tuberculosis*, *M. marinum* and *N. farcininca*. Besides precisely labelling DprE1, fluorescent PBTZ molecules have the potential for detection of BTZ-sensitive mycobacteria in more complex settings. This was investigated in the present study for *in vivo* imaging, in the zebrafish embryo model of *M. marinum* infection and in mice infected with luminescent *M. tuberculosis*.

In the first case, green fluorescent *M. marinum* bacteria were easily visualized with confocal fluorescence microscopy at different time points post infection, as previously described.^{10–12} Injection of **JN108** 24 h post infection in the CCV proved to be an optimal route of administration as the probe had distributed along the organism via the circulation and could be tracked with fluorescence microscopy. 24 and 48 h post injection, however, the fluorescent probe had mainly accumulated in the yolk and no clear co-localization with the bacteria was observed. This suggests that **JN108** is not sensitive enough to detect *M. marinum* in infected zebrafish embryos using the method described here. Notably, DprE1, the target of **JN108**, is only present at the poles of the bacteria. This means that **JN108** labelling is restricted to the tips of the bacilli, therefore weakening the limit of detection. In the zebrafish model, the limit of detection seems situated below the background level of fluorescence, rendering the bacteria invisible in the red fluorescence channel and precluding the utilization of **JN108** in this context.

For mycobacterial detection in the mouse model, a near-infrared fluorescent PBTZ derivative was designed and produced by coupling a Dy-750 dye to a PBTZ pharmacophore. Dy-750 has a maximum of emission above 750 nm, which is particularly suitable for fluorescence imaging in rodents, as mentioned earlier. The biodistribution of the probe, however, gave rise to considerable issues. Intravenous injection led to rapid accumulation in the liver and intraperitoneal administration created a large zone of fluorescence in the abdominal area, while no specific signal was visible in the thoracic area of the infected mice. In contrast, a clear luminescent signal could be recorded *in vivo* and *ex vivo* and this is further discussed in chapter 5 of this thesis. The fluorescence measured on explanted lungs did not corroborate the true bacterial load evaluated in parallel by luminescence and by enumeration of CFUs. Dy-750-based probes remain a suitable choice for *in vivo* imaging as no background fluorescence from the skin or the food in the gastrointestinal tract overlapped with the present measurements.

Although fluorescent PBTZ-based probes are extremely selective towards BTZ-sensitive bacteria such as *M. tuberculosis* and *M. marinum*, the global intensity of labelling remains weak, rendering mycobacterial detection difficult *in vivo*. The biodistribution and background fluorescence of unbound probe also impairs detection. Alternatively, enzymatically switchable probes might solve these issues, as recently suggested¹³⁻¹⁵ and as discussed in the concluding chapter of this work.

METHODS

Bacterial strains and culture conditions

M. tuberculosis and *M. marinum* strains were grown in Middlebrook 7H9 medium (Difco) supplemented with 0.2% glycerol, 10% albumin-dextrose-catalase (ADC) and 0.05% Tween-80 or on solid 7H10 agar plates containing 0.5% glycerol and 10% oleic acid-albumin-dextrose-catalase (OADC). *M. tuberculosis* was cultured at 37°C and *M. marinum* at 30°C. Liquid cultures were incubated with orbital shaking at 100 rpm. Hygromycin (HYG, 50 µg/mL) was added to culture medium when appropriate.

Construction of the mycobacterial reporter strains

Luminescent *M. tuberculosis* H37Rv (*M. tuberculosis* Lux) was obtained by transformation of the integrative plasmid pEG200,¹⁶ a gift from Neeraj Dhar. The *mNeonGreen* gene^{8,9} was PCR amplified and cloned in a pSMT3¹⁷ vector to generate a replicative plasmid constitutively (under the promoter P_{hsp60}) producing the fluorescent protein. The plasmid was transformed into wild type *M. marinum* strain M and its BTZ-resistant mutant⁵ to generate the *M. marinum* mNeon reporters. Transformation of DNA by electroporation was performed as described elsewhere.¹⁸

Infection of zebrafish embryos and probe injection

Zebrafish embryos were infected as previously described.¹⁹ Briefly, 24 h old *Danio rerio* (AB) embryos were manually dechorionated and aligned on a custom-made cavity-inlaid agarose bed covered with E3 medium²⁰ (5 mM NaCl, 0.17 mM KCl, 0.33 mM CaCl₂, 0.33 mM MgSO₄) containing 0.4 mg/mL MS-222 (Sigma). 1-2 nL of an *M. marinum* mNeon suspension containing ~300 bacteria was microinjected in the caudal vein of the anesthetized embryos using a heat-pulled glass capillary connected to a pneumatic PicoPump PV820 (World Precision Instruments). The embryos were allowed to recover in fresh E3 medium and were kept at 28°C. 24 h post infection, the embryos were anesthetized as indicated above and received 1-2 nL of **JN108**⁵ (0.05 mg/mL) by microinjection in the common cardinal vein (CCV) as described elsewhere.²¹ Zebrafish embryos were recovered in MS-222-free E3 medium and prepared for imaging.

Imaging of infected zebrafish embryos

2, 24 or 48 h after injection of the **JN108** probe, the zebrafish embryos were anesthetized with 0.4 mg/mL MS-222 in E3 medium. Embryos were embedded in 1.2% low melting agarose in an 8-chambered coverslip (Ibidi) and the solidified agarose was covered with a layer of E3 containing 0.4 mg/mL MS-222. Samples were visualized with a Zeiss LSM700 inverted confocal microscope equipped with Plan-Apochromat objectives (20× NA 0.8 (air), 40× NA 1.3 and 63× NA 1.4 (oil)). Images were processed with the ImageJ software v1.52h.

Infection of mice and probe injection

5-6 week old female SCID Hairless Outbred (SHO) (Charles River) were infected with *M. tuberculosis* Lux by aerosol exposure in a Madison chamber. 35 d post infection **JN139** (2 µg in 100 µL PBS containing 0.05% Tween-80) was administered by intraperitoneal injection. Mice were imaged as described below, immediately after injection of **JN139**. 36 d post infection, the same mice were imaged again and received another dose of **JN139**. The following day, mice were imaged and received a final double dose of **JN139**. Animals were imaged 1 and 2 d later without receiving further **JN139**. Experiments involving animals were performed under ABSL3 containment and approved by the Swiss Cantonal Veterinary Authority (licence number 3082). Experiments involving mice were performed once, with 5 animals per group infected and treated identically.

Enumeration of bacteria in the lungs

After the final session of *in vivo* imaging, animals were euthanized by cervical dislocation while still under anaesthesia. Lungs were aseptically excised, imaged in a sealed Petri dish and homogenized in 2 mL of PBS containing 0.05% Tween 80. Serial 10-fold dilutions of lung homogenates were plated on 7H10 agar containing 16 µg/mL nalidixic acid (sodium salt), 4 µg/mL azlocillin (sodium salt) and 10 µg/mL cycloheximide (all from Sigma). Plates were cultured at 37°C for 4-5 weeks before CFU enumeration.

***In vivo* and *ex vivo* imaging of mice**

In vivo imaging of live animals and *ex vivo* imaging of lungs was performed with a Photon Imager Optima (Biospace Labs, France). Acquisitions were performed with Photo Acquisition (version 3.4.5.1169) software. Luminescence was recorded without filters for 5 min. Fluorescence (10 s of acquisition) was measured with excitation and emission band-pass filters of 725-750 nm and 780-815 nm cut-off, respectively. Background fluorescence was quantified with a filter of 675-700 nm

cut-off. Luminescent or fluorescent signals were superimposed with black and white photographs of the specimen using M3 Vision (version 1.1.2.30843).

For imaging live animals, mice were anaesthetized with 5% isoflurane in an induction chamber and transferred on the heated stage (37°C) of the Photon Imager Optima. Mice were placed on their back or slightly tilted towards their left side in front of a gas manifold to maintain them under isoflurane (reduced to 2%) anaesthesia during image acquisition.

For quantification of the photonic signal, a region-of-interest (ROI) tool was used. Extracted lungs were imaged in a sealed plastic Petri dish and an ROI was drawn with the spline tool around the border of each organ. Radiance is expressed as photons per second per square centimetre per steradian ($\text{ph}\cdot\text{s}^{-1}\cdot\text{cm}^{-2}\cdot\text{sr}^{-1}$).

Statistics

Statistical analysis was carried out with GraphPad Prism version 7.02. For *in vivo* experiments, every group of mice contained $n = 5$ animals and all of them were included in statistical analyses. When two groups were compared, a Mann Whitney test was used. When more than two groups were compared, an ordinary one-way ANOVA followed by a Tukey's multiple comparisons test were performed.

REFERENCES

1. Makarov, V. *et al.* Benzothiazinones kill *Mycobacterium tuberculosis* by blocking arabinan synthesis. *Science* **324**, 801–804 (2009).
2. Makarov, V. *et al.* Towards a new combination therapy for tuberculosis with next generation benzothiazinones. *EMBO Mol. Med.* **6**, 372–383 (2014).
3. Neres, J. *et al.* Structural basis for benzothiazinone-mediated killing of *Mycobacterium tuberculosis*. *Sci. Transl. Med.* **4**, 150ra121 (2012).
4. Trefzer, C. *et al.* Benzothiazinones are suicide inhibitors of mycobacterial decaprenylphosphoryl- β -D-ribofuranose 2'-oxidase DprE1. *J. Am. Chem. Soc.* **134**, 912–915 (2012).
5. Sommer, R. *et al.* Fluorescent benzothiazinone analogues efficiently and selectively label DprE1 in mycobacteria and actinobacteria. *ACS Chem. Biol.* **13**, 3184–3192 (2018).
6. Brecik, M. *et al.* DprE1 is a vulnerable tuberculosis drug target due to its cell wall localization. *ACS Chem. Biol.* **10**, 1631–1636 (2015).
7. Filonov, G. S. *et al.* Bright and stable near-infrared fluorescent protein for *in vivo* imaging. *Nat. Biotechnol.* **29**, 757–761 (2011).
8. Hostettler, L. *et al.* The bright fluorescent protein mNeonGreen facilitates protein expression analysis *in vivo*. *G3: Genes, Genomes, Genet.* **7**, 607–615 (2017).
9. Shaner, N. C. *et al.* A bright monomeric green fluorescent protein derived from *Branchiostoma lanceolatum*. *Nat. Methods* **10**, 407–409 (2013).
10. van Leeuwen, L. M., van der Sar, A. M. & Bitter, W. Animal models of tuberculosis: zebrafish. *Cold Spring Harb. Perspect. Med.* **5**, a018580 (2014).
11. Benard, E. L. *et al.* Infection of zebrafish embryos with intracellular bacterial pathogens. *J. Vis. Exp.* e3781 (2012).
12. Takaki, K., Davis, J. M., Winglee, K. & Ramakrishnan, L. Evaluation of the pathogenesis and treatment of *Mycobacterium marinum* infection in zebrafish. *Nat. Protoc.* **8**, 1114–1124 (2013).

13. Kong, Y. *et al.* Imaging tuberculosis with endogenous beta-lactamase reporter enzyme fluorescence in live mice. *Proc. Natl. Acad. Sci. U. S. A.* **107**, 12239–12244 (2010).
14. Kong, Y. & Cirillo, J. D. Fluorescence imaging of mycobacterial infection in live mice using fluorescent protein-expressing strains. *Methods Mol. Biol.* **1790**, 75–85 (2018).
15. Yang, H.-J. *et al.* Real-time imaging of *Mycobacterium tuberculosis* using a novel near-infrared fluorescent substrate. *J. Infect. Dis.* **215**, 405–414 (2017).
16. Sharma, S. *et al.* Simple and rapid method to determine antimycobacterial potency of compounds by using autoluminescent *Mycobacterium tuberculosis*. *Antimicrob. Agents Chemother.* **58**, 5801–5808 (2014).
17. O’Gaora, P. Expression of genes in mycobacteria in *Mycobacteria Protocols* (eds. Parish T., Stoker N.G.) 261–273 (Humana Press, Totowa, NJ, 1998).
18. Parish, T. & Stoker, N. G. Electroporation of mycobacteria. *Methods Mol. Biol.* **101**, 129–144 (1998).
19. Stoop, E. J. M. *et al.* Zebrafish embryo screen for mycobacterial genes involved in the initiation of granuloma formation reveals a newly identified ESX-1 component. *Dis. Model. Mech.* **4**, 526–536 (2011).
20. Brand, M. & Granato, M. Keeping and raising zebrafish in *Zebrafish: A Practical Approach* (eds. Nusslein-Volhard, C. and Dahm, R.) 7–37 (Oxford Univ. Press, Oxford, 2002).
21. Smith, S. J., Horstick, E. J., Davidson, A. E. & Dowling, J. Analysis of zebrafish larvae skeletal muscle integrity with Evans blue dye. *J. Vis. Exp.* e53183 (2015).

PART II

***IN VIVO* IMAGING**

Chapter 4.

Monitoring Tuberculosis Drug Activity in Live Animals by Near-Infrared Fluorescence Imaging

This chapter is a manuscript in preparation (2019).

Contributions: design and execution of the experiments, data generation and analysis, manuscript preparation

ABSTRACT

Worldwide, tuberculosis (TB) is the leading cause of death due to infection with a single pathogenic agent, *Mycobacterium tuberculosis*. In the absence of an effective vaccine, new, more powerful antibiotics are required to halt the growing spread of multidrug-resistant strains and to shorten the duration of TB treatment. However, assessing drug efficacy at the preclinical stage remains a long and fastidious procedure that delays progression of drugs down the pipeline and towards the clinic. In this investigation, we report the construction, optimization and characterisation of genetically engineered near-infrared fluorescent reporter strains of the pathogens *Mycobacterium marinum* and *Mycobacterium tuberculosis* that enable direct visualization of bacteria in infected zebrafish and mice, respectively. Furthermore, we show that the fluorescence level accurately reflects the bacterial load, as determined by colony forming unit enumeration, thus enabling the efficacy of antibiotic treatment to be assessed in live animals in real time.

INTRODUCTION

Worldwide, tuberculosis (TB) remains one of the top 10 causes of death and the leading cause due to a single infectious agent, namely the bacillus *Mycobacterium tuberculosis*.¹ Despite major progress since 1993 when the World Health Organisation (WHO) declared TB a global health emergency, 10 million new cases and 1.6 million deaths were estimated in 2017 alone. The absence of an effective vaccine preventing TB in adults and the increasing number of multidrug-resistant (MDR) TB cases make this disease a serious global health threat. Short course chemotherapy is available for drug-sensitive TB but this requires the administration of four first-line drugs (rifampicin, isoniazid, ethambutol and pyrazinamide) over 6 months while the treatment of drug-resistant TB is considerably longer, more expensive and has more side effects. “Intensified research and innovation” is one of three pillars of the WHO’s End TB Strategy, and covers the discovery and the development of new antibiotics to tackle drug-resistant bacteria, to cut the risk of developing active and contagious TB among the 1.7 billion people already latently infected, and to develop simpler and shorter regimens for treating the disease.¹

During drug development and translation to clinical trials, preclinical animal models are required to evaluate the efficacy of candidate compounds. Mice have been a model of choice for the elucidation of immunological and pathological pathways and can also serve to study the activity of drugs and vaccines.² Aerosol exposure of mice with a suspension of bacteria enables a homogenous infection of several groups of animals with a route mimicking natural infection.^{2,3} It is particularly

important to minimize interindividual variation to allow appropriate comparison of different treatments or regimens among a cohort. This model, although it can demonstrate an efficient reduction of the bacterial burden following the treatment, is long, labour intensive and provides only retrospective information on the bacterial loads in the mice. The mouse model of chronic TB typically involves Balb/c or C57Bl/6 mice aerogenically infected with an *M. tuberculosis* suspension. 4-5 weeks post infection, the bacterial burden in the lungs of these strains stabilizes and treatment is usually administered orally for at least 4 weeks, followed by plating lung homogenates for colony forming unit (CFU) enumeration. Importantly, as CFU assays are endpoint measurements requiring the euthanasia of the animals, it is not possible to perform real time evaluation of the bacterial burden, longitudinal follow up and assessment of long term effects of the treatment, or to evaluate the kinetics of the infection upon treatment. In addition, many animals are required per experiment in order to gather statistically significant data on drug efficacy, which is arguable from an ethical point of view.

In contrast, *in vivo* optical imaging of TB infection in mice can provide this information. *In vivo* optical (or biophotonic) imaging involves the measurement of photons emitted by a particular source to evaluate its size and spatial location.⁴ The two major modalities are bioluminescence, in which photons are emitted during a chemical reaction catalysed by luciferase, and fluorescence. In the latter, fluorescent proteins (FPs) or dyes reemit photons during the relaxation from the excited to the ground state, following irradiation with light at an appropriate wavelength. *In vivo* fluorescence imaging methods are limited by autofluorescence, absorption and scattering of photons by mammalian tissues, as well as by light penetration. This is particularly important in deep tissue imaging, as is the case for lungs, limiting the applicability of the method to proteins or dyes (in fluorescence imaging) with emission shifted towards the near-infrared (NIR) range (above 650 nm), where tissue absorption and scattering are lowest.⁵⁻⁷ New NIR FPs have been engineered from bacterial phytochromes, which are photosensory receptors that absorb light in the far-red section of the spectrum.⁸⁻¹⁰ These NIR FPs are especially well suited for *in vivo* imaging as their spectra reside within the NIR tissue transparency window.¹¹ For example, the NIR FP iRFP has been successfully used for expression and imaging in live mice and excellent signal/background ratio has been achieved.^{9,12,13} iRFP has been used to track dissemination of bacteria in the gastrointestinal tract¹⁴, exemplifying its potential for imaging infectious diseases. However, this is the only report of *in vivo* imaging of an infection exploiting the protein iRFP.

In the case of mycobacterial infections, bioluminescent *M. tuberculosis* expressing the firefly luciferase gene could be visualized in the lungs of infected CB-17 SCID mice.^{15,16} Similarly, autoluminescent *M. tuberculosis* carrying the *luxCDABE* operon from *Photobacterium luminescens*

demonstrated the efficacy of several antibiotics *in vivo* in Balb/c mice, although not allowing whole body imaging.¹⁷ A red-shifted *M. tuberculosis* fluorescent reporter has been used for the quantification of the bacterial burden with a commercial IVIS system and for the precise localization of the bacteria with fluorescence molecular tomography.¹⁸ However, the study demonstrated the efficacy of an antibiotic only during the acute and progressive phase of tuberculosis infection and quantitative measurements could only be done on excised lungs. Reporter enzyme fluorescence using a fluorogenic β -lactamase substrate was reported to detect as few as 1000 CFUs in the lungs of mice, yet such a model depends on the adequate administration and distribution of an exogenous probe.¹⁹ Finally, monitoring of TB lesions has been accomplished with 2-deoxy-2-[¹⁸F]fluoro-D-glucose (FDG) positron emission tomography (PET) combined with computed tomography (CT) imaging in mice²⁰ and in non-human primates.²¹ FDG accumulates in metabolically active inflammatory cells and enables high resolution imaging of tuberculous lesion dynamics, albeit without providing direct quantitative information on the true bacterial load.

In this study, we exploit the recently described NIR FP iRFP for construction of reporters in *M. tuberculosis* and other mycobacteria. These strains permit a clear visualization of the bacteria in infected mice and zebrafish embryos. We report that the bacterial burden can be evaluated with NIR fluorescence measurement *in vivo* and that fluorescence levels *in vivo* and *ex vivo* correlate with the actual number of CFUs in the lungs of infected mice. Finally, we demonstrate that treatment efficacy and the subsequent reduction of the bacterial load can be tracked with fluorescence imaging. Here we describe for the first time a mouse model of tuberculosis with SCID Hairless Outbred (SHO) mice infected with NIR fluorescent *M. tuberculosis*. This model is applied for whole body *in vivo* fluorescence imaging and permits to assess the effect of several antibiotics on chronically infected living animals, which has until now been limited to quantitative measurements *ex vivo*, during the early progression of the disease.¹⁸ Overall, these results show the great potential of NIR fluorescence *in vivo* imaging for longitudinal studies, by allowing the kinetics of infection to be followed upon antibiotic administration, to reduce the number of animals required per experiment and to gain time in the process of drug development.

RESULTS

Mycobacteria carrying *iRFP* or *mIFP* emit NIR fluorescence when supplemented with biliverdin

Genes coding for NIR FPs derived from bacterial phytochromes have previously been expressed in mammalian cells, such as HEK293A⁸ or HeLa,⁹ in different bacteria (*Lactococcus lactis*, *Lactobacillus plantarum* and *Escherichia coli*)¹⁴ and in mice,¹³ but there are no reports of their use in mycobacteria yet. To assess expression of NIR FP genes in mycobacteria, the genes *iRFP*⁹ and *mIFP*¹⁰ were optimized for *M. tuberculosis* codon usage and cloned in episomal vectors under three strong mycobacterial promoters, namely G13²², P_{smyc}²³ and P_{hsp60}²⁴, to generate a collection of plasmids (Supplementary Table 1) and to select the brightest reporter. *M. smegmatis* cells transformed with *iRFP*- or *mIFP*-containing plasmids emitted fluorescence with a maximal intensity at 713 nm only when the growth medium was supplemented with biliverdin (BV), the obligate cofactor necessary for the protein to fluoresce (Fig. 1a and b). It is known that in eukaryotic cells, expression of a NIR FP gene is sufficient to generate fluorescence, as BV is ubiquitously present as the first product of heme degradation⁸. In the case of bacterial cultures however, no fluorescence could be measured without addition of BV exogenously. Wild-type bacteria grown in the presence of BV do not fluoresce confirming that the fluorescence measured in the reporter strains originates from successful expression of the NIR FP genes, maturation of the protein and incorporation of BV. As higher fluorescence intensity could be reached with *iRFP* than with *mIFP*, *iRFP* was selected for further optimization and expression in *M. smegmatis*, *M. marinum* and *M. tuberculosis*.

Co-expression of *iRFP* and *hO1* renders bacteria fluorescent in the absence of exogenous BV

It has been previously proposed that expressing the heme oxygenase 1 (*hO1*) gene could boost BV levels in mammalian cells expressing NIR FP genes.⁸ Heme oxygenase catalyses the degradation of heme to BV. Consequently, we sought to express *hO1* in mycobacteria to bypass the need for exogenous BV. The gene coding for the human heme oxygenase 1 was codon-optimized for expression in *M. tuberculosis* and cloned directly downstream of *iRFP* in the episomal plasmids described above (without adding a promoter or Shine Dalgarno sequence), to generate the NIR_G13, NIR_smyc and NIR_hsp strains (Supplementary Table 1). The new constructs were transformed into *M. smegmatis* and the transformants found to emit fluorescence without addition of BV or any other source of heme to the growth medium (Fig. 1c). Interestingly, colonies grown on 7H10 plates were slightly green after 4 days at 37°C (Supplementary Fig. 1). This suggests that expression of *hO1* in *M. smegmatis* created a bifurcation in mycobacterial heme metabolism to generate a pool of BV, directly available for incorporation in iRFP and thereby turn the colonies green. In order to qualitatively assess the fluorescence emitted by the bacteria, a culture of a NIR_smyc strain was subjected to fluorescence intensity scanning. The excitation and emission spectra agree with the data previously published for iRFP⁹ with measured excitation and emission maxima at 690 and 713 nm, respectively (Fig. 1d).

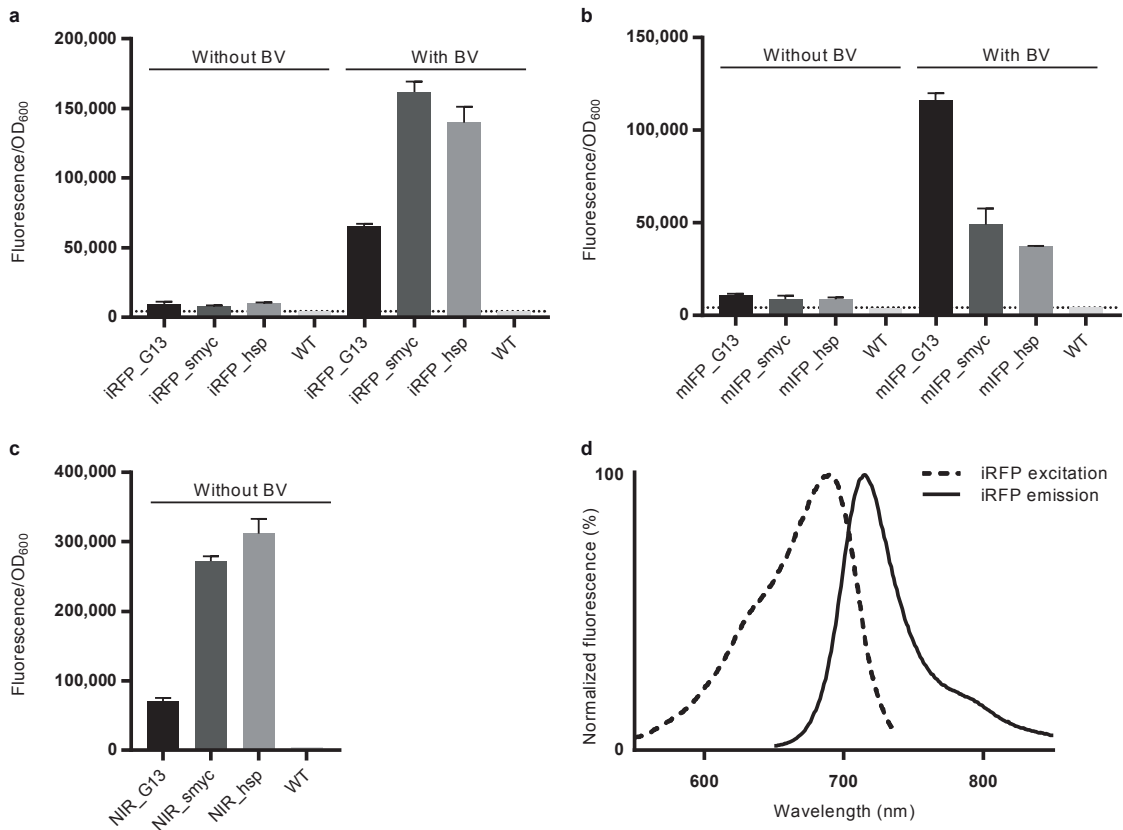


Fig. 1. *M. smegmatis* reporter strains emit NIR fluorescence. **a-c**, Fluorescence intensity measured at 713 nm for *M. smegmatis* expressing *iRFP* (**a**), *mIFP* (**b**), cultured overnight with or without BV, or NIR *M. smegmatis* reporters without BV supplementation (**c**). The fluorescence intensity was measured with a microplate reader and normalized according to the cell density for each well. The dotted line indicates the background autofluorescence recorded in WT bacteria in the same conditions. Data represent averages and s.e.m. for $n = 4$ independent clones per group. **d**, Fluorescence excitation and emission spectra of *M. smegmatis* NIR_smyc reporter.

A NIR *M. marinum* strain can be quantified in the zebrafish model of mycobacterial infection

Since constructs containing *iRFP* and *hsl* under the control of different promoters enabled us to measure strong NIR fluorescence in *M. smegmatis* we tested whether the optimized system was suitable for use in other mycobacteria. Plasmids pNIR_G13, pNIR_smyc and pNIR_hsp were electroporated into *M. marinum* strain M. Once again, transformants carrying the constructs exhibited a faint green color and this was most pronounced with pNIR_G13. Several independent transformants were grown in liquid culture to measure the fluorescence intensity of the different reporters. In *M. marinum*, expression under G13 control led to 3-fold higher fluorescence intensity than expression from P_{smyc} or P_{hsp} , hence *M. marinum* NIR_G13 was selected for further analyses (Fig. 2a). To test whether NIR mycobacteria can be visualized *in vivo*, 24 h old zebrafish embryos were infected with *M. marinum* NIR_G13 by microinjection of ~300 bacterial cells into the caudal vein.^{25,26} Bacteria could be observed with confocal microscopy in the muscular tissues of embryos 3 days post infection (dpi, Fig. 2b). In addition, a group of infected larvae was exposed to the experimental TB drug macoquinone (MCZ, 25 ng/mL added in E3²⁷) starting 1 dpi and continuing to the end of the experiment. After 4 days of infection, single embryos were distributed into the wells of a 96-well plate and NIR fluorescence measured. The average NIR fluorescence intensity for larvae treated with MCZ for 3 days corresponded to the baseline measured in uninfected fish. For the untreated group, however, significantly higher fluorescence levels were recorded (Fig. 2c). The average number of CFUs recovered from untreated fish was 4 log-fold higher than for embryos exposed to MCZ (Fig. 2d), thus corroborating the fluorescence measurements. These observations suggest that NIR *M. marinum* can be used for quantitative evaluation of the bacterial burden in infected zebrafish embryos and highlight the potential of NIR reporters for anti-mycobacterial drug development.

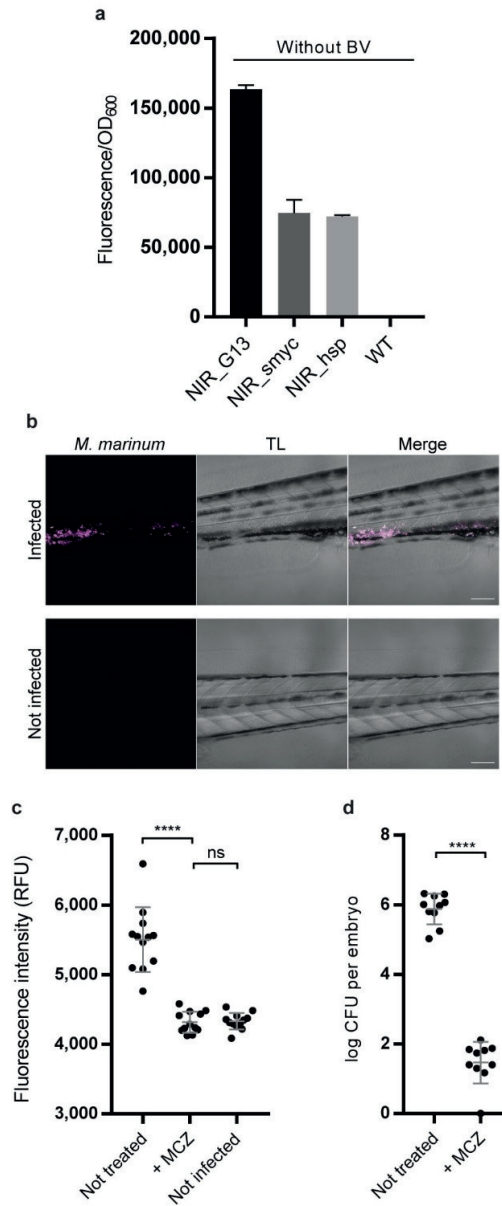


Fig. 2. NIR fluorescent *M. marinum* can be visualized and quantified in infected zebrafish embryos. **a**, Measurement of NIR fluorescence in cultures of *M. marinum* transformed with the indicated reporter constructs; $n = 3$ independent transformants per measurement. Bars show averages and s.e.m. **b**, Single plane confocal micrographs showing NIR *M. marinum* in zebrafish embryos at 3 dpi. Bacteria are visualized in NIR fluorescence (left), a gray picture (middle) is taken with trans-illumination (TL) and merged channels are shown at right. The bottom panel is an uninfected larva, highlighting specific fluorescence emitted by the bacteria (displayed in magenta). Scale bar, 100 μm . **c**, NIR fluorescence measurement of live infected zebrafish embryos with or without MCZ treatment. **d**, CFUs recovered from infected embryos with or without MCZ treatment. Each dot corresponds to one embryo and $n = 12$ (**c**) or $n = 10$ (**d**) elements per group. Bars show averages and standard deviations. **** $P < 0.0001$, ns = not significant.

Fluorescence in *M. tuberculosis* NIR reporters correlates with cell density and viability

In *M. tuberculosis*, expression with G13 and P_{smyc} led to reproducibly higher fluorescence levels than expression with P_{hsp}, hence NIR_G13 and NIR_smyc were selected for further analyses (Fig. 3a). The growth rate of *M. tuberculosis* NIR_G13 and NIR_smyc *in vitro* was not affected by the expression of heterologous genes and the fluorescence intensity correlated with the OD₆₀₀ during the exponential growth phase (Pearson correlation coefficient $r > 0.99$, measured from day 0 to day 7, Fig. 3b and c). Notably, the fluorescence intensity continued to rise for 3 days after the culture had reached stationary phase (Fig. 3e). This suggests that the maturation of the NIR FP and the incorporation of BV may be a slow process and indicates that such reporter systems are especially well suited for use with *M. tuberculosis*, which is a slow growing species with a generation time of approximately 20 h. Of note, the highest fluorescence intensity reached with NIR_G13 was about 2-fold higher than that measured with NIR_smyc. *M. tuberculosis* NIR_G13 was thus selected for *ex vivo* infections and the viability of THP-1 infected cells indicated that the virulence of *M. tuberculosis* NIR_G13 was slightly attenuated compared to the WT parental strain, while still being >5-fold more virulent than the fully attenuated $\Delta\Delta RD1$ strain (Fig. 3d). We also tested whether the NIR fluorescence of the NIR_G13 strain could be used as an indication of cell viability *in vitro* in the presence of a bacteriostatic (chloramphenicol, 8 $\mu\text{g}/\text{mL}$) or bactericidal (moxifloxacin, 15 $\mu\text{g}/\text{mL}$) antibiotic.¹⁸ As expected, the optical density rapidly stabilized or started to decrease when chloramphenicol and moxifloxacin were added, respectively. In contrast, growth of untreated cultures was normal (Fig. 3f). The same trends were seen when fluorescence was measured at the same time points (Fig. 3g). Taken together, these results indicate that the fluorescence of the NIR_G13 reporter is a precise indicator of bacterial viability and can serve as a read-out to evaluate the cidal activity of antimicrobials. Encouraged by these observations we investigated the potential of our reporter system for *in vivo* imaging of tuberculosis in mouse models.

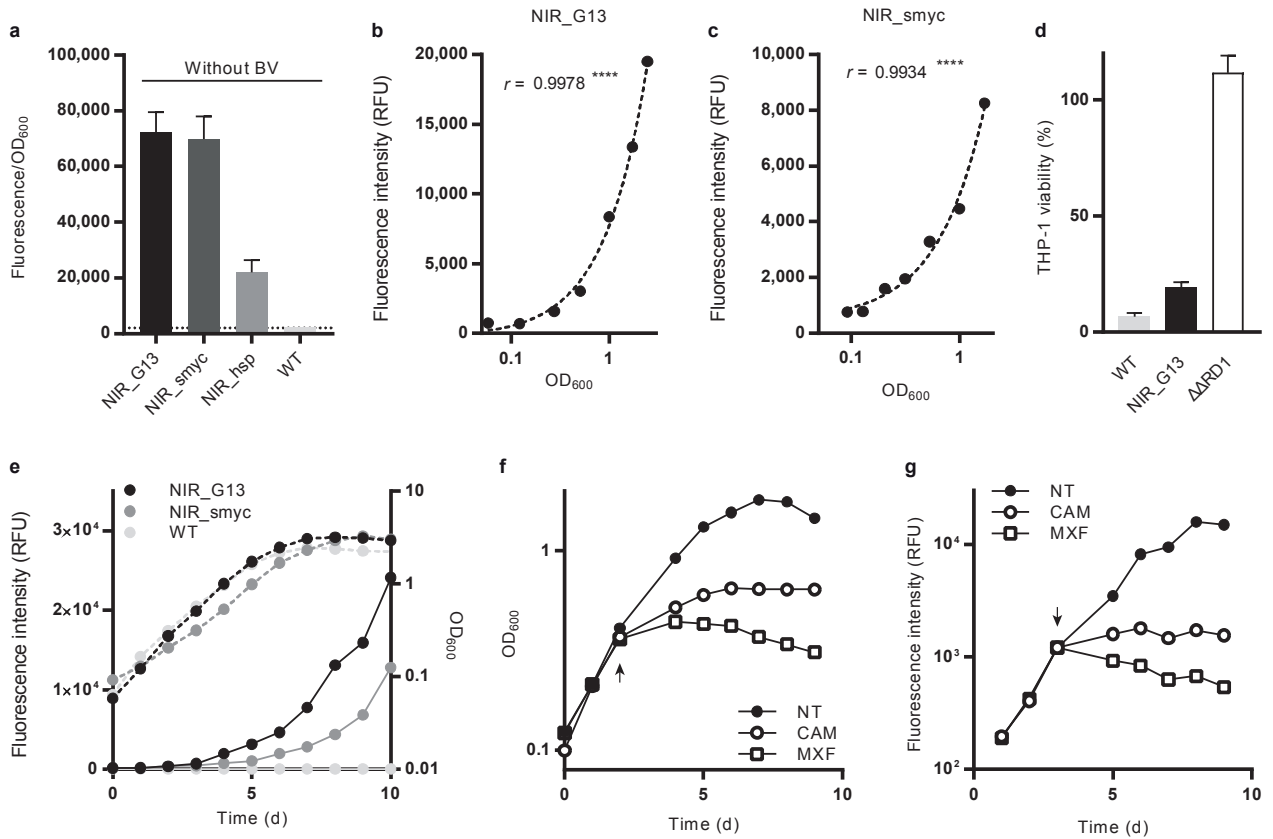


Fig. 3. Characterization of NIR fluorescent reporters in *M. tuberculosis*. **a**, Higher fluorescence intensities can be achieved when *iRFP* and *hol* are expressed from the G13 or *P_{smyc}* promoters. The dotted line indicates background fluorescence of WT bacteria in the same measurement conditions. **b**, **c** The NIR fluorescence measured over 1 week of growth in liquid culture correlates with the OD₆₀₀ for *M. tuberculosis* NIR_G13 (**b**) and NIR_smyc (**c**) strains. r is the Pearson correlation coefficient. **** $P < 0.0001$. The dashed lines are linear regressions. **d**, Viability of THP-1 cells upon infection with *M. tuberculosis* NIR_G13, the parental (WT) strain and the attenuated ΔΔRD1 strain. **e**, Comparison of the growth curves (broken lines) and evolution of the fluorescence intensity (solid lines) in liquid cultures for NIR_G13, NIR_smyc and the parental (WT) strain. **f**, Measurements of the cell density in *M. tuberculosis* NIR_G13 liquid cultures exposed to chloramphenicol (CAM), moxifloxacin (MXF), or untreated (NT). **g**, Measurements of NIR fluorescence in *M. tuberculosis* NIR_G13 liquid cultures exposed to the antibiotics indicated. Addition of antibiotics is indicated by an arrow.

NIR *M. tuberculosis* can be visualized *in vivo* in the lungs of infected mice

NIR FPs are appropriate for *in vivo* imaging in rodents since their emission wavelengths are found in the optical window of the highest tissue transparency.¹¹ To test if *M. tuberculosis* NIR_G13 could be visualized *in vivo*, SCID Hairless Outbred (SHO) mice were infected by aerosol exposure with the reporter strain and fluorescence was monitored by imaging anaesthetized animals with the Photon Imager. A specific fluorescent signal could be detected in the thoracic area 45 days after the infection (Fig. 4a), and its strength increased further up to 58 dpi when the animals were sacrificed. The fluorescence in the abdomen is a non-specific signal from the food in the digestive track, as this is slightly autofluorescent in the NIR wavelengths. Quantification of the fluorescence in the thorax revealed a significant increase in signal (Fig. 4b) that can be precisely monitored over time *in vivo* and correlates with the CFUs enumerated 4 weeks later (Fig. 4c). The pNIR_G13 construct, which carries a kanamycin resistance cassette, was stably maintained during infection as plating of lung homogenates with or without kanamycin revealed no significant difference in the number of CFUs (Supplementary Fig. 2). *Post mortem* quantification of the fluorescence on excised lungs confirmed the correlation between fluorescence intensity and the bacterial load (Fig. 4d). Measurements made 30, 45 and 58 dpi are time endpoints on independent groups of mice. Measurements at 51 and 58 dpi were made on the same group of animals, demonstrating the feasibility of longitudinal imaging. Encouraged by these findings, we decided to use this model to assess antimicrobial activity.

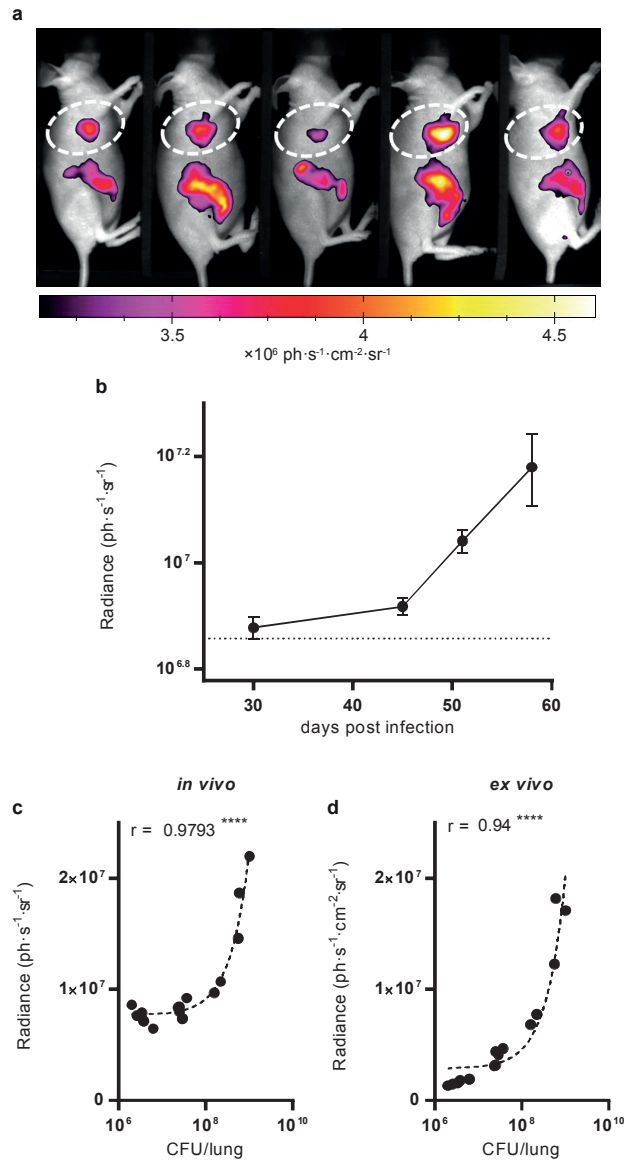


Fig. 4. Visualization and quantification of NIR fluorescence in living infected animals.

a, One group of mice 45 dpi analysed with NIR fluorescence. The picture is a black and white photograph and the NIR fluorescent signal is overlaid in false colour. The quantified zone in the thorax is delimited by dashes and reported in **b** at 45 dpi. **b**, Quantification of the fluorescence intensity in the thorax (indicated as photons per second per steradian) of different groups of mice at the time points indicated. Data show averages and s.e.m. The dotted line indicates the average background fluorescence level measured in uninfected mice. For all time points, $n = 5$ mice per group. **c**, **d** The number of CFU recovered from the lungs of mice at 30, 45 and 58 dpi correlates with the fluorescence measured and quantified *in vivo* (**c**) and *ex vivo* on excised lungs (**d**). r is the Pearson correlation coefficient. **** $P < 0.0001$. The dashed lines are linear regressions.

Fluorescence quantification for drug efficacy testing *in vivo* and *ex vivo*

In order to evaluate the efficacy of treatment, serial dilutions of lung homogenates are commonly plated for CFU enumeration and comparison with an untreated control group. Here, we took advantage of our fluorescent reporter to assess treatment efficacy from fluorescence measurements made *in vivo* and on excised lungs *post mortem*. The animals were infected by aerosol exposure and treated with the following antibiotics: isoniazid (INH), MCZ, and bedaquiline (BDQ) or with a combination of MCZ and BDQ (M+B) for 4 weeks. A significant drop in fluorescence was measured in live animals receiving treatment (Fig. 5a). Excised lungs from treated mice displayed considerably lower fluorescence than the untreated control animals. Lower fluorescence intensity was measured with the group receiving BDQ and M+B as compared to the groups of mice receiving INH or MCZ alone (Fig. 5b). This observation was confirmed by enumerating the CFUs in all cases (Fig. 5c) thus indicating that *post mortem* fluorescence imaging can serve as an indicator of the level of efficacy of a given treatment. Overall, these results suggest that with our NIR *M. tuberculosis* reporter, it is possible to predict *in vivo*, i.e. before sacrificing the animal, if an antibiotic is effectively reducing the bacterial burden in a mouse model of chronic TB infection. *Post mortem* fluorescence data on excised lungs permits to differentially assess the efficacy of the treatments and the CFU numbers enumerated 4-5 weeks later corroborate these measurements (Fig. 5).

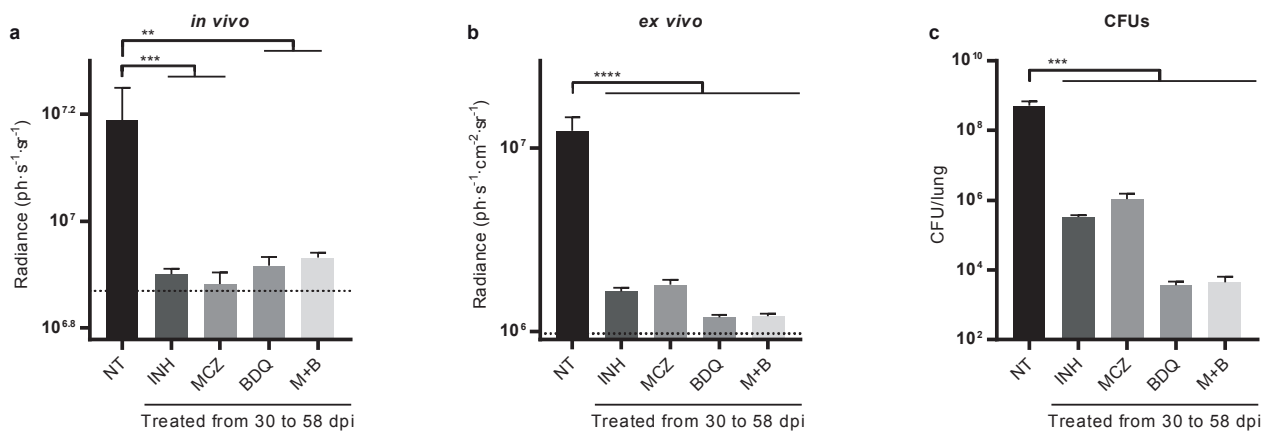


Fig. 5. Fluorescence measurements and CFU enumeration to assess antibiotic efficacy. **a,** Fluorescence was measured *in vivo* and quantified in the thorax of mice (**a**) or *post mortem* on excised lungs (**b**). For the latter, the fluorescence intensity measurement is adjusted for the area of the lung on which the quantification was done and expressed as photons per second per square centimeter per steradian. **c,** Serial 10-fold dilutions of lung homogenates were plated and CFUs were enumerated after 4-5 weeks of growth at 37°C. The dotted line indicates the average background fluorescence measured in uninfected mice (**a**) and lungs (**b**). Bars indicate the average and s.e.m. For each group $n = 5$ mice. NT – non-treated, INH – isoniazid, MCZ – macozinone, BDQ – bedaquiline, M+B – combination of macozinone and bedaquiline. ** $P < 0.01$, *** $P < 0.001$, **** $P < 0.0001$.

DISCUSSION

Here we report for the first time the cloning and expression in mycobacteria of genes encoding NIR FPs derived from bacterial phytochromes. Both *iRFP* and *mIFP*, codon-optimized for usage in *M. tuberculosis*, can be expressed in *M. smegmatis*, *M. marinum* and *M. tuberculosis* and the reporter strains emit NIR fluorescence when BV, the cofactor required for iRFP to fluoresce, is added to the growth medium. The BV requirement can be bypassed by co-expression of *iRFP* with the gene coding for the heme oxygenase 1 (*ho1*) that converts endogenous heme into BV, which is readily incorporated by iRFP. In *M. tuberculosis*, expression of *iRFP* and *ho1* from the G13 promoter leads to the highest fluorescence intensity measured *in vitro*. Moreover, the fluorescence intensity correlated with the number of bacteria in growing liquid culture and could be used to monitor the response to bacteriostatic or bactericidal antibiotics.

Fluorescence imaging *in vivo* requires red-shifted probes, especially for deep imaging, because absorption, scattering and autofluorescence of the tissues is greatly reduced at wavelengths above 650 nm. An *M. tuberculosis* fluorescent reporter producing the Turbo635 protein, which has a maximum of emission at 635 nm, has been reported¹⁸ to permit the visualization of *M. tuberculosis* in the lungs of CB-17 SCID mice and for quantification of the bacterial loads on excised lungs. However, the evaluation of antibiotic efficacy in that study¹⁸ was only performed with *ex vivo* fluorescence measurements and during acute progressive infection following intranasal instillation of bacteria. In contrast, and for the first time, our investigation allowed drug efficacy to be evaluated in living mice with NIR reporters. The low dose aerosol exposure also reproduces the natural route of infection, permitting homogenous infection of several groups of mice simultaneously, as well as allowing time for the infection to evolve before starting treatment. However, NIR *M. tuberculosis* could not be detected *in vivo* in infected immunocompetent furless SKH1 mice (data not shown). Fluorescence imaging of tuberculosis seems to be restricted, therefore, to immunodeficient animals, as suggested elsewhere, since the lower bacterial loads reached in immunocompetent mice can be much more difficult to detect *in vivo*.¹⁸ It may be possible to overcome this limitation using brighter lasers in fluorescence tomography, image enhancement technology, or utilizing mouse lines known to be more susceptible to TB infection, such as C3HeB/FeJ (the “Kramnik mouse model”).²⁸

The zebrafish infection model is finding wider application for assessing the activity of anti-mycobacterial drugs and is an inexpensive and much more rapid alternative to the mouse. In this case, *M. marinum*, a natural pathogen for fish, is used to infect *Danio rerio* embryos via caudal vein microinjection. The transparency of the larvae facilitates visualization of fluorescent bacteria

after infection or upon treatment and this has been done successfully with fluorescent reporters of several colours.²⁹ We show here that our NIR *M. marinum* strain can be visualized in zebrafish embryos, thus adding a new colour to the existing palette of fluorescent *M. marinum* reporters. Furthermore, quantification of NIR fluorescence in infected embryos enabled us to assess the efficacy of MCZ-treatment in this model, consistent with earlier CFU findings²⁷, highlighting the versatility of our approach for several *in vivo* models of tuberculosis infection, and the ensuing applications in drug discovery and development.

The development of NIR FPs has led to several new tools, applicable to small animal imaging and extending the range of available FPs for diverse *in vitro* assays.¹¹ However, their use in deeper and more precise imaging still requires improvement due to their relatively weak brightness.^{30,31} While the Photon Imager Optima permits epi-fluorescence imaging over a wide range of wavelengths, the sensitivity of the detection of bacterial infections could be further improved with trans-illumination or tomographic methods, as well as with the development of more efficient charge-coupled device (CCD) detection systems. Alternatively, intravital fluorescence excitation could partially solve the problem of light absorption and scattering by tissue, by providing a source of light deep in the lungs with an optical fibre-containing microendoscope.^{32,33} Photoacoustic tomography constitutes a different emerging technology with improved spatial resolution in deep tissues, although this technique has not yet been exploited for imaging mycobacterial infections.^{34,35} Finally, the use of NIR fluorescent reporter strains raises the possibility of correlating biomarkers for the pathogen with those of the host, such as the signals obtained by PET/CT imaging.^{20,21}

Development of a mouse model of tuberculosis infection suitable for *in vivo* biophotonic imaging affords numerous advantages over the current models in terms of time, resources and the number of animals required. For instance, the slow growth rate of *M. tuberculosis* requires at least 4 weeks of incubation before CFUs can be counted. In addition, excision, homogenisation and plating of lung samples are endpoint measurements thus provide no information in real time. Our model with NIR fluorescent reporters of *M. tuberculosis* permits 1) to follow the evolution of the infection in real time, 2) to perform several measurements on the same group of mice, thus reducing the total number of animals required per experiment, 3) to quantify the bacterial burden with fluorescence imaging and 4) to evaluate the efficacy of an antibiotic *in vivo*.

METHODS

Bacterial strains and culture conditions

All mycobacterial strains used in this study were grown in Middlebrook 7H9 medium (Difco) supplemented with 0.2% glycerol, 0.05% Tween-80 and 10% albumin-dextrose-catalase (ADC) or on solid 7H10 agar plates containing 0.5% glycerol and supplemented with 10% oleic acid-albumin-dextrose-catalase (OADC). *M. smegmatis* mc²155 and *M. tuberculosis* H37Rv were cultured at 37°C while *M. marinum* strain M³⁶ was kept at 30°C. THP-1 monocyte cells were grown in RPMI supplemented with 10% fetal bovine serum and 1 mM sodium pyruvate at 37°C with 5% CO₂. Hygromycin (HYG, 50 µg/mL), kanamycin (KAN, 20 µg/mL), chloramphenicol (CAM, 8 µg/mL), moxifloxacin (MXF, 15 µg/mL) and biliverdin HCl (BV, Sigma, 25 µM) were added when appropriate.

Construction of the fluorescent strains

The plasmids used in this work were constructed by PCR amplification of *iRFP*, *mIFP* or *hol* optimized for *M. tuberculosis* codon usage and synthesized by Gencript USA Inc. The *M. marinum* G13 promoter²² was amplified from the plasmid pMV306DIG13+FFlucRT¹⁵ (Addgene plasmid # 49998) along with the Shine Dalgarno sequence and cloned in pMV261³⁷ in place of the *hsp60* promoter (P_{hsp60}). The plasmid pCHARGE3³⁸ with the strong P_{smyc} promoter (*M. smegmatis* *rpsA* promoter with *tetO* operator) was a gift from Tanya Parish (Addgene plasmid # 24658). The codon-optimized genes were subcloned in pCHARGE3 in place of *turbo635* or in the multiple cloning site of the pMV261 backbone for expression under either P_{hsp60} or G13 control. The *hol* gene was cloned directly after *irfp* to generate autofluorescent reporters. pSMT3²⁴ was used as an alternative vector for expression of *iRFP* and *hol* under P_{hsp60} . 200 – 500 ng of DNA were electroporated in freshly made competent mycobacteria as described elsewhere³⁸ and selected on appropriate antibiotics.

Fluorescence measurements

M. smegmatis, *M. marinum* and *M. tuberculosis* WT and fluorescent strains were grown to an OD₆₀₀ of 0.8-1. 100 µL of culture were dispensed in black, clear bottom, polystyrene 96-well plates and fluorescence intensity was read in a M200 Tecan microplate reader (excitation / emission: 679 / 713 nm) and normalized to the respective absorbance value at 600 nm, measured in parallel. Strains growing with BV were previously centrifuged and resuspended in PBS or 7H9 without BV. Fluorescence intensity scans were performed similarly with a Tecan Spark M10 multimode microplate reader.

Infection of zebrafish embryos

Zebrafish embryos were infected as previously described.²⁵ Briefly, 24 h old *Danio rerio* (AB) embryos were manually dechorionated and aligned on a custom-made cavity-inlaid agarose bed covered with E3 medium⁴⁰ (5 mM NaCl, 0.17 mM KCl, 0.33 mM CaCl₂, 0.33 mM MgSO₄) containing 0.4 mg/mL MS-222 (Sigma). An *M. marinum* NIR_G13 suspension (1-2 nL containing ~300 bacteria) was microinjected in the caudal vein of the anesthetized embryos using a heat-pulled glass capillary connected to a pneumatic PicoPump PV820 (World Precision Instruments). The embryos were allowed to recover in fresh E3 and maintained at 28°C. 24 h post infection, embryos were distributed in a 6-well plate (15 larvae per well) with 4 mL E3. Macozinone (25 ng/mL) was added directly in E3 when appropriate.

Imaging of infected zebrafish embryos

At 3 dpi, untreated zebrafish embryos were anesthetized with 0.4 mg/mL MS-222 and embedded in 1.2% low melting agarose in an 8-chambered coverslip (Ibidi). The solidified agarose was covered with a layer of E3 containing 0.4 mg/mL MS-222. Samples were visualized with a Zeiss LSM700 inverted confocal microscope equipped with a 20× Plan-Apochromat objective (NA 0.8) and laser excitation light at 639 nm. Images were processed with the ImageJ software v1.52h (<https://imagej.nih.gov/ij/>). For quantitative fluorescence imaging, single anesthetized zebrafish embryos infected with *M. marinum* NIR_G13 (4 dpi) were dispensed in a black clear-bottom 96-well plate. Twelve fluorescence reads per well were measured with a Tecan M200 plate-reader (top reading, excitation / emission: 679 / 713 nm) and averaged for each well. For fluorescence measurements, $n = 12$ embryos per group.

Enumeration of mycobacteria in infected zebrafish embryos

Lysis and decontamination of embryos was performed as described elsewhere²⁵ with some modifications. Embryos were euthanized with an overdose of MS-222 and single specimens were incubated in 25 μ L of 5% SDS in PBS for 5 min. Larvae were disrupted by pipetting and 25 μ L of BBL MycoPrep (BD) was added. The samples were incubated at room temperature for 10 min with shaking and neutralized by addition of 450 μ L of PBS. Serial 10-fold dilutions were plated on 7H10 medium containing 10 μ g/mL cycloheximide and cultured at 30°C for 8 days before CFU enumeration.

Assessment of virulence in THP-1 cells

The virulence of the NIR_G13 strain was evaluated as previously described⁴¹. THP-1 human monocytic cells (10^5 /well) were seeded in 96-well plates and incubated with 100 nM phorbol-12-myristate-13-acetate (PMA) overnight to stimulate macrophage differentiation. The cells were infected with the different *M. tuberculosis* strains (wild-type, NIR_G13 or $\Delta\Delta$ RD1) at a multiplicity of infection of 5. Plates were incubated for 48 h at 37°C with 5% CO₂. Macrophage viability was measured by adding 10 μ l of PrestoBlue® (ThermoFischer Scientific) and incubating for a further 30 min before the fluorescence intensity (excitation / emission: 560 / 590 nm) was measured using an Infinite M200 Tecan plate reader.

Infection and treatment of animals

All the experiments involving animals were performed under ABSL3 containment and approved by the Swiss Cantonal Veterinary Authority under licence number 3082. 6-7 weeks old female SCID Hairless Outbred (SHO) mice (Charles River) were infected with *M. tuberculosis* strain NIR_G13 by aerosol exposure in a Madison chamber. Isoniazid (INH), bedaquilline (BDQ) and macozinone (MCZ), dissolved in water (INH) or in 20% hydroxypropyl- β -cyclodextrin (pH = 3.0, BDQ and MCZ), were administered at a dose of 25 mg/kg by oral gavage for 4 weeks, 5 days per week, starting 30 dpi. For all experiments, $n = 5$ animals per group. Infection followed by treatment with INH was performed twice and provided similar results in the two independent experiments (data not shown for the first experiment). Treatment with BDQ, MCZ and M+B were performed once.

Enumeration of bacteria in the lungs

At indicated time points and after whole body imaging, mice were euthanized by cervical dislocation while under anaesthesia. Lungs were aseptically removed, imaged and homogenized in 2 mL of PBS containing 0.05% Tween 80. Serial 10-fold dilutions of lung homogenates were spread on 7H10 agar containing 16 μ g/mL nalidixic acid (sodium salt), 4 μ g/mL azlocillin (sodium salt) and 10 μ g/mL cycloheximide (all from Sigma). Alternatively, homogenates were decontaminated by mixing with BBL Mycoprep (50:50 V/V), incubating for 5 min and neutralizing with PBS before plating 10-fold serial dilutions on 7H10 containing 0.4% activated charcoal to prevent carryover effects. All plates were kept at 37°C for 4-5 weeks before CFU enumeration.

***In vivo* and *ex vivo* imaging**

In vivo imaging of live animals and *ex vivo* imaging of lungs was performed with a Photon Imager Optima (Biospace Labs, France), equipped with an intensified CCD camera mounted on a light-tight imaging chamber, a 150 W halogen lamp as source of excitation and various excitation and

emission band pass filters. Acquisitions were performed with Photo Acquisition (version 3.4.5.1169) software and the following settings. An excitation filter (645-670 nm) and an emission filter (705-740 nm) were used to measure iRFP fluorescence. Autofluorescence was measured with a lower wavelength excitation filter (595-620 nm) and subtracted with the M3 Vision image analysis software (version 1.1.2.30843). All acquisitions were performed within 10 s of exposure with f/1.2 and illumination power at 100%. Fluorescence images, in false colour, were superimposed on black and white photographs of the specimen using M3 Vision. For quantification of the fluorescence, a region-of-interest (ROI) tool was used. For whole body images, an ROI was drawn on the thoracic area of the mice. This ROI was kept with the exact same shape and area for the analysis of all the animals and fluorescence intensity is expressed as photons per second per steradian ($\text{ph}\cdot\text{s}^{-1}\cdot\text{sr}^{-1}$). Excised lungs were imaged in a sealed plastic Petri dish and an ROI was drawn with the spline tool around the border of each organ. In this case, fluorescence is normalized according to the surface of the ROI and expressed as photons per second per square centimetre per steradian ($\text{ph}\cdot\text{s}^{-1}\cdot\text{cm}^{-2}\cdot\text{sr}^{-1}$). For imaging of live animals, mice were anaesthetized with 5% isoflurane in an induction chamber and transferred on the heated stage (37°C) of the Photon Imager Optima. Mice were placed on their back and slightly tilted towards their left side in front of a gas manifold to maintain them under isoflurane (reduced to 2%) anaesthesia during image acquisition.

Statistics

Statistical analysis was carried out with GraphPad Prism version 7.02. Fluorescence measurements *in vitro* were performed each time on 3 or 4 independent transformants and presented without statistical analysis. For *in vivo* experiments, each group of mice contained $n = 5$ animals and all of them were included in statistical analyses. Zebrafish experiments contained $n = 12$ embryos for fluorescence measurements and $n = 10$ larvae were homogenized and plated for CFU enumeration. When two groups were compared (CFU enumeration from zebrafish larvae), a Mann-Whitney test was used. When more than two groups were compared, an ordinary one-way ANOVA followed by a Tukey's multiple comparisons test were performed. For all tests, $\alpha = 0.05$ and adjusted P -values (two-tailed) are indicated between compared pairs of means. To evaluate the correlation between fluorescence measurements and CFU counts, a Pearson correlation test was used and linear regression analysis was performed. The Pearson correlation coefficient r is presented with a two-tailed P -value.

ACKNOWLEDGEMENTS

We would like to thank A. Lupien for technical assistance with the animal experiments, N. Dhar for providing the codon-optimized gene *iRFP*, L. Rohde and A. Oates for providing zebrafish eggs and for useful discussions. R.S. was supported by a grant from the Fondation Jacqueline Beytout.

AUTHOR CONTRIBUTIONS

R.S. and S.T.C. designed the experiments and wrote the manuscript. R.S. performed the experiments.

COMPETING INTERESTS STATEMENT

S.T.C. is a named inventor on patents pertaining to MCZ.

DATA AVAILABILITY STATEMENT

The data that support the findings of this study are available from the corresponding author upon reasonable request.

REFERENCES

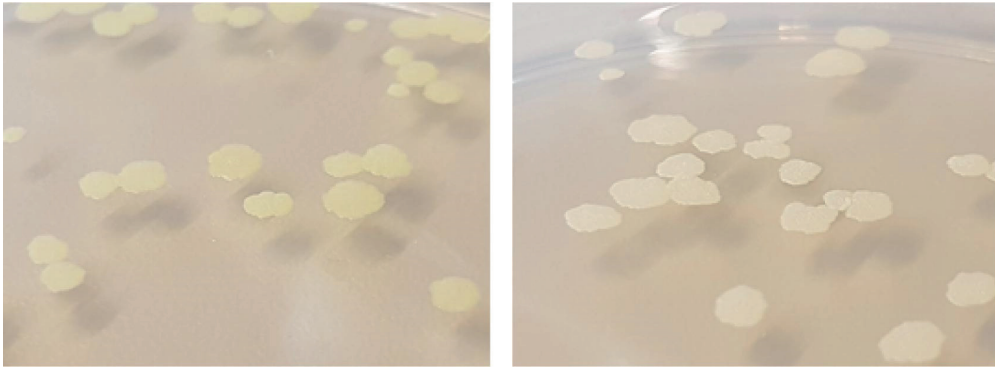
1. WHO. *Global tuberculosis report 2018* (World Health Organisation, Geneva, 2018).
2. Cooper, A. M. Mouse model of tuberculosis. *Cold Spring Harb. Perspect. Med.* **5**, a018556 (2015).
3. Saini, D. *et al.* Ultra-low dose of *Mycobacterium tuberculosis* aerosol creates partial infection in mice. *Tuberculosis* **92**, 160–165 (2012).
4. Andreu, N., Zelmer, A. & Wiles, S. Noninvasive biophotonic imaging for studies of infectious disease. *FEMS Microbiol. Rev.* **35**, 360–394 (2011).
5. Jobsis, F. F. Noninvasive, infrared monitoring of cerebral and myocardial oxygen sufficiency and circulatory parameters. *Science* **198**, 1264–1267 (1977).
6. Hong, G., Antaris, A. L. & Dai, H. Near-infrared fluorophores for biomedical imaging. *Nat. Biomed. Eng.* **1**, 0010 (2017).
7. Deliolanis, N. C. *et al.* Performance of the red-shifted fluorescent proteins in deep-tissue molecular imaging applications. *J. Biomed. Opt.* **13**, 044008 (2008).
8. Shu, X. *et al.* Mammalian expression of infrared fluorescent proteins engineered from a bacterial phytochrome. *Science* **324**, 804–807 (2009).
9. Filonov, G. S. *et al.* Bright and stable near-infrared fluorescent protein for *in vivo* imaging. *Nat. Biotechnol.* **29**, 757–761 (2011).
10. Yu, D. *et al.* A naturally monomeric infrared fluorescent protein for protein labeling *in vivo*. *Nat. Methods* **12**, 763–765 (2015).
11. Chernov, K. G., Redchuk, T. A., Omelina, E. S. & Verkhusha, V. V. Near-infrared fluorescent proteins, biosensors, and optogenetic tools engineered from phytochromes. *Chem. Rev.* **117**, 6423–6446 (2017).
12. Shcherbakova, D. M. & Verkhusha, V. V. Near-infrared fluorescent proteins for multicolor *in vivo* imaging. *Nat. Methods* **10**, 751–754 (2013).
13. Tran, M. T. N. *et al.* *In vivo* image analysis using iRFP transgenic mice. *Exp. Anim.* **63**, 311–319 (2014).

14. Berlec, A., Završnik, J., Butinar, M., Turk, B. & Štrukelj, B. *In vivo* imaging of *Lactococcus lactis*, *Lactobacillus plantarum* and *Escherichia coli* expressing infrared fluorescent protein in mice. *Microb. Cell Factories* **14**, 181 (2015).
15. Andreu, N. *et al.* Rapid *in vivo* assessment of drug efficacy against *Mycobacterium tuberculosis* using an improved firefly luciferase. *J. Antimicrob. Chemother.* **68**, 2118-2127 (2013).
16. Andreu, N. *et al.* Optimisation of bioluminescent reporters for use with mycobacteria. *Plos One* **5**, e10777 (2010).
17. Zhang, T., Li, S.-Y. & Nuermberger, E. L. Autoluminescent *Mycobacterium tuberculosis* for rapid, real-time, non-invasive assessment of drug and vaccine efficacy. *Plos One* **7**, e29774 (2012).
18. Zelmer, A. *et al.* A new *in vivo* model to test anti-tuberculosis drugs using fluorescence imaging. *J. Antimicrob. Chemother.* **67**, 1948–1960 (2012).
19. Yang, H.-J. *et al.* Real-time imaging of *Mycobacterium tuberculosis* using a novel near-infrared fluorescent substrate. *J. Infect. Dis.* **215**, 405–414 (2017).
20. Davis, S. L. *et al.* Noninvasive pulmonary [¹⁸F]-2-fluoro-deoxy-D-glucose positron emission tomography correlates with bactericidal activity of tuberculosis drug treatment. *Antimicrob. Agents Chemother.* **53**, 4879–4884 (2009).
21. Via, L. E. *et al.* Differential virulence and disease progression following *Mycobacterium tuberculosis* complex infection of the common marmoset (*Callithrix jacchus*). *Infect. Immun.* **81**, 2909–2919 (2013).
22. Barker, L. P., Porcella, S. F., Wyatt, R. G. & Small, P. L. The *Mycobacterium marinum* G13 promoter is a strong sigma 70-like promoter that is expressed in *Escherichia coli* and mycobacteria species. *FEMS Microbiol. Lett.* **175**, 79–85 (1999).
23. Guo, X. V. *et al.* Silencing *Mycobacterium smegmatis* by using tetracycline repressors. *J. Bacteriol.* **189**, 4614–4623 (2007).
24. O’Gaora, P. Expression of genes in mycobacteria in *Mycobacteria Protocols* (eds. Parish, T., and Stoker, N.G.) 261–273 (Humana Press, Totowa, NJ, 1998).

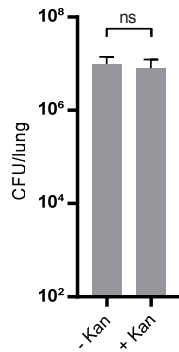
25. Stoop, E. J. M. *et al.* Zebrafish embryo screen for mycobacterial genes involved in the initiation of granuloma formation reveals a newly identified ESX-1 component. *Dis. Model. Mech.* **4**, 526–536 (2011).
26. Takaki, K., Davis, J. M., Winglee, K. & Ramakrishnan, L. Evaluation of the pathogenesis and treatment of *Mycobacterium marinum* infection in zebrafish. *Nat. Protoc.* **8**, 1114–1124 (2013).
27. Makarov, V. *et al.* Towards a new combination therapy for tuberculosis with next generation benzothiazinones. *EMBO Mol. Med.* **6**, 372–383 (2014).
28. Driver, E. R. *et al.* Evaluation of a mouse model of necrotic granuloma formation using C3HeB/FeJ mice for testing of drugs against *Mycobacterium tuberculosis*. *Antimicrob. Agents Chemother.* **56**, 3181–3195 (2012).
29. Takaki, K., Cosma, C. L., Troll, M. A. & Ramakrishnan, L. An *in vivo* platform for rapid high-throughput antitubercular drug discovery. *Cell Rep.* **2**, 175–184 (2012).
30. Baloban, M. *et al.* Designing brighter near-infrared fluorescent proteins: insights from structural and biochemical studies. *Chem. Sci.* **8**, 4546–4557 (2017).
31. Shemetov, A. A., Oliinyk, O. S. & Verkhusha, V. V. How to increase brightness of near-infrared fluorescent proteins in mammalian cells. *Cell Chem. Biol.* **24**, 758–766 (2017).
32. Nooshabadi, F. *et al.* Intravital fluorescence excitation in whole-animal optical imaging. *Plos One* **11**, e0149932 (2016).
33. Nooshabadi, F. *et al.* Intravital excitation increases detection sensitivity for pulmonary tuberculosis by whole-body imaging with β -lactamase reporter enzyme fluorescence. *J. Biophotonics* **10**, 821–829 (2017).
34. Filonov, G. S. *et al.* Deep-tissue photoacoustic tomography of a genetically encoded near-infrared fluorescent probe. *Angew. Chem. Int. Ed Engl.* **51**, 1448–1451 (2012).
35. Krumholz, A., Shcherbakova, D. M., Xia, J., Wang, L. V. & Verkhusha, V. V. Multicontrast photoacoustic *in vivo* imaging using near-infrared fluorescent proteins. *Sci. Rep.* **4**, 3939 (2014).

36. Ramakrishnan, L. & Falkow, S. *Mycobacterium marinum* persists in cultured mammalian cells in a temperature-restricted fashion. *Infect. Immun.* **62**, 3222–3229 (1994).
37. Stover, C. K. *et al.* New use of BCG for recombinant vaccines. *Nature* **351**, 456–460 (1991).
38. Carroll, P. *et al.* Sensitive detection of gene expression in mycobacteria under replicating and non-replicating conditions using optimized far-red reporters. *Plos One* **5**, e9823 (2010).
39. Goude, R. & Parish, T. Electroporation of mycobacteria in *Mycobacteria Protocols: Second Edition* (Parish, T., and Brown, A.) 203–215 (Humana Press, Totowa, NJ, 2009).
40. Brand, M. & Granato, M. Keeping and raising zebrafish in *Zebrafish: A Practical Approach* (eds. Nusslein-Volhard, C. and Dahm, R.) 7–37 (Oxford Univ. Press, Oxford, 2002).
41. Foo, C. S. *et al.* Arylvinylpiperazine amides, a new class of potent inhibitors targeting QcrB of *Mycobacterium tuberculosis*. *mBio* **9**, e01276-18 (2018).

SUPPLEMENTARY DATA



Supplementary Fig. 1. A pale green colour is visible on NIR_smyc *M. smegmatis* colonies (left) compared to wild type bacteria (right).



Supplementary Fig. 2. Similar numbers of CFUs, recovered from the lungs of the group sacrificed at 30 dpi, were enumerated when the sample was plated with and without kanamycin (the selective marker of pNIR_G13). ns = non-significant

Strain name	Plasmid name	Plasmid backbone	Gene expressed	Promoter
mIFP_G13	pmIFP_G13	pMV261-G13	<i>mIFP</i>	G13
mIFP_smyc	pmIFP_smyc	pCHARGE3	<i>mIFP</i>	P _{smyc}
mIFP_hsp	pmIFP_hsp	pMV261	<i>mIFP</i>	P _{hsp60}
iRFP_G13	piRFP_G13	pMV261-G13	<i>iRFP</i>	G13
iRFP_smyc	piRFP_smyc	pCHARGE3	<i>iRFP</i>	P _{smyc}
iRFP_hsp	piRFP_hsp	pMV261	<i>iRFP</i>	P _{hsp60}
NIR_G13	pNIR_G13	pMV261-G13	<i>iRFP</i> and <i>hol</i>	G13
NIR_smyc	pNIR_smyc	pCHARGE3	<i>iRFP</i> and <i>hol</i>	P _{smyc}
NIR_hsp	pNIR_hsp	pSMT3	<i>iRFP</i> and <i>hol</i>	P _{hsp60}

Supplementary Table 1. Plasmids used in this study to construct the reporter strains in mycobacteria.

Chapter 5.

Comparative Analysis of Luciferase-Based Systems for Bioluminescence Imaging of Tuberculosis Infection in Mice

This chapter is a manuscript in preparation (2019).

Contributions: design and execution of the experiments, data generation and analysis, manuscript preparation.

ABSTRACT

Tuberculosis (TB) remains an important global health threat particularly due to the emergence of multidrug-resistant strains of its causative agent, *Mycobacterium tuberculosis*. New, more potent antibiotics are needed to combat resistance and reduce the duration of treatment. Preclinical anti-TB drug development generally involves the assessment of drug efficacy in mouse models but such procedures are long and laborious, given the slow growth rate of *M. tuberculosis*. Here, after comparing the performance of different luciferases and mouse lines, we demonstrate that an autoluminescent *M. tuberculosis* reporter strain can considerably shorten this process by measuring the luminescence in excised lungs from infected immunocompetent mice, rather than by culturing lung homogenates for colony forming unit (CFU) enumeration. The luminescence intensity measured in the organs is proportional to the bacterial load and thus provides a measure of the relative efficacy of a given antibiotic or drug combination. Furthermore, we show that when this reporter is used to infect Severe Combined Immune Deficiency (SCID) Hairless Outbred (SHO) mice, longitudinal *in vivo* measurement of the bacterial load can be performed to evaluate disease progression and the response to isoniazid treatment in real time.

INTRODUCTION

Tuberculosis (TB) is an infectious disease caused by the pathogen *Mycobacterium tuberculosis*. Despite the availability of antibiotic regimens, TB is the leading cause of death worldwide due to a single pathogenic agent.¹ An estimated 10 million people fell ill with TB and 1.6 million people died in 2017 alone. The reasons of this long-lasting pandemic are the absence of an effective vaccine and the emergence of single- and multidrug-resistant (MDR) strains that do not respond to first line drugs (isoniazid, rifampicin, pyrazinamide and ethambutol¹), emphasising the need for new antibiotics to treat MDR-TB and to prevent the development of the disease in the 1.7 billion people latently infected with *M. tuberculosis*.¹

During the TB drug discovery process, the efficacy of new drug candidates is usually evaluated *in vivo* in mouse models of TB infection.²⁻⁶ Exposure of mice to aerosols containing *M. tuberculosis* mimics the natural route of infection. In a model of chronic TB, treatments are administered by oral gavage starting 4 weeks post infection, when the number of bacteria in the lungs of immunocompetent mice plateaus around 10⁶ organisms per lung.⁵ The efficacy of the treatment is generally assessed by plating lung homogenates on solid media, counting the colony forming units (CFUs) recovered and comparison with an untreated group. This method is slow since at least 4 weeks are required for *M. tuberculosis* to produce visible colonies on agar plates and inefficient by

today's standards as data for progression of the infection and treatment efficacy are only obtained retrospectively.

A faster method has been proposed and this involves biophotonic, or *in vivo* imaging of the bacterial infection.⁷ Quantitative imaging of excised lungs infected with a fluorescent *M. tuberculosis* strain has been reported for the evaluation of antibiotic treatment in CB-17 Severe Combined Immune Deficiency (SCID) and SCID Hairless Outbred (SHO) mice.⁸ Similarly, reporter enzyme fluorescence has been used to detect mycobacteria in the lungs of infected animals.⁹⁻¹² Bioluminescent reporters also provide powerful tools to visualize pathogens and quantify bacterial loads *in vivo* and this technique has been successfully applied to *M. tuberculosis* infection.¹³⁻¹⁵

Several luciferase-based systems have been developed as reporters of gene expression or cell viability. Firefly luciferase has been genetically engineered to emit red-shifted light (FFlucRT, maximum of emission at 620 nm) in mycobacteria and proved to be valuable for quantifying the bacterial burden in immunodeficient mice.^{13,14} However, D-luciferin, the substrate for firefly luciferase, has to be administered exogenously, usually via intraperitoneal or intravenous injection, and its biodistribution might pose problems of variability and reproducibility. Alternatively, the *luxCDABE* operon from *Photobacterium luminescens* encodes a luciferase heterodimer (LuxA and LuxB) along with the enzymes that produce its substrate (LuxC, LuxD and LuxE). Hence, cells that express this cluster emit light spontaneously. The utility of the LuxAB luciferase, which is less bright compared to FFlucRT systems, is limited by the wavelength of maximum light emission at around 490 nm and absorbance of this blue-shifted light by mammalian tissues^{16,17}. These features render Lux-based reporters less appropriate for *in vivo* imaging.¹³ The full *luxCDABE* operon has been optimized for expression in high-GC bacteria¹⁸ and successfully used as a reporter of cell viability *in vitro*.^{19,20} *P. luminescens* luciferase-based autoluminescent systems have been used for monitoring *M. tuberculosis* in mice with a luminometer,¹⁵ however, there is no report of whole body imaging of mycobacterial infection to date.

In this study, we investigate the respective advantages and limitations of FFlucRT- and Lux-based *M. tuberculosis* luminescent reporters in different immunocompetent and immunodeficient mouse models. Our aims were 1) to reduce the time of *in vivo* TB experimental infections for drug assessment and 2) to establish a system permitting longitudinal imaging on living animals in order to follow treatment response in real time via luminescence measurements. We demonstrate here that experimental infection of Balb/c and SHO mice with Lux-based *M. tuberculosis* reporters allows these goals to be reached.

RESULTS

Characterization of bioluminescent reporters

To compare the firefly and *P. luminescens* luciferase-based systems in mycobacteria, and to ultimately monitor TB infection *in vivo*, mycobacterial reporters were constructed in the parental strains *M. tuberculosis* H37Rv and *M. smegmatis* mc²155. The Lux reporters were created by transformation of the plasmid pEG200,¹⁹ which replicates in *E. coli* and contains the *luxCDABE* operon codon-optimized for expression in high-CG bacteria,¹⁸ together with the mycobacteriophage L5 *attP* and integrase sequences, required for integration of a single plasmid copy in the bacterial genome.²¹ The *luxCDABE* operon is expressed from the strong pUV15 promoter²² and plasmid pEG200 has been successfully used as a marker of cell viability *in vitro*.^{19,20} Alternatively, plasmid pRS200 contains the *fflucRT*^{13,14} gene, expressed from the strong mycobacterial promoter G13.²³ pRS200 also contains the *attP* site and is integrative but the integrase gene was excised from this plasmid. pRS200 was transformed in mycobacteria to generate the FFlucRT reporters. Neither pEG200 nor pRS200 hampered the growth of the *M. tuberculosis* reporter strains, as the growth curves resemble that of the parental strain (Figure 1a). The luminescence measured for both strains correlates with the optical density (OD₆₀₀) during the exponential growth phase (Figure 1a, d and e). Note that the luminescence of the FFlucRT samples exceeded the detection capacity of the plate reader after 5 d of culture. The intensity of the luminescent signal is dependent on the final luciferin concentration for the FFlucRT reporter. Furthermore, luminescence values weaken over time because of substrate consumption (Figure 1b). The bioluminescence spectra, measured in luminescent *M. smegmatis* reporters, indicated emission maxima around 500 and 620 nm for the Lux and FFlucRT reporters, respectively (Figure 1c), as previously described.^{13,16,18}

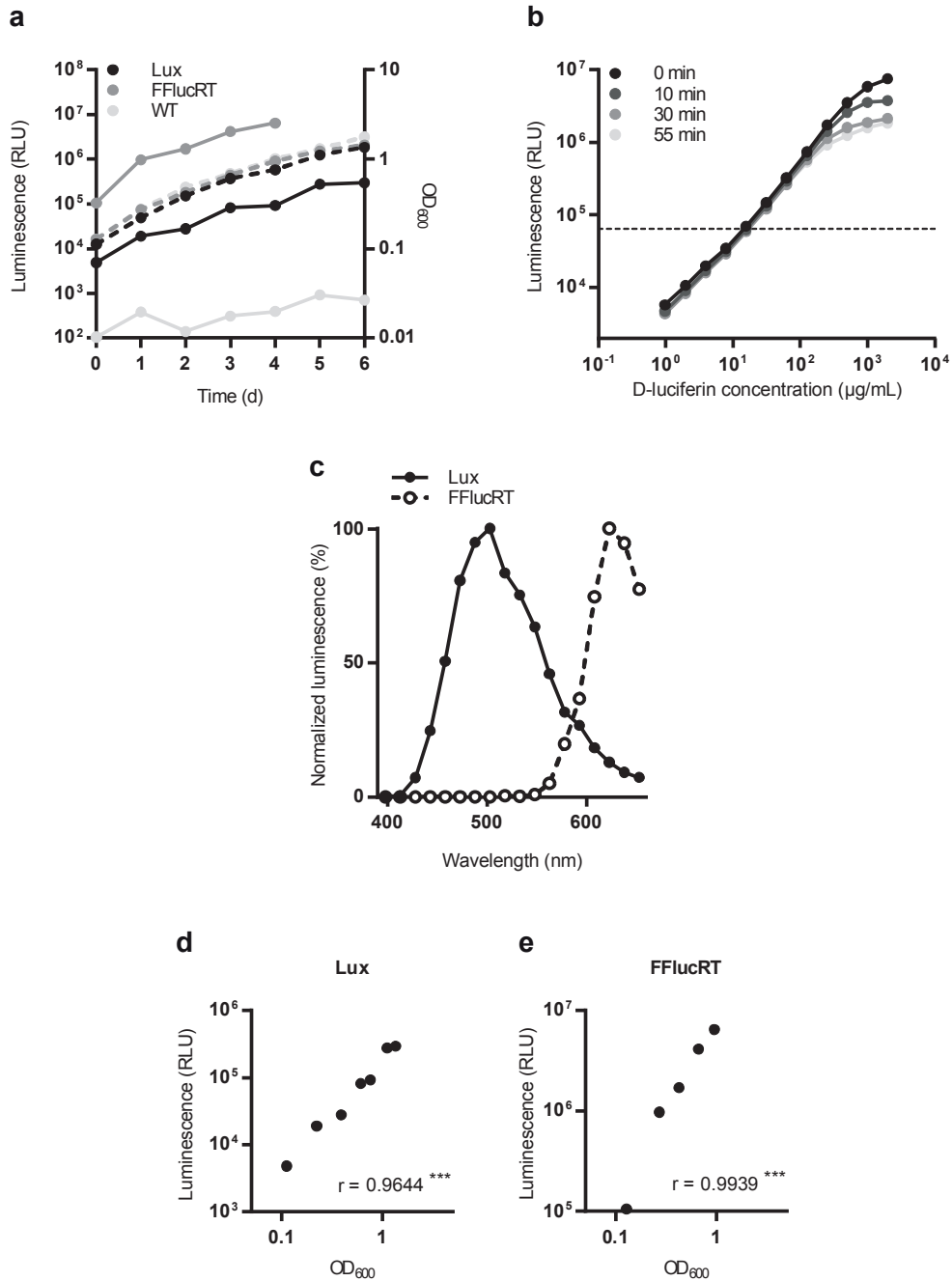


Figure 1. Characterization of the FFlucRT and Lux luminescent mycobacterial strains. (a) Growth curve of *M. tuberculosis* strains FFlucRT, Lux and H37Rv alone (WT) measured by luminescence (solid lines) and optical density at 600 nm (OD_{600} , broken lines). (b) Dependence of the luminescence intensity on D-luciferin concentration and time, for the FFlucRT reporter (bacterial suspension adjusted to $OD_{600} = 1$). The different curves show luminescence measurements of the same samples immediately or 10, 30 or 55 min after addition of the substrate. The dashed line shows the stable luminescence level of the Lux reporter at the same optical density. (c) Normalized luminescence spectra for the *M. smegmatis* FFlucRT and Lux reporters. (d, e) Correlation between the OD_{600} and luminescence measurements for *M. tuberculosis* Lux (panel d) and FFlucRT (panel e) reporters. r is the Pearson correlation coefficient. *** $P < 0.001$.

The FFlucRT system is insufficiently sensitive in immunocompetent animals

An *M. tuberculosis* reporter based on firefly luciferase has previously allowed precise quantification of the bacterial burden *in vivo* and *ex vivo* in CB-17 SCID mice with a good correlation with the CFU counts.¹³ However, these conclusions were only made on immunocompromised animals prompting us to evaluate the performance of our FFlucRT reporter in immunocompetent mice. To maximize the sensitivity of our assay, we selected SKH1 mice, which are non-pigmented and hairless (homozygous for *Hr^{hr}*) yet euthymic and fully immunocompetent. These mice develop *M. tuberculosis* infection and bacterial loads reached 10^4 – 10^5 CFU/lung 4 weeks after low-dose aerosol infection with *M. tuberculosis* H37Rv (data not shown). Mice were infected with the *M. tuberculosis* FFlucRT reporter and imaged at various time points immediately after intra-peritoneal administration of D-luciferin (1 g/kg). As can be seen in Figure 2a, a strong albeit variable luminescent signal was visible in the thorax of the infected mice 4 weeks after infection and the average bacterial load was evaluated at $2.3 \cdot 10^4$ CFU/lung. Two groups of mice were treated with isoniazid (INH) or macozinone (MCZ), respectively, one month post infection, and a third group left untreated for control purposes. Each group was imaged at regular intervals during treatment and the bioluminescent signal in the thoracic area was quantified. The values displayed wide variability both within and between the different groups (Figure 2c), which greatly limited assessment of the effect of treatment *in vivo*. Luminescence measured on excised lungs was nonetheless significantly lower for the treated groups than for the untreated group (Figure 2b), highlighting improved sensitivity *ex vivo* compared to *in vivo*. These results suggest that FFlucRT *M. tuberculosis* reporters can be detected and visualized in SKH1 mice but do not enable quantitative evaluation of the bacterial load *in vivo*, thus precluding longitudinal imaging for the evaluation of treatment efficacy.

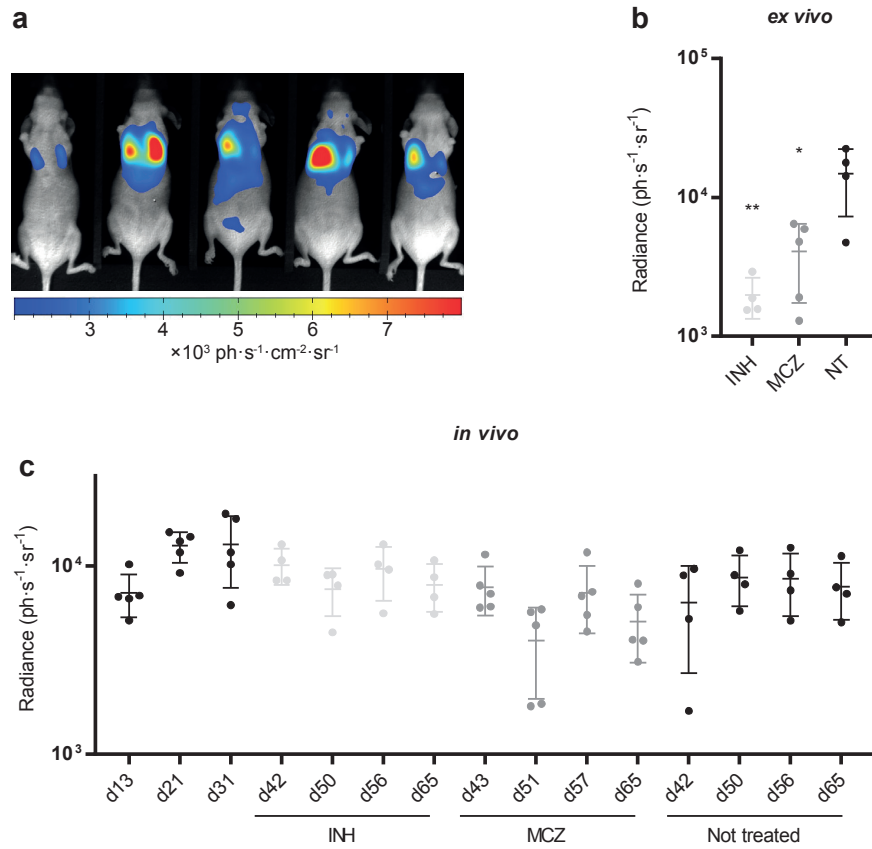


Figure 2. Visualization of FFlucRT *M. tuberculosis* reporters in SKH1 mice. (a) SKH1 mice infected with *M. tuberculosis* FFlucRT imaged 31 d post infection after D-luciferin injection. **(b)** Quantification of the luminescence on excised lungs. INH – isoniazid, MCZ – macozinone, NT – not treated. Each dot corresponds to the lungs of one mouse and bars represent means and standard deviations. * $P < 0.1$, ** $P < 0.01$ on ordinary one-way ANOVA and Tukey’s multiple comparisons test (versus NT). **(c)** Quantification of the luminescent signal in the thoracic area of infected SKH1 mice imaged at the time points indicated (d = day) post infection or upon treatment with INH or MCZ. Treatments were administered from days 30 to 65, when animals were euthanized for *ex vivo* imaging of the lungs. Each dot corresponds to one mouse and bars represent means and standard deviations.

M. tuberculosis* carrying *luxCDABE* permits precise bacterial load quantification in immunocompetent mice *ex vivo

In order to circumvent the need for exogenous D-luciferin administration, the *luxCDABE* operon provides an alternative autoluminescent reporter. While the weak brightness and blue-shifted spectrum of luminescence obtained with bacterial luciferase potentially limit its application for *in vivo* imaging,^{16,17} luminescence remains a faster and time-saving alternative to CFU enumeration and can also be measured *post mortem* on excised lungs. To evaluate the feasibility of this model, Balb/c mice, routinely used to assess the efficacy of anti-TB drugs *in vivo*, were infected with the *M. tuberculosis* Lux reporter strain carrying pEG200. As expected, quantification of the luminescent signal upon *in vivo* whole body imaging did not permit the effect of antibiotic treatment to be measured as all the post-treatment measurements display values very close to the average luminescence signal obtained with uninfected mice. (Figure 3a) However, when imaging was performed on excised lungs, the luminescent signal was significantly lower in lungs from the treated groups compared to the untreated controls. Furthermore, lower luminescence was recorded in groups treated with bedaquiline (BDQ) or a combination of macozinone and bedaquiline (M+B) when compared with groups treated with INH or MCZ alone. (Figure 3b) The CFU values mirror and corroborate the luminescence measurements and display a high correlation with them. (Figure 3c and d) Interestingly, during the course of the infection, the bacterial load reaches a stable plateau at $\sim 10^6$ CFU/lung after one month, while luminescence decreases after two months. This luminescence reduction is probably associated with a reduced metabolic activity of the bacteria entering a latent state. (Supplementary Figure 1) These findings indicate that *post mortem* luminescence measurements on excised lungs from immunocompetent mice infected with an *M. tuberculosis* Lux reporter not only demonstrate that a given treatment reduces the bacterial load, but can also rank the relative activities of single drugs or combinations thereof.

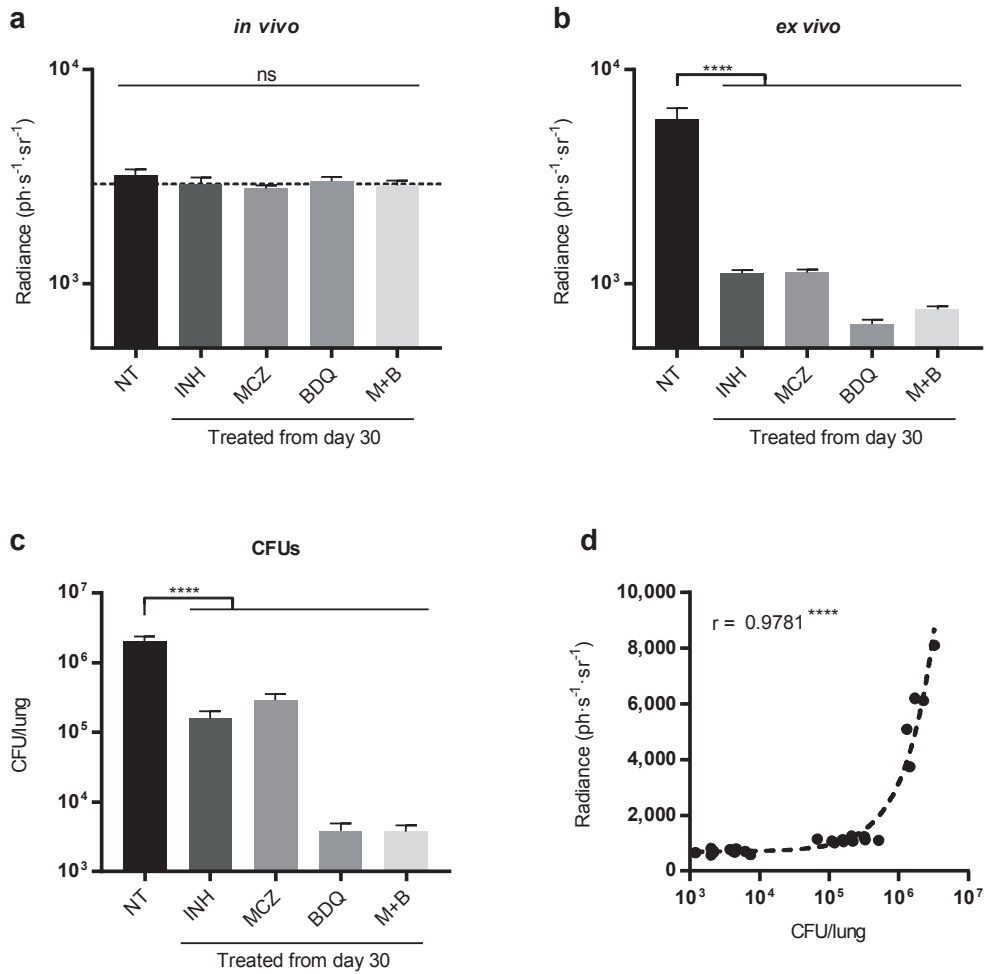


Figure 3. Evaluation of the bacterial load in Balb/c mice by *post mortem* luminescence measurements. (a) Quantification of the luminescence in the thoracic area of infected mice *in vivo*. The dashed line indicates the average luminescence measured in uninfected mice. (b) Quantification of the luminescence on excised lungs from mice receiving the indicated treatment for 4 weeks. (c) CFUs recovered from the same lungs as in panel b. (d) Correlation between luminescence values and CFUs depicted in panels b and c, respectively. Bars represent averages and S.E.M. r is the Pearson correlation coefficient and the dashed line in panel d is a linear regression. **** $P < 0.0001$.

In vivo* quantitative longitudinal imaging with *M. tuberculosis* carrying *luxCDABE

It has been reported that an *M. tuberculosis* strain carrying the *luxCDABE* operon allows the efficacy of several antibiotics to be assessed *in vivo*.¹⁵ The treatments however, were administered for 3 days only, starting one day after infection by tail-vein injection of a bacterial suspension and the luminescence was measured with a benchtop luminometer.

In view of the results presented in the preceding section and in order to increase the sensitivity of detection *in vivo*, we infected SCID Hairless Outbred (SHO) mice, which are homozygous for the *Prkdc^{scid}* and the *Hr^{hr}* mutations. SHO mice can be infected with fluorescent *M. tuberculosis* strains but the mycobacterial growth kinetics appear to be slower than in CB-17 SCID mice,⁸ allowing a larger temporal window for *in vivo* imaging. Mice were exposed to *M. tuberculosis*-containing aerosols to mimic the natural route of infection and 35 d post infection (dpi), a clear bioluminescent signal emanating from the thorax was visible (Figure 4a). Treatment with INH was initiated and the same group of mice was imaged at regular intervals. The luminescent signal was quantified in the thoracic area for each imaging session. As can be seen from Figure 4a and b, the luminescence intensity rapidly dropped after initiation of the treatment and continued to decrease until the end of the experiment. By comparison, a group of untreated mice was imaged successively at 36 and 40 dpi before being sacrificed for CFU enumeration. Untreated mice showed an increase in the bioluminescent signal suggesting that the infection with *M. tuberculosis* remains progressive in SHO mice one month after aerosol exposure (Figure 4b), in contrast to the observations made in immunocompetent animals. The results of *ex vivo* imaging and luminescence quantification are mirrored by the number of CFUs recovered from the lungs (Figure 4c and d, Supplementary Figure 2). In summary, the *luxCDABE* autoluminescent reporter system allows treatment efficacy to be monitored in real time within a single group of mice, and, to our knowledge, this is the first report of serial whole body luminescence measurements of tuberculosis infection with this system in live animals.

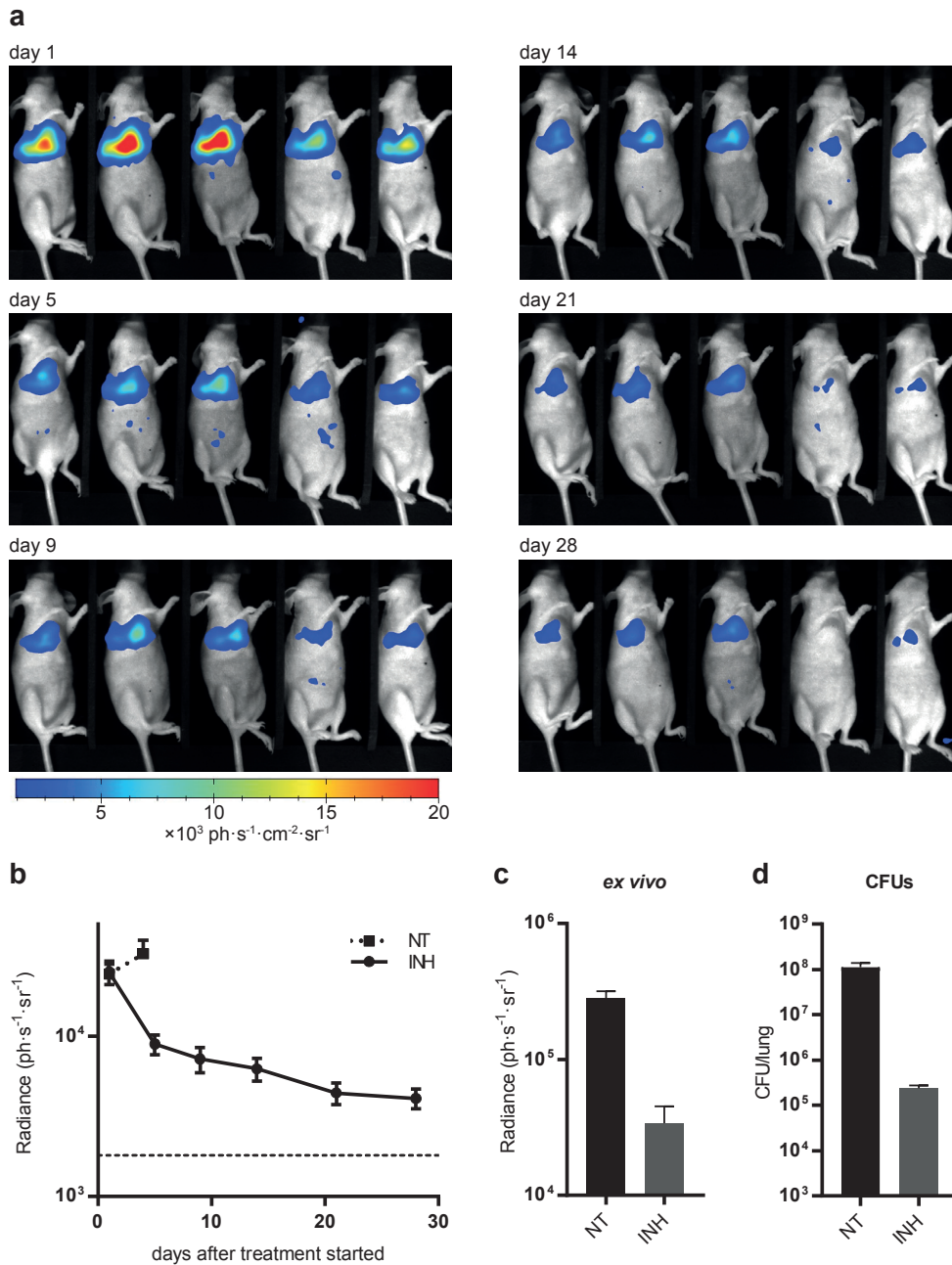


Figure 4. Longitudinal *in vivo* follow up of *M. tuberculosis* load in SHO mice upon treatment with INH. (a) Black/white images of mice with luminescent signal overlaid in false colours. Imaging was performed over time on the exact same mice demonstrating the feasibility of longitudinal monitoring of treatment efficacy using this system. **(b)** Quantification of the luminescence in the thoracic area for the images depicted in panel **a** (solid line) and an untreated group sacrificed at 40 dpi (dotted line). The data show averages and S.E.M. and the dashed line is the average level of bioluminescence measured in 5 non-infected mice. **(c)** Quantification of the luminescence on excised lungs from untreated mice at 40 dpi (NT) or mice treated with INH for 4 weeks (INH). **(d)** CFU enumeration from the organs depicted in panel **c**.

DISCUSSION

Measuring the activity of TB drugs in animal models is a slow and laborious process that has scarcely evolved since the 1930s. In recent years, attempts have been made to monitor biomarkers of the host and pathogen that could increase speed and sensitivity while reducing the number of animals required, ideally by following the same cohort for the duration of the experiment. PET/CT analysis is a good example of the former²⁴ whereas the use of a fluorogenic β -lactamase substrate has been proposed as a means of detecting *M. tuberculosis in vivo*¹². In this investigation we compared the relative efficiency and sensitivity of *M. tuberculosis* reporter strains expressing two different luciferases, one from the firefly (FFlucRT), the other from the bacterium *P. luminescens* (Lux), in two different mouse lines.

By infecting Balb/c mice with a Lux *M. tuberculosis* reporter, we showed that the measurement of the luminescent signal on excised lungs, but not live animals, provides precise evaluation of the bacterial burden and an immediate indication of antibiotic efficacy. Furthermore, the luminescence level also provides accurate information on the relative efficacy of different drugs and drug combinations since the luminescence signal mirrors the bacterial load as determined by CFU enumeration. Depending on the assay design, this approach permits conclusions to be drawn up to 1.5 times faster than with the regular CFU assays (i.e. 2 instead of 3 months).

Luminescence measurement on excised lungs is an endpoint assay. Further improvement lies in following evolution of the infection longitudinally, in the same animals in real time. In immunocompetent Balb/c mice infected with the Lux reporter, no luminescent signal could be quantified in the thorax probably due to their cell-mediated immunity containing and controlling the infection thereby limiting multiplication of bacteria to 10^6 CFU/lungs.⁵ Furthermore, their fur also attenuates light. These combined effects explain why the Balb/c model is not appropriate for *in vivo* imaging with luciferase-based *M. tuberculosis* reporters.

In contrast, SCID Hairless Outbred (SHO) mice allowed more permissive progression of the infection and lack fur. When this mouse line was infected with the *M. tuberculosis* Lux reporter, luminescence could be detected and quantified on the thorax of living mice, as early as 35 dpi (low-dose aerosol exposure). SHO mice appear less susceptible to *M. tuberculosis* infection than CD-17 SCID mice, allowing for more flexibility in imaging and treatment follow up. We demonstrated that with this model it is possible to monitor INH treatment in real time on a single group of mice. Such an experiment easily provides information regarding the rate of the therapeutic effect and also permits the effect of different doses to be evaluated. The two drawbacks with this model are 1) the SCID phenotype and the lack of the adaptive immune response; and 2) outbreeding of the animals,

which might lead to more variability of the results. A congenic variant exists (SCID Hairless Congenic or SHC mice) carrying *Prkdc^{scid}* and the *Hr^{hr}* mutations and was obtained by backcrossing SKH1 onto a CB-17 SCID background. However, the utilization of SHC mice for TB-studies has never been reported.

M. tuberculosis FFlucRT strains have been used for *in vivo* imaging in CB-17 SCID mice.¹³ Our attempts to perform similar measurements in immunocompetent (SKH1) mice were, alas, unfruitful. Although luminescence in the lungs of infected mice could be detected, the high variability among and within the different groups prevented quantitative measurement of the bacterial loads during antibiotic treatment. Exogenous administration of the substrate D-luciferin by injection and differences in its biodistribution might lead to variability and its metabolism by liver enzymes can also be a source of background luminescence. In contrast, when SHO mice were infected with the *M. tuberculosis* Lux reporter strain, the luminescent signal was precisely localized to the thorax.

Our results indicate that infection of mice with an autoluminescent *M. tuberculosis* reporter carrying the *luxCDABE* operon can 1) bypass the need for exogenous substrate injection required for FFlucRT reporters, 2) allow assessment of bacterial loads on excised lungs from Balb/c mice and more rapidly indicate the relative efficacy of different antibiotic treatments than the CFU enumeration method and 3) enable longitudinal whole body imaging of tuberculosis infection and response to antibiotic treatments in real time in SHO mice. These significant improvements to the TB drug development process could help reduce the time to reach clinical trials.

METHODS

Bacterial strains and culture conditions

Mycobacteria were grown in Middlebrook 7H9 medium (Difco) containing 0.2% glycerol, 0.05% Tween-80 and 10% albumin-dextrose-catalase (ADC) or on solid 7H10 agar plates supplemented with 0.5% glycerol and 10% oleic acid-albumin-dextrose-catalase (OADC). Strains *M. smegmatis* mc²155 and *M. tuberculosis* H37Rv were cultured at 37°C. Hygromycin (HYG, 50 µg/mL) was added when appropriate.

Construction of reporter strains

The integrative plasmid pEG200 containing the *luxCDABE* gene cluster optimized for expression in high-GC bacteria organisms was a kind gift from Neeraj Dhar.¹⁹ The plasmid pRS200 was constructed by PCR amplification of the region containing the G13 promoter, Shine Dalgarno and *fflucRT* gene from the plasmid pMV306DIG13+FFlucRT,¹³ kindly provided by Brian Robertson (Addgene plasmid # 49998). The amplicon was then subcloned in a vector variant of pGA44²⁵ (pGA118) containing a hygromycin resistance cassette and a mycobacteriophage L5 *attP* integration site. *M. tuberculosis* reporter strains were obtained after electroporation of 200 – 500 ng of DNA, as described elsewhere,²⁶ and plating on 7H10 containing hygromycin. When needed, pGA80²⁵ was co-transformed to provide the integrase *in trans*.

Luminescence measurements *in vitro*

100 µL of bacterial culture were dispensed in white opaque 96-well plates. In the case of FFlucRT reporters, D-luciferin was added at a final concentration of 150 µg/mL (from a stock solution prepared at 15 mg/mL in PBS and diluted 1:100 V/V), unless otherwise indicated, and luminescence was measured immediately after with a Tecan Infinite M200 (integration time 1 s). Luminescence spectra were acquired with *M. smegmatis* luminescent strains with a Tecan Spark 10M multimode microplate reader. Scans were performed from 398 nm to 653 nm with a step size of 15 nm, a bandwidth of 25 nm and an integration time of 1 s. Graphs were plotted with GraphPad Prism version 7.02.

Infection and treatment of animals

5-6 week old female Balb/c, SKH1 or SCID Hairless Outbred (SHO) mice (Charles River) were infected with *M. tuberculosis* luminescent reporter strains by aerosol exposure in a Madison chamber. The antibiotics isoniazid (INH), dissolved in water, bedaquiline (BDQ) and macozinone (MCZ), dissolved in 20% hydroxypropyl- β -cyclodextrin (pH = 3.0), were administered at 25 mg/kg by oral gavage for 4 weeks, 5 d per week, starting 30 d after the infection. Experiments involving mice were performed under ABSL3 containment and approved by the Swiss Cantonal Veterinary Authority (license number 3082). Experiments involving mice were performed once, with 5 animals per group infected and treated identically.

Enumeration of bacteria in the lungs

At the time points indicated and after *in vivo* imaging, animals were sacrificed by cervical dislocation while anaesthetized. Lungs were aseptically excised, imaged in a black 24-well plate and homogenized in 2 mL of PBS containing 0.05% Tween 80. Serial 10-fold dilutions of the lung homogenates were plated on 7H10 agar containing 16 μ g/mL nalidixic acid (sodium salt), 4 μ g/mL azlocillin (sodium salt) and 10 μ g/mL cycloheximide (all from Sigma). Alternatively, homogenates were decontaminated by mixing with BBL Mycoprep (50:50 V/V), incubating for 5 min and neutralizing with PBS before plating 10-fold serial dilutions on 7H10 containing 0.4% activated charcoal to prevent carryover effects. All plates were cultured at 37°C for 4-5 weeks before CFU enumeration.

***In vivo* and *ex vivo* imaging**

In vivo imaging of live animals and *ex vivo* imaging of lungs was performed with a Photon Imager Optima (Biospace Labs, France), equipped with an intensified CCD camera mounted on a light-tight imaging chamber. Acquisitions were performed with Photo Acquisition (version 3.4.5.1169) software, *f*/1.2, without filters and integrated over 20 min for Balb/c mice and organs and 5 min for SHO mice and lungs. Luminescent signals were superimposed with black and white photographs of the specimen using M3 Vision image analysis software (version 1.1.2.30843). For quantification of the luminescence, a region-of-interest (ROI) tool was used. For whole body images, an elliptic ROI was drawn on the thorax and kept with the exact same shape and area for the analysis of all the animals. Radiance is expressed as photons per second per steradian ($\text{ph}\cdot\text{s}^{-1}\cdot\text{sr}^{-1}$). Organs were distributed in the wells of a 24-well black Ibidi plates for imaging. Quantification of the radiance was performed with a circular ROI adapted to the size of a single well. Alternatively, extracted lungs were imaged in a sealed plastic Petri dish and an ROI was drawn with the spline tool around the border of each organ. In the latter case, radiance was normalized according to the surface of the

ROI and expressed as photons per second per square centimetre per steradian ($\text{ph}\cdot\text{s}^{-1}\cdot\text{cm}^{-2}\cdot\text{sr}^{-1}$). For imaging of live animals, mice were anaesthetized with 5% isoflurane in an induction chamber and transferred on the heated stage (37°C) of the Photon Imager Optima. Mice were placed on their backs or slightly tilted towards their left side in front of a gas manifold to maintain them under isoflurane (reduced to 2%) anaesthesia during image acquisition.

Statistics

Statistical analysis was carried out with GraphPad Prism version 7.02. When two groups were compared, a Mann Whitney test was used. When more than two groups were compared, an ordinary one-way ANOVA followed by a Tukey's multiple comparisons test were performed. To evaluate the correlation between luminescence measurements and CFU counts, a Pearson correlation test was used and linear regression analysis was applied where indicated.

ACKNOWLEDGEMENTS

We would like to thank Andreeane Lupien for technical assistance with the animal experiments and Neeraj Dhar for providing the plasmid pEG200. R.S. was supported by a grant from the Fondation Jacqueline Beytout.

AUTHOR CONTRIBUTIONS

R.S. and S.T.C. designed the experiments and wrote the manuscript. R.S. performed the experiments.

COMPETING INTERESTS STATEMENT

S.T.C. is a named inventor on patents pertaining to MCZ

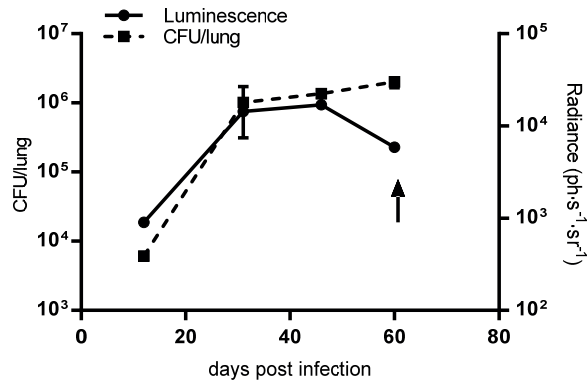
REFERENCES

1. WHO. *Global tuberculosis report 2018* (World Health Organisation, Geneva, 2018).
2. Cooper, A. M. Mouse model of tuberculosis. *Cold Spring Harb. Perspect. Med.* **5**, a018556 (2015).
3. Gupta, U. D. & Katoch, V. M. Animal models of tuberculosis. *Tuberculosis* **85**, 277–293 (2005).
4. Zhan, L., Tang, J., Sun, M. & Qin, C. Animal models for tuberculosis in translational and precision medicine. *Front. Microbiol.* **8**, 717 (2017).
5. Dharmadhikari, A. S. & Nardell, E. A. What animal models teach humans about tuberculosis. *Am. J. Respir. Cell Mol. Biol.* **39**, 503–508 (2008).
6. Young, D. Animal models of tuberculosis. *Eur. J. Immunol.* **39**, 2011–2014 (2009).
7. Andreu, N., Zelmer, A. & Wiles, S. Noninvasive biophotonic imaging for studies of infectious disease. *FEMS Microbiol. Rev.* **35**, 360–394 (2011).
8. Zelmer, A. *et al.* A new *in vivo* model to test anti-tuberculosis drugs using fluorescence imaging. *J. Antimicrob. Chemother.* **67**, 1948–1960 (2012).
9. Kong, Y. *et al.* Imaging tuberculosis with endogenous beta-lactamase reporter enzyme fluorescence in live mice. *Proc. Natl. Acad. Sci. U. S. A.* **107**, 12239–12244 (2010).
10. Kong, Y. & Cirillo, J. D. Reporter enzyme fluorescence (REF) imaging and quantification of tuberculosis in live animals. *Virulence* **1**, 558–562 (2010).
11. Kong, Y. & Cirillo, J. D. Fluorescence imaging of mycobacterial infection in live mice using fluorescent protein-expressing strains. *Methods Mol. Biol.* **1790**, 75–85 (2018).
12. Yang, H.-J. *et al.* Real-time imaging of *Mycobacterium tuberculosis* using a novel near-infrared fluorescent substrate. *J. Infect. Dis.* **215**, 405–414 (2017).
13. Andreu, N. *et al.* Rapid *in vivo* assessment of drug efficacy against *Mycobacterium tuberculosis* using an improved firefly luciferase. *J. Antimicrob. Chemother.* **68**, 2118–2127 (2013).

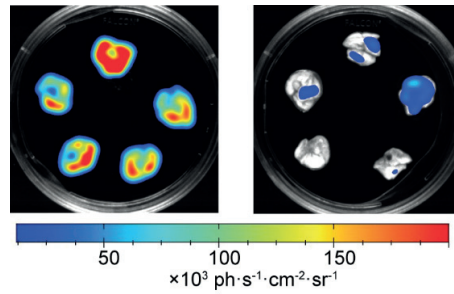
14. Andreu, N. *et al.* Optimisation of bioluminescent reporters for use with mycobacteria. *Plos One* **5**, e10777 (2010).
15. Zhang, T., Li, S.-Y. & Nuermberger, E. L. Autoluminescent *Mycobacterium tuberculosis* for rapid, real-time, non-invasive assessment of drug and vaccine efficacy. *Plos One* **7**, e29774 (2012).
16. Zhao, H. *et al.* Emission spectra of bioluminescent reporters and interaction with mammalian tissue determine the sensitivity of detection *in vivo*. *J. Biomed. Opt.* **10**, 41210 (2005).
17. Rice, B. W., Cable, M. D. & Nelson, M. B. *In vivo* imaging of light-emitting probes. *J. Biomed. Opt.* **6**, 432–440 (2001).
18. Craney, A. *et al.* A synthetic *luxCDABE* gene cluster optimized for expression in high-GC bacteria. *Nucleic Acids Res.* **35**, e46 (2007).
19. Sharma, S. *et al.* Simple and rapid method to determine antimycobacterial potency of compounds by using autoluminescent *Mycobacterium tuberculosis*. *Antimicrob. Agents Chemother.* **58**, 5801–5808 (2014).
20. Vocat, A. *et al.* Bioluminescence for assessing drug potency against nonreplicating *Mycobacterium tuberculosis*. *Antimicrob. Agents Chemother.* **59**, 4012–4019 (2015).
21. Lee, M. H., Pascopella, L., Jacobs, W. R. & Hatfull, G. F. Site-specific integration of mycobacteriophage L5: integration-proficient vectors for *Mycobacterium smegmatis*, *Mycobacterium tuberculosis*, and bacille Calmette-Guérin. *Proc. Natl. Acad. Sci.* **88**, 3111–3115 (1991).
22. Ehrt, S. *et al.* Controlling gene expression in mycobacteria with anhydrotetracycline and Tet repressor. *Nucleic Acids Res.* **33**, e21 (2005).
23. Barker, L. P., Porcella, S. F., Wyatt, R. G. & Small, P. L. The *Mycobacterium marinum* G13 promoter is a strong sigma 70-like promoter that is expressed in *Escherichia coli* and mycobacteria species. *FEMS Microbiol. Lett.* **175**, 79–85 (1999).
24. Davis, S. L. *et al.* Noninvasive pulmonary [¹⁸F]-2-fluoro-deoxy-D-glucose positron emission tomography correlates with bactericidal activity of tuberculosis drug treatment. *Antimicrob. Agents Chemother.* **53**, 4879–4884 (2009).

25. Kolly, G. S. *et al.* Assessing the essentiality of the decaprenyl-phospho-D-arabinofuranose pathway in *Mycobacterium tuberculosis* using conditional mutants. *Mol. Microbiol.* **92**, 194–211 (2014).
26. Parish, T. & Stoker, N. G. Electroporation of mycobacteria. *Methods Mol. Biol.* **101**, 129–144 (1998).

SUPPLEMENTARY DATA



Supplementary Figure 1. Measurement of the luminescence in excised lungs and enumeration of the CFUs at the time points indicated. Balb/c mice were infected with the *M. tuberculosis* Lux reporter. Both the luminescence and number of CFUs reach a plateau at 30 dpi. The number of CFUs remains stable for an additional month at 10⁶ CFU/lung while the luminescence decreases at the last time point (arrow).



Supplementary Figure 2. Luminescence imaging of excised lungs from the untreated group of SHO mice (40 dpi, left panel) or mice treated with INH for 4 weeks (right panel). Images show black and white pictures of the organs overlaid with the luminescence signal in false colours.

PART III

CONSUMPTIVE ZEBRAFISH EMBRYOS

Chapter 6.

The Zebrafish Embryo as a Tool for Anti-TB Drug Discovery and Development

PREFACE

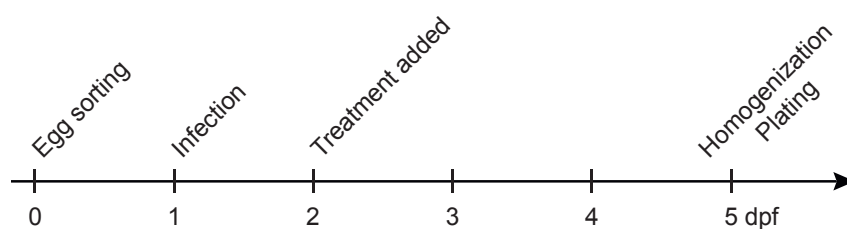
During the last year and a half of my PhD studies, I had the great opportunity to learn innovative techniques and applications with a model to study tuberculosis *in vivo* that is becoming more and more popular: the zebrafish. Beside investigations on host-pathogen interactions, zebrafish embryos infected with mycobacteria can serve in primary assays to evaluate the efficacy of anti-mycobacterial compounds *in vivo*, with major advantages over the mouse model of tuberculosis in terms of time and resources. In line with the general theme of my Thesis regarding the refinement of standard methods to study tuberculosis *in vivo* and to improve drug discovery, I present in this chapter four projects in which I implemented the zebrafish model to complement ongoing efforts on anti-mycobacterial drug development.

INTRODUCTION

Danio rerio, commonly named zebrafish, has become a popular and attractive vertebrate model organism over the past twenty years, with a wide range of applications including in mycobacterial pathogenesis.¹⁻⁴ Their small adult size, ease of breeding, genetic accessibility and larval transparency – just to name a few – are advantageous features favouring their popularity in biomedical research labs, as complements, even surrogates, to rodents. Zebrafish have been used as hosts for studying microbial pathogenesis with several human and fish pathogens.⁵ In order to model mycobacterial infections in zebrafish, *Mycobacterium marinum*, a species closely genetically related to *M. tuberculosis* and a natural pathogen of cold-blooded animals, is usually used for experimental infections in adult fish or in embryos. *M. marinum* infection causes disease in fish, recapitulating several features of *M. tuberculosis* infection in humans.^{6,7} Notably, infection by caudal vein microinjection in 24 h old embryos, which rely solely on their innate immune system, is sufficient to observe the formation of early granulomas following phagocytosis and migration of infected macrophages from the blood stream to deeper tissue.^{2,4}

This model has been extensively applied to study host-pathogen interactions, granuloma dynamics and the roles of mycobacterial virulence factors.⁸ Its application to anti-mycobacterial drug discovery and development began a few years ago.^{9,10} In 2014, a study reported the utilization of the zebrafish-*M. marinum* infection model to validate the *in vivo* anti-mycobacterial efficacy of second generation benzothiazinones (PBTZs), a new class of potent bactericidal anti-TB drugs, showing lower embryonic toxicity compared to the first BTZ generation.¹¹

As a starting point for the development of the assays described in this chapter, the following scheme was applied (Scheme 1). After collection and sorting fertilized eggs, embryos were kept at 28°C in E3 (see Methods section). At 24 h post fertilisation, embryos were infected by microinjection into the caudal vein (~300 bacteria in 1-2 nL) to mimic systemic infection. 24 h post infection, groups of embryos were allocated to defined treatment conditions or left untreated. 4 d post infection (dpi), the embryos were euthanized, homogenized and decontaminated by alkaline treatment with the MycoPrep (BD) reagent (containing 1% NaOH and killing non-mycobacterial species in the fish lysate). Serial 10-fold dilutions were plated for colony forming unit (CFU) enumeration. Finally, zebrafish embryos have been used to model the pathogenesis of *M. abscessus* *in vivo*, as well as for drug discovery against this emerging pathogen.^{12,13}



Scheme 1. General timeline to assess anti-mycobacterial drugs in infected zebrafish embryos. dpf = days post fertilisation.

In line with these demonstrations,⁸⁻¹³ we applied similar approaches to the following contexts, which will be explained and discussed in this chapter:

- 1) *In vivo* activity of pyridomycin in *M. marinum*-infected zebrafish embryos
- 2) Investigating the role of *fadD9* in clofazimine resistance *in vivo*
- 3) Efficacy of inhibitors of mycobacterial virulence factor secretion in infected embryos
- 4) Activity of arylvinylpiperazine amide derivatives against *M. abscessus in vivo*

IN VIVO ACTIVITY OF PYRIDOMYCIN IN *M. MARINUM*-INFECTED EMBRYOS

Background Information

Pyridomycin was initially described in 1935.¹⁴ This molecule (Figure 1), a natural compound produced by the actinomycete *Dactylosporangium fulvum*, exhibited specific antimicrobial activity against several mycobacteria and its mechanism of action has been discovered only recently.^{15,16} These studies demonstrated that pyridomycin is a direct competitive inhibitor of the NADH-binding site of the NADH-dependent enoyl-[Acyl-Carrier-Protein] reductase InhA, which is also the target of isoniazid, a frontline anti-TB prodrug. Inhibition of InhA by pyridomycin or isoniazid leads to the interruption of mycolic acid synthesis, which is one of the most powerful means to kill mycobacteria.¹⁵ However, the emergence of multidrug-resistant *M. tuberculosis* strains, which are resistant to isoniazid and other frontline drugs, compromise current available therapeutic strategies. Notably, pyridomycin kills isoniazid-resistant clinical isolates of *M. tuberculosis*. Furthermore, no cross-resistance has been observed between pyridomycin and isoniazid, making this compound a promising scaffold for the treatment of drug-resistant TB.

Two 2,1'-dihydropyridomycin isomers have been recently synthesized.¹⁷ While the 2*S* isomer presented a much lower activity against *M. tuberculosis*, the 2*R* isomer only showed a fourfold increase in MIC, encouraging the production of other synthetic pyridomycin analogues. Among them, the synthetic compound DM122 (Figure 1) displayed similar activity as pyridomycin *in vitro*. Like pyridomycin, DM122 increases the viability of *M. tuberculosis*-infected THP-1 cells compared to untreated infected controls and the mechanism of action of DM122 is under investigation (Lupien A. *et al.*, manuscript in preparation).

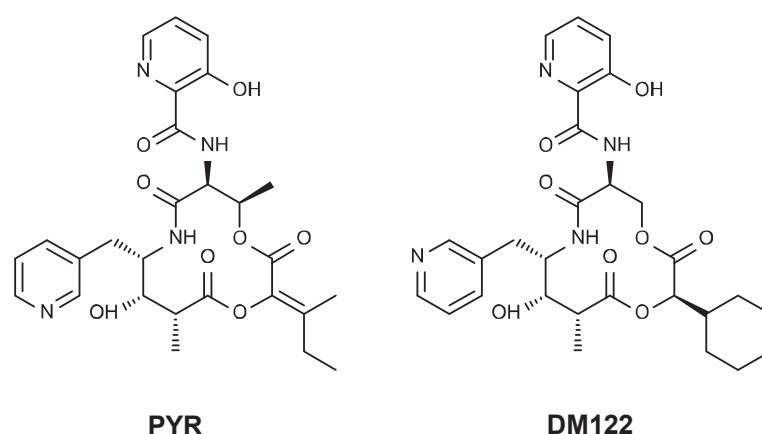


Figure 1. Molecular structure of pyridomycin (PYR) and its synthetic analogue DM122.

To complement *in vitro* and *ex vivo* data, the aim of our study was to test whether pyridomycin and DM122 can reduce mycobacterial loads *in vivo*. Using the zebrafish embryo model of *M. marinum* infection, we showed that exposure of infected larvae to pyridomycin and DM122 diminishes the number of CFU per fish. The zebrafish model is especially useful as the procedure does not require large amounts of drugs, usually difficult to obtain with synthetic experimental compounds such as DM122. This is, to our knowledge, the first demonstration of pyridomycin and DM122 efficacy *in vivo*. In addition, no toxicity was observed for zebrafish embryos exposed to these drugs at the concentrations tested. These results are encouraging for the further development of pyridomycin-based anti-mycobacterial drugs, especially to treat drug-resistant infections.

Pyridomycin and DM122 treatment reduces bacterial loads in *M. marinum*-infected zebrafish embryos

The *in vitro* minimal inhibitory concentration (MIC) of pyridomycin and its most potent analogue DM122 against *M. marinum* were 3.16 and 6.3 $\mu\text{g/mL}$, respectively. To test whether pyridomycin and DM122 have antibacterial activity *in vivo*, zebrafish embryos were infected with *M. marinum* via microinjection in the caudal vein and drugs were added directly to fish water 24 h post infection. Larvae were exposed for 3 d to several concentrations of the drugs before lysis and plating of fish homogenates for CFU enumeration. CFU numbers recovered from infected embryos exposed to 2, 5 or 10 \times the *in vitro* MIC of pyridomycin or DM122, were similar to those counted for untreated embryos, indicating that the drugs are inactive *in vivo* at these concentrations (Figure 2a). At 50 \times MIC, pyridomycin exposure led to a slight yet significant reduction of CFUs when compared to a non-treated group (Figure 2b). DM122 was still ineffective at 50 \times MIC and slightly precipitated. The concentration of DMSO was raised to 2% to aid solubilisation without affecting the bacterial load (Figure 2c). A significant reduction of the CFUs was observed for fish exposed to 75 and 100 \times the MIC of pyridomycin and DM122 (Figure 2d). This therapeutic effect was similarly observed when fish were exposed to isoniazid. To compare the effect of both drugs at the same concentration, infected embryos were exposed to a molar concentration of pyridomycin or DM122 equivalent to 75 \times the *in vitro* MIC of pyridomycin. Both drugs significantly reduced the bacterial load in zebrafish embryos at this concentration (Figure 2e). The slightly attenuated efficacy of DM122 can be attributed to its weak solubility in water. Finally, similar conclusions could be drawn when fluorescence intensity of bacterial reporters was used as a readout instead of CFU enumeration, corroborating our observations (Figure 2f). Notably, exposure to pyridomycin, DM122 or 2% DMSO did not significantly impact embryonic development, as the length of embryos at 3 d of treatment was similar in treated and untreated fish (Figure 2g). Taken together, our observations indicate that both pyridomycin and DM122 reduce mycobacterial loads in

M. marinum-infected zebrafish embryos without affecting embryonic development, indicating a highly specific and effective anti-mycobacterial activity in this model with low side-effects.

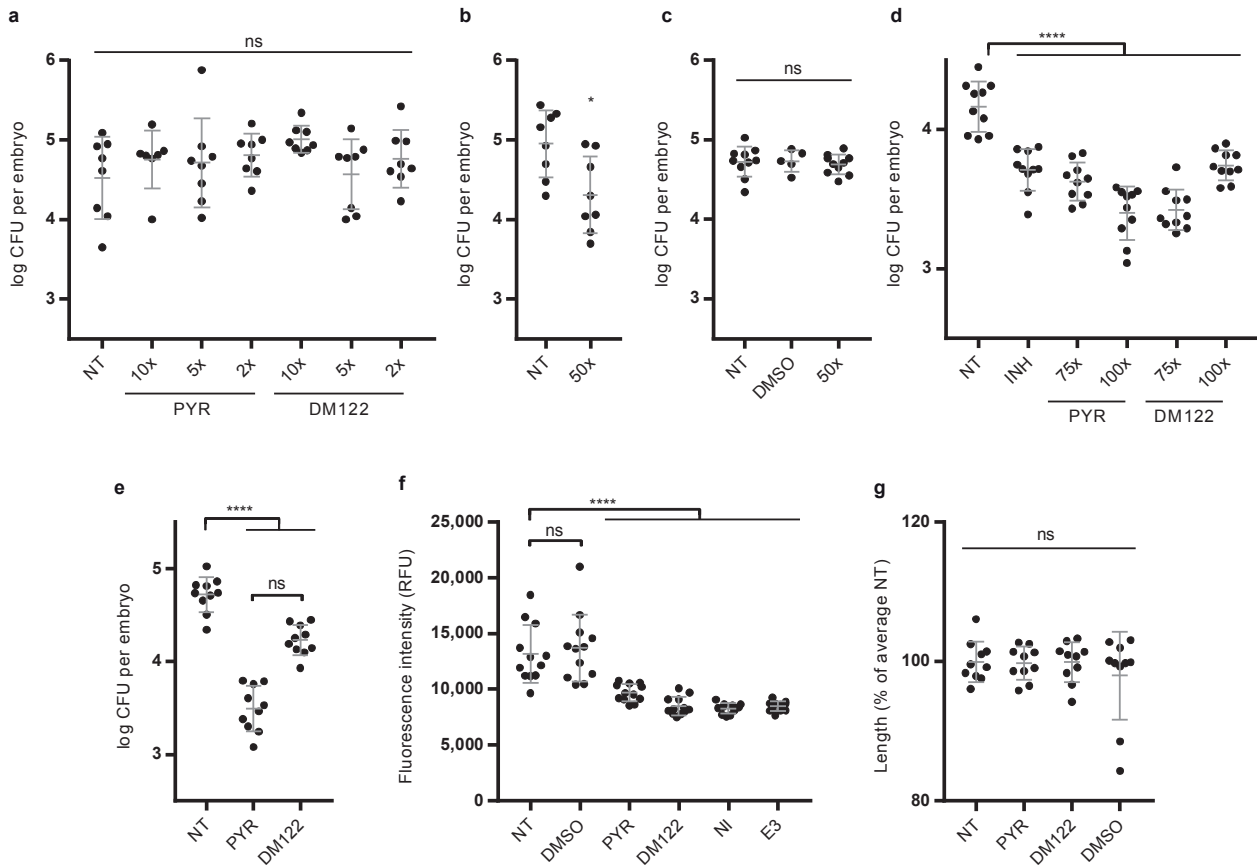


Figure 2. Anti-mycobacterial activity of pyridomycin and DM122 in *M. marinum*-infected zebrafish embryos. **a**, CFUs recovered from zebrafish embryos treated with pyridomycin (PYR) or DM122 at their indicated fold MIC. **b**, Enumeration of CFUs from infected zebrafish embryos treated with PYR at 50× its MIC. **c**, Number of colonies recovered from zebrafish larvae exposed to DM122 at 50× its MIC or 2% DMSO. **d**, CFUs recovered from fish larvae treated with isoniazid (INH, 400 μM), PYR and DM122 at the indicated multiple concentration of their respective MIC. **e**, Recovery of CFUs from zebrafish embryos treated with the same molar concentration of PYR or DM122 (drug concentration = 75× MIC of PYR). **f**, Evaluation of the bacterial load in zebrafish embryos infected with a fluorescent *M. marinum* reporter and exposed to 2% DMSO, PYR and DM122 (at 75× their respective MIC). **g**, The total length of the embryos is not affected by exposition to the compounds PYR, DM122 (at 75× their respective MIC) and 2% DMSO. NT = not treated, NI = not infected, E3 = E3 medium only. ns = not significant, **** $P < 0.0001$ on ordinary one-way ANOVA and Tukey's multiple comparison test. * $P = 0.0194$ on Mann-Whitney test.

INVESTIGATING THE ROLE OF *FADD9* IN CLOFAZIMINE RESISTANCE *IN VIVO***Background Information**

Clofazimine (CFM, Figure 3) is a riminophenazine drug commonly used to treat leprosy. It is part of the multidrug therapy recommended for leprosy treatment by the WHO, along with rifampicin and dapson. ¹⁸ It was recently repurposed for the treatment of multidrug-resistant TB. ¹⁹ Several preclinical studies reported the benefits of CFM-containing regimens to treat TB in mice ^{20,21} and synergism could be observed when CFM was combined with benzothiazinones. ^{22,23} The mode of action of CFM in *M. tuberculosis* and *M. smegmatis* has been investigated by others. ²⁴ The study reported that CFM can act as a prodrug that is reduced by type 2 NADH-quinone oxidoreductase (NDH-2). Its subsequent spontaneous nonenzymatic reoxidation releases reactive oxygen species (ROS). ROS at high concentration can trigger cell death but do not have a specific target, rendering CFM resistance difficult to characterize in this context. It has also been proposed that overexpression of MmpL5 (a multisubstrate efflux pump) can lead to low-level resistance to CFM and cross-resistance to bedaquiline, a new promising anti-TB drug inhibiting *M. tuberculosis* ATP synthase, ^{25,26} by boosting efflux mechanisms. ²⁷

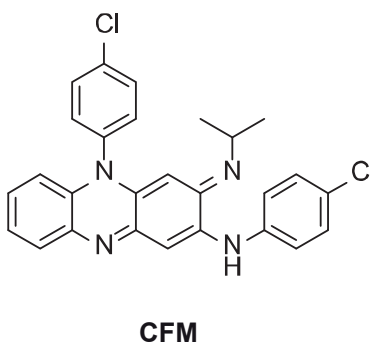


Figure 3. Molecular structure of clofazimine.

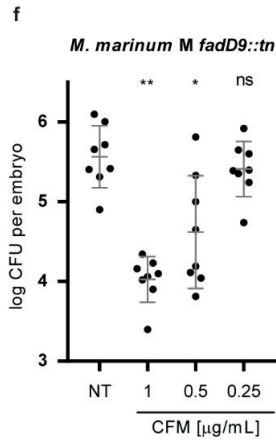
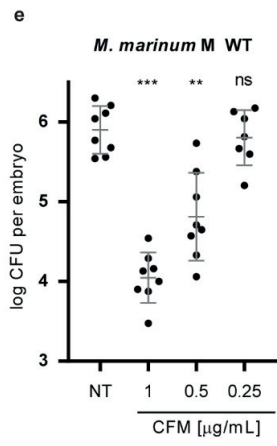
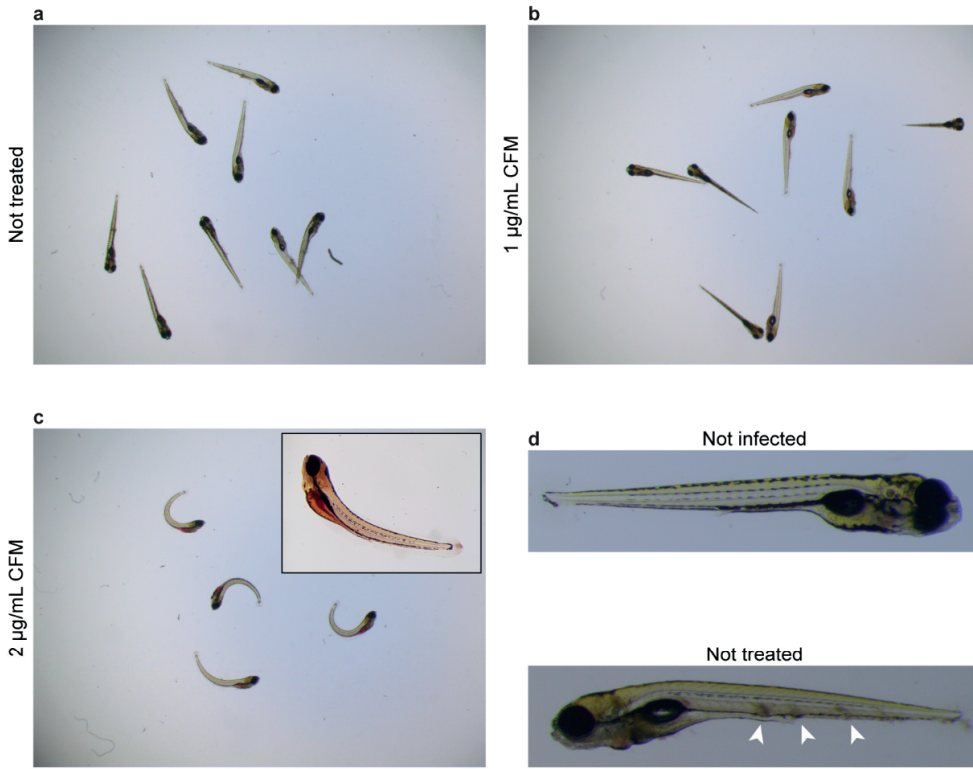
The precise mode of action and resistance mechanisms of CFM in the unculturable, intracellular pathogen, *Mycobacterium leprae*, the causative agent of leprosy, remain poorly understood, however. Comparative genomics on 154 *M. leprae* genomes revealed polymorphisms in the gene *fadD9*, occurring exclusively in multidrug resistant strains. ²⁸ The observed mutations are frameshift mutations, premature stop codons or non-synonymous mutations. Consistent with these observations, *fadD9* which encodes a putative fatty-acid-CoA ligase, is not required for the *in vitro* growth of *M. tuberculosis* ^{29,30} This led us to hypothesize that the polymorphisms in *fadD9*

observed in *M. leprae* may be associated with drug resistance and play a role in the mode of action of CFM. As genetic modification of *M. leprae* is impossible, the role of *fadD9* in CFM resistance is currently being investigated in *M. tuberculosis* and *M. marinum* as surrogate hosts.

Preliminary data with an *M. tuberculosis* strain in which *fadD9* had been deleted showed that the *in vitro* susceptibility to CFM was not significantly altered compared with the wild-type (WT) strain. However, when THP-1 cells were infected with *M. tuberculosis*, the deletion of *fadD9* conferred resistance to CFM and viability of THP-1 cells was reduced, compared to cells infected with WT bacteria and exposed to the same amount of CFM. This led to the hypothesis that when *M. tuberculosis* or *M. leprae* bacteria grow intracellularly, then the activity of FadD9 contributes to their susceptibility to CFM.

In an effort to validate this hypothesis, we worked with an *M. marinum* strain carrying a transposon in *fadD9* (*M. marinum fadD9::tn*), thus abolishing the normal expression of this gene. Previous observations suggested that the CFM resistance phenotype appears only when bacteria grow inside macrophages, so we applied the zebrafish embryo model of mycobacterial infections to explore this hypothesis *in vivo* and upon exposure to CFM.

Figure 4 (page vis-à-vis). Anti-mycobacterial activity of clofazimine in *M. marinum*-infected zebrafish embryos. **a-c**, Photographs of infected zebrafish embryos taken 4 dpi, depicting their global morphology upon exposure to 1 µg/mL CFM (**b**), 2 µg/mL CFM (**c**) or left untreated (**a**). **d**, Close up of the morphology of uninfected fish (top panel) or infected fish (bottom panel) 4 dpi. Arrowheads indicate probable lesions caused by *M. marinum*. **e-f**, CFUs recovered from zebrafish larvae infected with *M. marinum* strain M WT (**e**) or *fadD9::tn* (**f**) and treated with the indicated dose of CFM. ns = not significant, * $P < 0.05$, ** $P < 0.01$ *** $P < 0.001$ on ordinary one-way ANOVA and Tukey's multiple comparison test.



An optimal compromise between drug toxicity and anti-mycobacterial activity of CFM is achieved at a concentration of 1 $\mu\text{g}/\text{mL}$

Before comparing the efficacy of CFM treatment in zebrafish embryos infected with WT or *fadD9::tn M. marinum*, we evaluated whether CFM was toxic to the embryos by exposing them to different concentrations of CFM. Addition of $>1 \mu\text{g}/\text{mL}$ CFM in fish water led to a slight orange coloration of the embryos, mainly visible in the yolk (Figure 4a-c). This is consistent with its known high lipophilicity, often leading to skin coloration in patients treated with this drug.³¹ At a concentration of $>1 \mu\text{g}/\text{mL}$, embryonic malformations were visible as soon as 24 h after drug addition (Figure 4c). Notably, dorsal spinal curvature was visible in most of the embryos treated with $2 \mu\text{g}/\text{mL}$ CFM suggesting that the compound is toxic for the embryos at this concentration. At $>2 \mu\text{g}/\text{mL}$, most of the embryos died before the end of the experiment (3 d of drug exposure in total). No malformations were visible at concentrations $\leq 1 \mu\text{g}/\text{mL}$ and we therefore decided to use final concentrations $\leq 1 \mu\text{g}/\text{mL}$ for our assays, to minimize toxicity. Interestingly, dark areas (probably necrotic regions), absent in non-infected fish, were visible in untreated embryos at 4 dpi (Figure 4d, arrowheads). These regions are likely to be lesions triggered by early granuloma formation as previously reported.²

***fadD9::tn M. marinum* do not display a CFM resistance phenotype upon zebrafish larvae infection**

The *in vitro* MIC of CFM in WT and *fadD9::tn* mutant *M. marinum* was $0.2 \mu\text{g}/\text{mL}$ for both strains, confirming that a disruptive mutation in *fadD9* does not confer resistance to CFM in 7H9 complete medium. To test whether a CFM resistance phenotype can be observed upon infection, 24 h old zebrafish embryos were infected with either WT or *fadD9::tn M. marinum* bacteria by microinjection in the caudal vein. 24 h later, 1, 0.5 or $0.25 \mu\text{g}/\text{mL}$ CFM was added directly in fish water and larvae were exposed to the drug for 3 consecutive days before homogenization and plating for CFU enumeration. As can be seen in Figure 4e, more than 1.5 log-fold reduction in CFUs was achieved on exposure to $1 \mu\text{g}/\text{mL}$ CFM, validating the efficacy of this drug in the zebrafish model at a concentration as low as $5\times$ its *in vitro* MIC. The antimicrobial activity was dose dependent and at $0.25 \mu\text{g}/\text{mL}$, no significant therapeutic effect could be observed (Figure 4e). Unexpectedly, similar dose-dependent antimicrobial activity was observed in embryos infected with the *fadD9::tn* mutant (Figure 4f), suggesting that an inactive FadD9 is not sufficient to confer resistance to CFM upon *M. marinum* infection in the zebrafish embryo model.

EFFICACY OF INHIBITORS OF MYCOBACTERIAL VIRULENCE FACTOR SECRETION

Background Information

Bacterial resistance to antibiotics has become one of the greatest threats to global health in the twenty-first century and new strategies to treat infectious diseases are being explored.³² An innovative proposal is to inhibit the virulence mechanisms of bacterial pathogens. This approach has the added advantage of lowering the risk of resistance developing.³³ Anti-virulence compounds do not directly affect microbial growth and it is therefore postulated that bacteria are much less subject to selective pressure for resistance development.³⁴

M. tuberculosis' most crucial virulence factor is a type VII secretion system named ESX-1, which is missing in the attenuated vaccine strain *Mycobacterium bovis* BCG. Although all the functions of ESX-1 effector proteins are not fully understood, these factors are required for mycobacterial survival in the host and escape from the phagosome of the macrophage into the cytosol. Taking this into account, it is legitimate to propose that ESX-1 inhibition could be a good strategy to control *M. tuberculosis* upon infection.^{34,35}

Two promising inhibitors of mycobacterial virulence, the benzothiophene BTP15 and the benzyloxy benzylidene hydrazine BBH7, have been identified in a cell-based anticytolytic screen.³⁵ BTP15 seemed to be a specific ESX-1 inhibitor, protecting lung fibroblasts from *M. tuberculosis*-induced cell death and reducing intracellular bacterial load in infected THP-1 macrophages without affecting bacterial growth *in vitro*. The proposed mechanism of action of BTP15 is the inhibition of the histidine kinase MprB, which is part of a two-component system that directly regulates ESX-1. Indeed, BTP15 addition to *M. tuberculosis* cultures led to reduced detection of EsxA, an ESX-1-secreted protein, in the culture milieu. Notably, EsxA has been associated with interruption of phagosome maturation, cytosolic escape and host cell lysis.³⁶

It has been reported that BTP15 does not inhibit bacterial growth *in vitro*.³⁵ In order to appreciate its anti-virulence effect, *ex vivo* infections of lung fibroblasts or THP-1 cells are thus necessary. In addition, the zebrafish embryo model of mycobacterial infection seems well suited for this assay, in order to measure the anti-virulence properties of this inhibitor *in vivo*, and this is the subject of this study. It has been demonstrated that macrophages are functional in zebrafish embryos and these immune cells can phagocytose mycobacterial pathogens upon infection.² We hypothesized that treatment of infected zebrafish embryos with inhibitors of mycobacterial virulence factors would promote phagolysosomal fusion and attenuate intracellular bacterial growth. We assessed this hypothesis by counting CFUs recovered from embryos and our observations are described below.

Optimization of an anti-virulence drug assay in the zebrafish embryo model of *M. marinum* infection

For this assay, 24 h old zebrafish embryos were infected with *M. marinum* via caudal vein microinjection and subsequently exposed to the candidate compounds at different concentrations. The half maximal inhibitory concentration (IC₅₀) of BTP15 in lung fibroblasts infected with *M. tuberculosis* was 1.2 μM ³⁵ (equivalent to 0.43 $\mu\text{g/mL}$) and embryos were exposed to concentrations ranging from 1 to 100 $\mu\text{g/mL}$. We observed high toxicity towards zebrafish embryos in this range of concentrations: all the individuals of several groups had died the day after the drug was added, as indicated by absence of heart beat, shrinking and darkening of the larvae. The maximal tolerated dose of BTP15 for this assay was only 1 $\mu\text{g/mL}$ (Table 1). However at this concentration, no difference could be observed in the number of CFUs when treated and untreated groups were compared. (Figure 5a).

Based on preliminary *in vitro* and *ex vivo* activity assays of several BTP derivatives with *M. tuberculosis*, (Lupien, A., *et al*, manuscript in preparation), a selection of 5 benzothiophene (BTP) analogues (Table 1) was made for application in the zebrafish model. As seen with BTP15, most of the molecules were found to be toxic for the embryos. The maximal drug concentrations tolerated for this assay are listed in Table 1. As BTP derivatives are anti-virulence drugs, we thought that the effect of the treatment would be more pronounced if the molecules were added immediately after infection at 24 h post fertilization (hpf). This was not the case, as similar numbers of CFUs were recovered from treated and untreated groups (Figure 5b). Furthermore, we observed a higher larval death rate when the inhibitors were added to the embryo medium at 24 hpf than at 48 hpf, at the same concentration (data not shown), suggesting that younger embryos are more sensitive to toxicity related to BTPs. These observations suggest that, at the maximal tolerated concentrations, the drugs do not prevent cytosolic escape and this does not reduce bacterial loads in zebrafish embryos when compared to untreated groups.

Two BTP analogues, **11826191** and **11826192**, were tolerated at concentrations of $>10 \mu\text{g/mL}$. The assay was thus repeated with a higher number of larvae and the inhibitors were added at 50 $\mu\text{g/mL}$ immediately after infection. Although the embryos survived 4 d of drug exposure, CFU counts revealed no significant bacterial inhibition compared to untreated controls. A weak tendency nevertheless appeared for the embryos treated with **11826192** (Figure 5c).

Finally, BTP15 was proven to prevent EsxA secretion and protect infected lung fibroblasts without impacting the growth of *M. tuberculosis*.³⁵ We thus hypothesized that the bacteria could be chemically attenuated by exposure to the drug before zebrafish infection. 20 μM BTP15 was added

in a culture of *M. marinum* 12 h before the bacteria were collected and prepared for microinjection in the embryos. Infected larvae were subsequently kept in the presence of 1 µg/mL of BTP15 or left untreated. Again, no difference with the control could be observed upon CFU enumeration indicating that the inhibitor had no significant effect with this setup (Figure 5d).

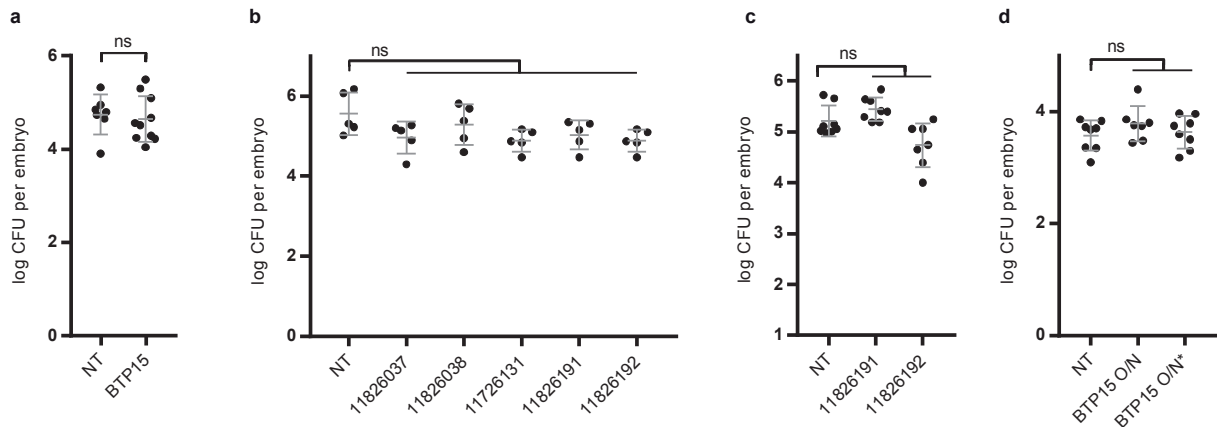


Figure 5. Anti-virulence activity of BTP analogues in *M. marinum*-infected zebrafish embryos. **a**, CFUs recovered from zebrafish embryos infected with *M. marinum* M and exposed to 1 µg/mL BTP15 from 1 to 4 dpi, or left untreated (NT). **b**, CFU count from zebrafish larvae infected with *M. marinum* M and exposed to the indicated BTP analogues immediately after infection and for 4 d (11826037, 11826031: 1 µg/mL; 11726131, 11826191, 11826192: 5 µg/mL). **c**, Same as **b**, with 11826191 and 11826192 added immediately after infection at 50 µg/mL. **d**, *M. marinum* (E11) cultures were treated for 12 h with 20 µM of BTP15 prior to infection. NT – non-treated bacteria and untreated fish, BTP15 O/N – bacterial cultures treated with BTP15 before infection, BTP15 O/N* – bacterial cultures treated with BTP15 before infection and addition of 1 µg/mL BTP15 in embryo medium immediately after infection. ns = non-significant.

Name	Conc.^a ($\mu\text{g}/\text{mL}$)
BTP15	1
11726131	5
11826037	1
11826038	1
11826191	50
11826192	100

Table 1. Benzothioephene analogues used in this investigation. ^a Maximal concentration tolerated by zebrafish embryos when the drug was added at 48 hpf

ACTIVITY OF ARYLVINYLPIPERAZINE AMIDES AGAINST *M. ABSCESSUS* *IN VIVO*

Background Information

Mycobacteroides abscessus, subsp. *abscessus* (*M. abscessus*) is a ubiquitous emerging pathogen responsible for diverse nontuberculous mycobacterium (NTM)-related diseases in humans, mostly chronic pulmonary infections in immunosuppressed and cystic fibrosis patients.³⁷ It is a rapidly growing mycobacterial species possessing some important pathogenic traits.¹² Although *M. abscessus* is an opportunistic pathogen, this species is intrinsically resistant to many available antibiotics, rendering infections highly difficult to cure. For instance, *M. abscessus* is resistant to all frontline anti-TB drugs,³⁸ which can pose serious problems, especially if misdiagnosed as an *M. tuberculosis* infection. Despite restricted availability of animal and cellular infection models, the zebrafish has proven to be a suitable organism to study *M. abscessus* pathogenesis.¹³ Furthermore, *M. abscessus* is genetically accessible and fluorescent reporters have been used to evaluate the efficacy of antibiotics *in vivo*.^{12,39}

In 2013, 177 hit compounds were identified in a large scale phenotypic screen against *M. tuberculosis* and *M. bovis* BCG by GlaxoSmithKline.⁴⁰ Among these hits, an arylvinylpiperazine amide compound, AX-35, showed potent activity against *M. tuberculosis* and its mechanism of action, as well as SAR studies, have been investigated in a recent study.⁴¹ QcrB, a subunit of cytochrome *bc*₁ oxidase (one of the two terminal oxidases in the electron transport chain), was found to be the direct target of this compound, which displayed bacteriostatic activity in wild type *M. tuberculosis*. Notably, AX-35 exhibits anti-mycobacterial activity against several NTM including *M. abscessus*. The activity of arylvinylpiperazine amide derivatives against NTMs is currently under investigation and the *in vivo* activity of some of these derivatives in the zebrafish model is the subject of the study described below.

Optimization of an *in vivo* drug efficacy assay against *M. abscessus* with arylvinylpiperazine amide derivatives

Infection of zebrafish embryos was performed by microinjection of an *M. abscessus* suspension, as for infections with *M. marinum* and as described elsewhere.¹³ Interestingly, *M. abscessus* does not tolerate alkaline decontamination and no mycobacteria were recovered after only 1 min of incubation with MycoPrep. *M. abscessus*-infected zebrafish embryos were thus disrupted in 5% SDS and homogenates were diluted and plated on 7H10 containing a mixture of polymyxin B, amphotericin B, nalidixic acid, trimethoprim and azlocillin (PANTA). Subsequent experiments revealed that nalidixic acid, azlocillin and cycloheximide (NAC) is sufficient to isolate *M. abscessus* from zebrafish lysates without additional decontamination.

Embryos were exposed to several concentrations of arylvinylpiperazine amide analogues (Table 2) and drug-related toxicity was revealed by the death of all the larvae in several groups as early as one day after compounds were added, even at low doses. The maximum concentration tolerated in this assay was estimated for each compound (Table 2) and for all the drugs except AX-50, it was found to be lower than the *in vitro* minimal inhibitory concentration (MIC). The macrolide antibiotic clarithromycin (CLR), recommended to treat *M. abscessus* infections in humans,⁴² was used as a positive control for this assay. Exposure of infected embryos to 1 mg/mL CLR for 3 d led to a significant reduction in bacterial load, as previously reported,¹² and embryos did not display any signs of toxicity-related malformation. In contrast, addition of 0.5 µg/mL AX-35 for only 24 h (from 24 to 48 h post infection, followed by transfer into drug-free E3) led to the death of half of the larvae in that group, and the survivors had a similar bacterial load as the untreated group, at the end of the experiment (Figure 6a). Another positive control experiment with bedaquiline (BDQ, 4 µg/mL) led to a slight reduction in CFUs as previously observed by others (Figure 6b).³⁹

In an attempt to assess drug efficacy while reducing embryonic death rate, the drugs AX-35 and AX-50 were added immediately after the infection and larvae were homogenized 24 h later. However, the CFU numbers were similar between the treated and the untreated groups (Figure 6c). Finally, infected embryos were exposed to AX-35 and AX-50 only 2.5 h per day for 4 d, starting on the day of infection, and were maintained in drug-free E3 otherwise. After the fourth dose, all embryos exposed to AX-35 had died and no difference between AX-50-treated and untreated fish were observed upon CFU enumeration (Figure 6d). Taken together, these observations suggest that arylvinylpiperazine amide analogues are too toxic to be evaluated in zebrafish embryos, given the high drug concentration necessary to observe a reduction of *M. abscessus* load in this model.

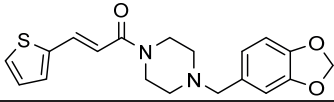
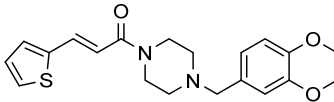
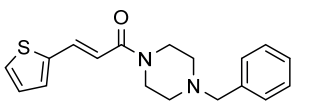
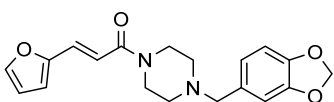
Name	Molecular structure	Conc. ^a ($\mu\text{g/mL}$)	MIC ^b ($\mu\text{g/mL}$)
AX-35		<0.5	3.3
AX-50		8	8.7
JW010		8	12.2
JW011		2	4.9
CLR		>1000	0.9

Table 2. Arylvinyloperazine amide derivatives used in this study. ^a Maximal concentration tolerated by zebrafish embryos when the drug was added at 48 hpf. ^b Minimal inhibitory concentration for *M. abscessus* measured by REMA *in vitro*.

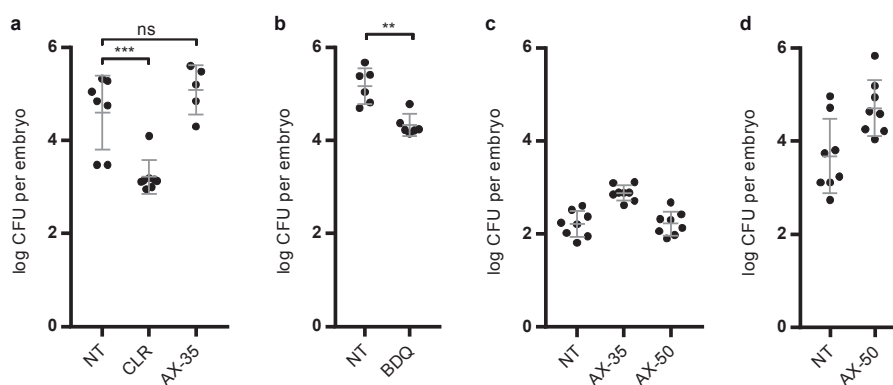


Figure 6. *In vivo* activity of arylvinylpiperazine amide derivatives and control drugs against *M. abscessus*. **a**, *M. abscessus*-infected embryos were exposed to 1 mg/mL CLR from 1 to 4 dpi or to 0.5 $\mu\text{g/mL}$ AX-35 for 24 h at 1 dpi. Surviving larvae were homogenized at 4 dpi and samples were plated for CFU enumeration. **b**, Embryos were exposed to 4 $\mu\text{g/mL}$ BDQ from 1 to 4 dpi or left untreated, before homogenization, plating and CFU count. **c**, Embryos were infected with *M. abscessus* and immediately exposed to 0.5 $\mu\text{g/mL}$ AX-35, 8 $\mu\text{g/mL}$ AX-50 or left untreated. Samples were homogenized and plated 24 h later. **d**, Infected zebrafish embryos were exposed to 10 $\mu\text{g/mL}$ AX-35 or 20 $\mu\text{g/mL}$ AX-50 2.5 h per day for 4 successive days, or left untreated. All larvae from the AX-35-treated group died after the fourth dose and data are thus not displayed. ** $P = 0.0008$, *** $P = 0.001$, ns = non-significant.

GENERAL DISCUSSION

Zebrafish embryos have become an attractive alternative to mouse models for the study of mycobacterial pathogenesis. Infection of zebrafish embryos permits for instance to rapidly assess the activity of antimicrobials *in vivo* over 5 d. In addition, low absolute amounts of drugs are necessary to treat up to 12 embryos simultaneously in 4 mL of fish water (concentrations are generally <500 µg/mL), whereas drug efficacy assays in mice require several milligrams of compound (e.g. 25 mg/kg for INH) and daily administration to every animal for several weeks. This could be a serious issue when experimental synthetic compounds have to be tested *in vivo*.

With the zebrafish model, we demonstrate here for the first time that the natural product pyridomycin and one of its synthetic analogues, DM122, have anti-mycobacterial activity *in vivo*, without causing side-effects in the larvae. We also demonstrate that the anti-leprosy drug clofazimine has specific anti-mycobacterial efficacy in zebrafish embryos infected with *M. marinum*, at concentrations as low as 1 µg/mL. Our initial aim was to test whether an *fadD9::tn* mutant shows a CFM-resistance phenotype only intracellularly and the zebrafish was our model of choice. Our observations indicated that disruption of the *fadD9* gene in *M. marinum* is not sufficient to confer resistance to CFM in our model. One can hypothesize that the resistance phenotype may appear later, following a change in host or pathogen metabolism in response to CFM. Testing this hypothesis would require extending the time window of our zebrafish-*M. marinum* infection assay, which becomes then ethically debatable. CFUs recovered from infected and treated larvae were our main readout to assess drug efficacy. However, alternatives can be explored, such as larval survival, as already reported for *M. abscessus*-infected embryos.^{12,39}

Inhibitors of mycobacterial virulence factor secretion do not kill the bacteria but do attenuate virulence. Such “chemical attenuation” of pathogenic bacteria is a rather elegant strategy, however the toxicity of BTP analogues for zebrafish embryos greatly limited their use in our model. BTP15 prevented the secretion of EsxA via the ESX-1 secretion system, a major virulence factor in *M. tuberculosis*.³⁵ Alternatively, *M. marinum* mutants lacking the RD1 region⁴³ (in which the genes required for a functional ESX-1 system are located) or with a disrupted ESX-1 system⁸ (in an *eccCb1::tn* mutant, EccCb1 being an essential component of ESX-1) were phenotypically characterized by reduced initial granuloma formation upon zebrafish embryo infection. If BTP analogues truly attenuate ESX-1-dependent secretion, one could look for inhibition of early granuloma formation in BTP-treated fish using fluorescent reporters instead of counting CFUs. Finally, BTP15 and BTP analogues have been characterized for their anti-virulence activity in *M. tuberculosis*, not in *M. marinum*. Differences in activities of BTP analogues between

M. tuberculosis and *M. marinum* could be explained by the presence of more efflux systems in the latter, as well as differences in the active site of the target, MprB. Microbiological and biochemical validation should be therefore undertaken with these inhibitors in *M. marinum* in further studies.

Mouse models of *M. abscessus* infection for preclinical drug testing have been reported with granulocyte-macrophage colony-stimulating factor knockout (GM-CSF KO) mice and intrapulmonary delivery of bacteria,⁴⁴ or nude mice (lacking T cells) with intravenous injection of a bacterial suspension.⁴⁵ However, in wild-type mice, *M. abscessus* fails to establish a persistent infection after aerosol exposure.¹² Zebrafish embryos may be a useful alternative to study *M. abscessus* pathogenesis¹³ and have already been used for drug discovery.^{12,39} We thus used zebrafish to test the *in vivo* efficacy of a new class of anti-mycobacterial compounds, arylvinylpiperazine amide derivatives. Notably, these drugs, targeting QcrB in *M. tuberculosis*,⁴¹ display specific antimicrobial activity towards nontuberculous mycobacteria, including *M. abscessus*. All the tested compounds were found to be lethal for the zebrafish embryos and no therapeutic effect could be observed, despite variations of drug concentrations and exposure times. Although toxicity did not seem to be an issue in the mouse model of acute tuberculosis,⁴¹ our observations in zebrafish should be taken as a warning for potential side-toxicity or off-target consequences of this class of compounds which may delay progression to the clinic. Medicinal chemistry and toxicological investigations are thus necessary to identify causes of toxicity and to ameliorate the compounds accordingly.

Finally, zebrafish embryo are versatile, faster and cheaper alternatives to rodents in anti-TB drug discovery, permitting an increase in throughput and boosting the development of anti-mycobacterial compounds. One can safely conclude that zebrafish provide an excellent platform to investigate the mechanisms of mycobacterial pathogenesis, identify and understand key bacterial virulence factors and develop new approaches to anti-mycobacterial therapies.

METHODS

Bacterial strains and culture conditions

M. marinum strains E11,⁴⁶ M⁴⁷ and mutants, kindly provided by Astrid van der Sar and Wilbert Bitter, were grown in Middlebrook 7H9 medium (Difco) supplemented with 0.2% glycerol, 0.05% Tween-80 and 10% albumin-dextrose-catalase (ADC) or on solid 7H10 agar plates containing 0.5% glycerol and 10% oleic acid-albumin-dextrose-catalase (OADC). Cultures were incubated at 30°C. Hygromycin (HYG, 50 µg/mL) or kanamycin (KAN, 25 µg/mL) were added in culture medium when appropriate. Strain E11 was used for all experiments related to pyridomycin and DM122, except for fluorescence measurements in which case the reporter was constructed in an M background (see below). Strain M WT and *fadD9::tn* were used in all experiments with clofazimine. For assays with benzothiophene, the strains used are indicated in the figure legend.

M. abscessus sensu stricto (rough variant of strain CIP104536^T (ATCC19977T)) expressing *tdTomato* was a kind gift from Laurent Kremer.⁴⁸ *M. abscessus* was grown at 30°C in 7H9 containing 0.2% glycerol, 0.05% Tween-80 and 10% OADC or on 7H10 agar plates containing 0.5% glycerol and 10% OADC, in presence of 500 µg/mL HYG.

Construction of an *M. marinum* fluorescent reporter

To generate a fluorescent *M. marinum* reporter strain, the plasmid pCHARGE3,⁴⁹ kindly provided by Tanya Parish (Addgene plasmid # 24658), was transformed in parental *M. marinum* strain M by electroporation, as previously described.⁵⁰ This reporter constitutively (under the strong *hsp60* promoter) produces the far-red fluorescent protein Turbo-635 (also named Katushka⁵¹), whose gene was codon-optimized for expression in mycobacteria.

Infection of zebrafish embryos

Zebrafish embryos were infected with *M. marinum* or *M. abscessus* as previously described.^{8,10,13} Briefly, 24 h old *Danio rerio* (AB) embryos were manually dechorionated and aligned on a custom-made agarose bed covered with E3 medium⁵² (5 mM NaCl, 0.17 mM KCl, 0.33 mM CaCl₂, 0.33 mM MgSO₄) containing 0.4 mg/mL MS-222 (Sigma). A bacterial suspension containing ~300 bacteria in 1-2 nL was microinjected in the caudal vein of anesthetized embryos using a heat-pulled glass capillary connected to a pneumatic PicoPump PV820 (World Precision Instruments). 24 h after infection, unless specified differently, embryos were split into groups of 8-12 and placed in 4 mL of E3 in 6-well plates and drugs were added directly in E3 at the concentrations indicated. The embryos were maintained at 28°C until the end of the experiment (4 dpi unless specified

differently). For the measurement of embryonic lengths, pictures were taken with a Leica DFC295 camera mounted on a Leica M125 stereomicroscope and analysed with ImageJ (v1.52h).

Enumeration of mycobacteria in infected zebrafish embryos

Lysis and decontamination of embryos was performed as described elsewhere⁸ for *M. marinum* isolation, with some modifications. At the end of the experiment, embryos were euthanized with an overdose of MS-222 and single specimens were incubated in for 5 min in 25 μ L 5% SDS in PBS. Larvae were disrupted by pipetting and 25 μ L of BBL MycoPrep (BD) was added. The samples were incubated at room temperature for 10 min under shaking and neutralized by addition of 450 μ L of PBS. Serial 10-fold dilutions were plated on 7H10 medium containing 10 μ g/mL cycloheximide and cultured at 30°C for 8 d before CFU enumeration.

M. abscessus-infected embryos were disrupted in 25 μ L 5% SDS in PBS, diluted in 500 μ L PBS and plated on 7H10 containing the antibiotic mixtures PANTA (40 U/mL polymyxin B, 4 μ g/mL amphotericin B, 16 μ g/mL nalidixic acid sodium salt, 4 μ g/mL trimetoprim and 4 μ g/mL azlocillin sodium salt) or NAC (16 μ g/mL nalidixic acid sodium salt, 4 μ g/mL azlocillin sodium salt and 10 μ g/mL cycloheximide). Plates were incubated at 37°C for 3-4 d before CFU enumeration.

***M. marinum* load evaluation with fluorescence measurement**

At 4 dpi, single anesthetized zebrafish embryos were dispensed in black clear-bottom 96-well plates. Twelve fluorescence reads per well were measured with a Tecan M200 plate-reader (top reading, excitation 558 nm and emission 653 nm) and the signal was averaged for each well. For fluorescence measurements, $n = 12$ embryos per group.

Culture pre-treatment with BTP15

M. marinum E11 was grown to an OD₆₀₀ of 0.3, 20 μ M of BTP15 was added and the culture was further kept at 30°C under agitation overnight. The next morning, bacterial cultures were centrifuged, resuspended in 0.5% Tween-80 in PBS to disrupt clumps, centrifuged and resuspended in 7H9 at an OD₆₀₀ of 4, diluted 1:4 in a 0.5% phenol red solution and prepared for injection as described above. An untreated control was prepared and administered in parallel to a separate group of fish.

Statistics

Statistical analysis was carried out with GraphPad Prism version 7.02. When two groups were compared, a Mann Whitney test was used. When more than two groups were compared, an ordinary one-way ANOVA followed by a Tukey's multiple comparisons test were performed. Groups contained between 8 and 12 elements unless specified differently.

REFERENCES

1. van Leeuwen, L. M., van der Sar, A. M. & Bitter, W. Animal models of tuberculosis: zebrafish. *Cold Spring Harb. Perspect. Med.* **5**, a018580 (2014).
2. Lesley, R. & Ramakrishnan, L. Insights into early mycobacterial pathogenesis from the zebrafish. *Curr. Opin. Microbiol.* **11**, 277–283 (2008).
3. Ramakrishnan, L. The zebrafish guide to tuberculosis immunity and treatment. *Cold Spring Harb. Symp. Quant. Biol.* **78**, 179–192 (2013).
4. Ramakrishnan, L. Looking within the zebrafish to understand the tuberculous granuloma. *Adv. Exp. Med. Biol.* **783**, 251–266 (2013).
5. van der Sar, A. M., Appelmelk, B. J., Vandenbroucke-Grauls, C. M. J. E. & Bitter, W. A star with stripes: zebrafish as an infection model. *Trends Microbiol.* **12**, 451–457 (2004).
6. Tobin, D. M. & Ramakrishnan, L. Comparative pathogenesis of *Mycobacterium marinum* and *Mycobacterium tuberculosis*. *Cell. Microbiol.* **10**, 1027–1039 (2008).
7. Cronan, M. R. & Tobin, D. M. Fit for consumption: zebrafish as a model for tuberculosis. *Dis. Model. Mech.* **7**, 777–784 (2014).
8. Stoop, E. J. M. *et al.* Zebrafish embryo screen for mycobacterial genes involved in the initiation of granuloma formation reveals a newly identified ESX-1 component. *Dis. Model. Mech.* **4**, 526–536 (2011).
9. Takaki, K., Cosma, C. L., Troll, M. A. & Ramakrishnan, L. An *in vivo* platform for rapid high-throughput antitubercular drug discovery. *Cell Rep.* **2**, 175–184 (2012).

10. Takaki, K., Davis, J. M., Winglee, K. & Ramakrishnan, L. Evaluation of the pathogenesis and treatment of *Mycobacterium marinum* infection in zebrafish. *Nat. Protoc.* **8**, 1114–1124 (2013).
11. Makarov, V. *et al.* Towards a new combination therapy for tuberculosis with next generation benzothiazinones. *EMBO Mol. Med.* **6**, 372–383 (2014).
12. Bernut, A. *et al.* *In vivo* assessment of drug efficacy against *Mycobacterium abscessus* using the embryonic zebrafish test system. *Antimicrob. Agents Chemother.* **58**, 4054–4063 (2014).
13. Bernut, A. *et al.* Deciphering and imaging pathogenesis and cording of *Mycobacterium abscessus* in zebrafish embryos. *J. Vis. Exp.* e53130 (2015).
14. Maeda, K., Kosaka, H., Okami, Y. & Umezawa, H. A new antibiotic, pyridomycin. *J. Antibiot. (Tokyo)* **6**, 140 (1953).
15. Hartkoorn, R. C. *et al.* Towards a new tuberculosis drug: pyridomycin – nature’s isoniazid. *EMBO Mol. Med.* **4**, 1032–1042 (2012).
16. Hartkoorn, R. C. *et al.* Pyridomycin bridges the NADH- and substrate-binding pockets of the enoyl reductase InhA. *Nat. Chem. Biol.* **10**, 96–98 (2014).
17. Horlacher, O. P., Hartkoorn, R. C., Cole, S. T. & Altmann, K.-H. Synthesis and antimycobacterial activity of 2,1'-dihydropyridomycins. *ACS Med. Chem. Lett.* **4**, 264–268 (2013).
18. WHO Regional Office for South-East Asia. *Guidelines for the diagnosis, treatment and prevention of leprosy.* (World Health Organization Regional Office for South-East Asia, 2018).
19. Van Deun, A. *et al.* Short, highly effective, and inexpensive standardized treatment of multidrug-resistant tuberculosis. *Am. J. Respir. Crit. Care Med.* **182**, 684–692 (2010).
20. Grosset, J. H. *et al.* Assessment of clofazimine activity in a second-line regimen for tuberculosis in mice. *Am. J. Respir. Crit. Care Med.* **188**, 608–612 (2013).
21. Tyagi, S. *et al.* Clofazimine shortens the duration of the first-line treatment regimen for experimental chemotherapy of tuberculosis. *Proc. Natl. Acad. Sci. U. S. A.* **112**, 869–874 (2015).

22. Lechartier, B. & Cole, S. T. Mode of action of clofazimine and combination therapy with benzothiazinones against *Mycobacterium tuberculosis*. *Antimicrob. Agents Chemother.* **59**, 4457–4463 (2015).
23. Lupien, A. *et al.* Optimized background regimen for treatment of active tuberculosis with the next-generation benzothiazinone macozinone (PBTZ169). *Antimicrob. Agents Chemother.* **62**, e00840-18 (2018).
24. Yano, T. *et al.* Reduction of clofazimine by mycobacterial type 2 NADH:quinone oxidoreductase: a pathway for the generation of bactericidal levels of reactive oxygen species. *J. Biol. Chem.* **286**, 10276–10287 (2011).
25. Andries, K. *et al.* A diarylquinoline drug active on the ATP synthase of *Mycobacterium tuberculosis*. *Science* **307**, 223–227 (2005).
26. Diacon, A. H. *et al.* Randomized pilot trial of eight weeks of bedaquiline (TMC207) treatment for multidrug-resistant tuberculosis: long-term outcome, tolerability, and effect on emergence of drug resistance. *Antimicrob. Agents Chemother.* **56**, 3271–3276 (2012).
27. Hartkoorn, R. C., Uplekar, S. & Cole, S. T. Cross-resistance between clofazimine and bedaquiline through upregulation of MmpL5 in *Mycobacterium tuberculosis*. *Antimicrob. Agents Chemother.* **58**, 2979–2981 (2014).
28. Benjak, A. *et al.* Phylogenomics and antimicrobial resistance of the leprosy bacillus *Mycobacterium leprae*. *Nat. Commun.* **9**, 352 (2018).
29. Sassetti, C. M., Boyd, D. H. & Rubin, E. J. Genes required for mycobacterial growth defined by high density mutagenesis. *Mol. Microbiol.* **48**, 77–84 (2003).
30. Griffin, J. E. *et al.* High-resolution phenotypic profiling defines genes essential for mycobacterial growth and cholesterol catabolism. *PLoS Pathog.* **7**, e1002251 (2011).
31. Job, C. K., Yoder, L., Jacobson, R. R. & Hastings, R. C. Skin pigmentation from clofazimine therapy in leprosy patients: a reappraisal. *J. Am. Acad. Dermatol.* **23**, 236–241 (1990).
32. Rasko, D. A. & Sperandio, V. Anti-virulence strategies to combat bacteria-mediated disease. *Nat. Rev. Drug Discov.* **9**, 117–128 (2010).

33. Chen, J. M., Pojer, F., Blasco, B. & Cole, S. T. Towards anti-virulence drugs targeting ESX-1 mediated pathogenesis of *Mycobacterium tuberculosis*. *Drug Discov. Today Dis. Mech.* **7**, e25–e31 (2010).
34. Bitter, W. & Kuijl, C. Targeting bacterial virulence: the coming out of type VII secretion inhibitors. *Cell Host Microbe* **16**, 430–432 (2014).
35. Rybniker, J. *et al.* Anticytolytic screen identifies inhibitors of mycobacterial virulence protein secretion. *Cell Host Microbe* **16**, 538–548 (2014).
36. Leon, J. D. *et al.* *Mycobacterium tuberculosis* ESAT-6 exhibits a unique membrane-interacting activity that is not found in its ortholog from non-pathogenic *Mycobacterium smegmatis*. *J. Biol. Chem.* **287**, 44184–44191 (2012).
37. Medjahed, H., Gaillard, J.-L. & Reyrat, J.-M. *Mycobacterium abscessus*: a new player in the mycobacterial field. *Trends Microbiol.* **18**, 117–123 (2010).
38. Brown-Elliott, B. A. & Philley, J. V. Rapidly growing mycobacteria in *Tuberculosis and Nontuberculous Mycobacterial Infections, Seventh Edition* (ed. Schlossberg D.) 703–723 (ASM Press, Washington, DC, 2017).
39. Dupont, C. *et al.* Bedaquiline inhibits the ATP synthase in *Mycobacterium abscessus* and is effective in infected zebrafish. *Antimicrob. Agents Chemother.* **61**, e01225-17 (2017).
40. Ballell, L. *et al.* Fueling open-source drug discovery: 177 small-molecule leads against tuberculosis. *ChemMedChem* **8**, 313–321 (2013).
41. Foo, C. S. *et al.* Arylvinylpiperazine amides, a new class of potent inhibitors targeting QcrB of *Mycobacterium tuberculosis*. *mBio* **9**, e01276-18 (2018).
42. Griffith, D. E. *et al.* An official ATS/IDSA statement: diagnosis, treatment, and prevention of nontuberculous mycobacterial diseases. *Am. J. Respir. Crit. Care Med.* **175**, 367–416 (2007).
43. Volkman, H. E. *et al.* Tuberculous granuloma formation is enhanced by a *Mycobacterium* virulence determinant. *PLoS Biol.* **2**, e367 (2004).
44. De Groote, M. A. *et al.* GM-CSF knockout mice for preclinical testing of agents with antimicrobial activity against *Mycobacterium abscessus*. *J. Antimicrob. Chemother.* **69**, 1057–1064 (2014).

45. Lerat, I. *et al.* *In vivo* evaluation of antibiotic activity against *Mycobacterium abscessus*. *J. Infect. Dis.* **209**, 905–912 (2014).
46. van der Sar, A. M. *et al.* *Mycobacterium marinum* strains can be divided into two distinct types based on genetic diversity and virulence. *Infect. Immun.* **72**, 6306–6312 (2004).
47. Ramakrishnan, L. & Falkow, S. *Mycobacterium marinum* persists in cultured mammalian cells in a temperature-restricted fashion. *Infect. Immun.* **62**, 3222–3229 (1994).
48. Bernut, A. *et al.* *Mycobacterium abscessus* cording prevents phagocytosis and promotes abscess formation. *Proc. Natl. Acad. Sci. U. S. A.* **111**, e943-52 (2014).
49. Carroll, P. *et al.* Sensitive detection of gene expression in mycobacteria under replicating and non-replicating conditions using optimized far-red reporters. *Plos One* **5**, e9823 (2010).
50. Parish, T. & Stoker, N. G. Electroporation of mycobacteria. *Methods Mol. Biol.* **101**, 129–144 (1998).
51. Shcherbo, D. *et al.* Bright far-red fluorescent protein for whole-body imaging. *Nat. Methods* **4**, 741–746 (2007).
52. Brand, M. & Granato, M. Keeping and raising zebrafish in *Zebrafish: A Practical Approach* (eds. Nusslein-Volhard, C. and Dahm, R.) 7–37 (Oxford Univ. Press, Oxford, 2002).

PART IV

RETROSPECTIVES AND PERSPECTIVES

Chapter 7.

Conclusion and Outlook

The work presented in the previous chapters benefits from extensive interdisciplinarity involving a variety of approaches, ranging from chemical biology, genetic engineering of mycobacterial reporters and *in vivo* models of TB infection in mice (*Mus musculus*) and zebrafish (*Danio rerio*). Engineered mycobacterial species have been applied in different contexts, for instance as reporters to visualize TB infection in zebrafish and mice and, in the case of *M. marinum* and *M. abscessus*, as the basis of a zebrafish model of mycobacterial infection. Strong emphasis was placed on the application of these tools to anti-TB drug assessment thus highlighting the benefits of alternative approaches, in saving precious time and substantial resources.

Innovative drugs and treatment strategies are necessary to stop the global TB epidemic and BTZs constitute a highly potent new class of anti-TB drugs, macozinone being undoubtedly the most promising one.¹⁻³ Results presented in this thesis contributed to the validation of its efficacy in mouse and zebrafish models, evaluated not only by CFU enumeration but also with innovative quantitative *in vivo* imaging techniques. Besides its powerful anti-TB character, PBTZ169 proved to be an excellent scaffold to design specific and selective fluorescent probes, following a chemical biology approach.⁴ In chapter 2, we presented the development and characterisation of fluorophore-coupled BTZ molecules permitting the subcellular polar and periplasmic localization of DprE1 to be visually assessed, by means of high- and super-resolution imaging techniques. A single amino acid mutation in DprE1 abolished the binding of the most advanced probe, **JN108**, which is consistent with the mechanism of action of BTZs. We further demonstrated that such observations were valid for other BTZ-sensitive actinobacterial species.

Thanks to their high selectivity for DprE1, such probes are valuable tools for the detection of a defined number of bacterial species in different contexts, especially applicable to pathogenic mycobacteria such as *M. marinum* or *M. tuberculosis*. The application of fluorescent BTZs to potentially contaminated samples may therefore enable the presence of *M. tuberculosis* to be revealed, with patient derived sputum samples for example. More recently, the development of a Respiratory Aerosol Sampling Chamber (RASC), consisting of a personal clean room connected to sampling devices for sampling of airborne particles,^{5,6} may provide a cleaner source of patient-derived samples that can readily be analysed with *M. tuberculosis*-specific probes, such as **JN108** (Digby Warner, personal communication). Furthermore, the development of such probes in appropriate formulations could enable the identification of mycobacterial pathogens *in situ*. This could be the case for cutaneous BTZ-susceptible pathogens such as *M. marinum* or *M. leprae*. Together, these considerations highlight the potential of fluorescent BTZ analogues for the development of innovative diagnostic tools for mycobacterial pathogen detection.

Interestingly, a recent study reported the development and application of a dual-targeting fluorogenic probe that selectively labels *M. tuberculosis* and other bacteria *in vitro* and in sputum samples.⁷ The probe was designed with a quencher that is released upon hydrolysis by the β -lactamase BlaC, naturally produced by *M. tuberculosis*. Hydrolysis of the quencher activates the fluorescent probe, which also carries a chemical group that covalently labels DprE1 with a similar mechanism to **JN108**. Notably, the reported specific probe is not derived from a BTZ moiety. By coupling DprE1- and BlaC-specific probes, the authors can discriminate live and dead mycobacteria as well as *M. tuberculosis* from other bacteria, and the utilization of a simple microfluidic chip facilitated their detection *in vitro*, corroborating the potential of DprE1-targeting probes for TB diagnostics.

Given the high specificity of **JN108** *in vitro*, we sought to evaluate its capacity to detect mycobacteria *in vivo*, for imaging purposes as discussed in chapter 3. This was attempted in infected zebrafish embryos but the probe could not specifically detect the bacteria over background fluorescence, although green fluorescent *M. marinum* reporters could be easily seen with confocal microscopy. For the application in infected mice, a NIR variant of **JN108**, **JN139**, was used. This probe is based on the Dy-750 fluorochrome that emits around 750 nm. **JN139** could be detected in the abdomen after intraperitoneal injection into mice, confirming the high suitability of NIR probes for imaging in rodents. However, **JN139** failed to label *M. tuberculosis* in the lungs sufficiently for detection, suggesting that the biodistribution of this probe was not adequate. A fluorogenic β -lactamase probe emitting at 795 nm has nonetheless been successfully applied for the quantitative detection of mycobacterial infection in mouse lungs.⁸⁻¹² This probe was also designed with a quencher and β -lactamase activated the probe upon hydrolysis of the quencher. Although β -lactam probes may be sensitive to β -lactamases from bacteria other than *M. tuberculosis*, the authors reported a high sensitivity, enabling the detection of <1000 CFUs in the lungs of live experimentally infected mice in their most recent study.⁸ Fluorogenicity and NIR wavelengths, combined with the best detection equipment, seem to be key for optimal and sensitive quantification of mycobacterial infection with fluorescent probes in mice.

Beside fluorescent probes for *in vivo* imaging, reporters carrying genetically engineered fluorescent proteins have been applied for *in vivo* imaging of mycobacterial infection. Notably, tdTomato^{13,14} and Turbo635¹⁵ enabled mycobacteria to be seen *in vivo*. In chapter 4, we reported for the first time the application to mycobacteria of the newly developed NIR fluorescent protein (iRFP).¹⁶ Autofluorescent NIR reporter strains of *M. smegmatis*, *M. marinum* and *M. tuberculosis* have been successfully designed by cloning the *iRFP* gene together with *ho1*, encoding the heme oxygenase 1 (HO1). HO1 generates an intrabacterial pool of biliverdin (BV), the cofactor necessary for iRFP to

fluoresce. The reporter strains emit at a maximal wavelength of 713 nm. NIR *M. marinum* could be visualized in zebrafish embryos and NIR *M. tuberculosis* in the lungs of infected SHO mice. In both cases, quantitative fluorescence measurements provided precise real-time information on antibiotic treatment efficacy. The successful visualization of *M. tuberculosis* in live mice can be attributed to the NIR emission wavelength of the reporters, less subjected to absorption and scattering by mammalian tissues than blue-shifted wavelengths, and the immunodeficient/hairless phenotype of the mice, more permissive to *M. tuberculosis* multiplication and therefore favouring fluorescence detection. One major disadvantage intrinsic to iRFP and other NIR fluorescent proteins is their relatively weak brightness, rendering the emitted fluorescent signal difficult to detect. For example, the molecular brightness (product of molar extinction coefficient and quantum yield) of iRFP is 6'200 and that of tdTomato, which remains one of the brightest red fluorescent proteins known to date, is 48'000¹⁷. Further biochemical improvement of NIR fluorescent proteins derived from bacterial phytochromes is being undertaken to design brighter reporters, especially well-suited for *in vivo* imaging.^{18,19} Although these NIR fluorescent probes seem more attractive for application to eukaryotic cells so far, our study demonstrated their suitability for designing mycobacterial reporters thus paving the way for the utilisation of such tools in bacteria in general.

Fluorescence imaging requires irradiation with light at an appropriate wavelength to excite chromophores, which subsequently reemit photons that can be detected by the CCD camera. Mouse autofluorescence (skin, fur, food in the gut) is a major source of background signal although this phenomenon is attenuated in the NIR region. Deconvolution algorithms are necessary to improve the signal-to-noise ratio, while weak fluorescent signals may be completely masked by autofluorescence and therefore below the limit of detection. Bioluminescence on the other hand, does not require irradiation to produce photons and background autoluminescence originating from mammalian tissues is null when measurements are performed on live animals. The luminescence imaging modality enables therefore the detection of dimmer signals without the need for spectral deconvolution. In chapter 5, we applied autoluminescent *M. tuberculosis* reporters expressing the *luxCDABE* operon from *P. luminescens* to real-time imaging of TB in mice. This system did not require the exogenous administration of luciferin, as the *luxCDABE* cassette encodes the luciferase and the enzymes necessary for the biosynthesis of its substrate, providing a substantial advantage compared to firefly luciferase-based systems. Our protocol enabled the longitudinal imaging of the *M. tuberculosis* load in mice and a real-time assessment of isoniazid treatment, leading to a rapid reduction of the bacterial burden accompanied by a decrease in luminescence intensity in the thoracic area of mice. Our observations suggest that the kinetics and the temporal response to a treatment can be investigated in such a way, as well as the effect of drug dosage. This question is currently being investigated by repeating the key experiment described in

chapter 5, with different isoniazid dosages tested in parallel. Further characterisation of this infection system in SHO mice would be required to obtain a mathematical model that can predict the number of CFUs based on single bioluminescence measurements.

Many luciferase-based systems have been discovered, developed and applied to generate genetic reporters. Biochemical engineering of luciferases and new synthetic substrates enabled more efficient and longer (“glowing”) luminescence reactions, shifted emission wavelengths and smaller enzymes, for applications *in vitro* and *in vivo*.²⁰ Interestingly, NIR bioluminescent proteins for multimodal imaging have been recently developed.²¹ The authors designed chimeric probes based on *Renilla* luciferase fused with a NIR-fluorescent protein undergoing intramolecular bioluminescence resonance energy transfer (BRET), therefore spontaneously emitting a NIR signal without irradiation. BRET-probes are valuable tools for *in vivo* imaging, combining the advantages of spontaneous light emission and NIR wavelengths, and should be applied for the monitoring of bacterial infections.

Overall, fluorescence and bioluminescence imaging are complementary approaches. The latter enables the detection of weak signals thanks to the absence of background noise but requires the availability of substrate and cofactors, while fluorescence imaging is a versatile tool that exploits a large diversity of proteins and dyes emitting at numerous wavelengths. The availability of both luminescence and fluorescence imaging modalities in most *in vivo* imaging platforms enables dual-labelling possibilities, to study the metabolic state of mycobacteria upon infection, the response of the host (e.g. recruitment of immune cells) in real-time, the dissemination of bacteria in the organism and the response to antimicrobials. Further improvement of the detection devices (more sensitive CCD cameras) or optimized system design, including planar imaging and molecular tomography capabilities, would enable better spatiotemporal resolution and higher sensitivity. Finally, coupling optical imaging modalities with non-optical techniques, such as computed tomography and positron emission tomography, would also provide information about both the host and the pathogen upon infection.

Following the very same purpose of improving and boosting TB drug discovery and development with alternative methods, we implemented the zebrafish embryo model of mycobacterial infection and applied it to four different projects, as discussed in chapter 6. We successfully applied this model to demonstrate antimicrobial activity of the natural product pyridomycin and its synthetic analogue DM122 *in vivo* (Lupien A., *et al*, manuscript in preparation). Similarly, an assay was optimized to assess the repurposed drug clofazimine, which displayed anti-mycobacterial activity

against *M. marinum* in infected zebrafish embryos, while our attempts to link the role of *fadD9* inactivation in clofazimine resistance were inconclusive with this model.

Zebrafish embryos are an excellent platform to investigate mycobacterial pathogenesis and test the activity of new drugs. They provide observable readouts thanks to their optical transparency, rapid drug testing (results in <2 weeks), enable medium/high throughput screening and are genetically accessible for the study of important host factors during infection. One potential disadvantage, however, is the sensitivity of the embryos to drug-related toxicity, that arose for several compounds tested in our studies. Despite multiple optimization attempts, it was not possible to evaluate the anti-virulence properties of benzothiophene analogues and the anti-mycobacterial activity of arylvinylpiperazine amide derivatives in this model, as the compounds appeared toxic for fish larvae. One can speculate that the thiophene ring, also present in most arylvinylpiperazine amide derivatives tested, might be the source of embryonic toxicity in our assays. Daily and oral administration of these compounds to adult mice might enable a therapeutic effect to be observed, whereas a good compromise between antimicrobial activity and embryonic toxicity could not be determined with zebrafish larvae. These observations are nonetheless warnings of potential side effects that may arise and should therefore be taken into consideration.

Altogether, the multiple approaches undertaken in the present work were aimed at providing innovative approaches for TB diagnosis, as well as finding solutions to boost and refine the assessment of new anti-tubercular compounds. Furthermore, the implementation of real-time imaging for anti-TB drug activity assessment combined with the zebrafish embryo model is fully compatible with the 3R policy on animal experimentation, promoting replacement, reduction and refinement of animal use in biomedical research. Notably, every “R” of this policy is met with the different projects proposed in this thesis: *replacem*ent of the mouse model with zebrafish larvae, *reducti*on of the absolute number of animals enabled by longitudinal imaging, and *refin*ement of the drug assessment process via quantitative *in vivo* imaging. Besides providing advantageous substantial resources for TB drug development, our approaches also offer more ethically acceptable methodologies and biomedical applications.

REFERENCES

1. Lupien, A. *et al.* Optimized background regimen for treatment of active tuberculosis with the next-generation benzothiazinone macoquinone (PBTZ169). *Antimicrob. Agents Chemother.* **62**, e00840-18 (2018).
2. Makarov, V. *et al.* Benzothiazinones kill *Mycobacterium tuberculosis* by blocking arabinan synthesis. *Science* **324**, 801–804 (2009).
3. Makarov, V. *et al.* Towards a new combination therapy for tuberculosis with next generation benzothiazinones. *EMBO Mol. Med.* **6**, 372–383 (2014).
4. Sommer, R. *et al.* Fluorescent benzothiazinone analogues efficiently and selectively label DprE1 in mycobacteria and actinobacteria. *ACS Chem. Biol.* **13**, 3184–3192 (2018).
5. Wood, R. *et al.* Real-time investigation of tuberculosis transmission: developing the respiratory aerosol sampling chamber (RASC). *Plos One* **11**, e0146658 (2016).
6. Patterson, B. *et al.* Detection of *Mycobacterium tuberculosis* bacilli in bio-aerosols from untreated TB patients. *Gates Open Res.* **1**, 11 (2017).
7. Cheng, Y. *et al.* Rapid and specific labeling of single live *Mycobacterium tuberculosis* with a dual-targeting fluorogenic probe. *Sci. Transl. Med.* **10**, eaar4470 (2018).
8. Yang, H.-J. *et al.* Real-time imaging of *Mycobacterium tuberculosis* using a novel near-infrared fluorescent substrate. *J. Infect. Dis.* **215**, 405–414 (2017).
9. Sharan, R., Yang, H.-J., Sule, P. & Cirillo, J. D. Imaging *Mycobacterium tuberculosis* in mice with reporter enzyme fluorescence. *J. Vis. Exp.* e56801 (2018).
10. Sule, P., Tilwawala, R., Behinaein, P., Walkup, G. K. & Cirillo, J. D. New directions using reporter enzyme fluorescence (REF) as a tuberculosis diagnostic platform. *Tuberculosis* **101 Suppl**, S78-S82 (2016).
11. Kong, Y. *et al.* Imaging tuberculosis with endogenous beta-lactamase reporter enzyme fluorescence in live mice. *Proc. Natl. Acad. Sci. U. S. A.* **107**, 12239–12244 (2010).
12. Kong, Y. & Cirillo, J. D. Reporter enzyme fluorescence (REF) imaging and quantification of tuberculosis in live animals. *Virulence* **1**, 558–562 (2010).

13. Kong, Y. & Cirillo, J. D. Fluorescence imaging of mycobacterial infection in live mice using fluorescent protein-expressing strains. *Methods Mol. Biol.* **1790**, 75–85 (2018).
14. Kong, Y. *et al.* Application of fluorescent protein expressing strains to evaluation of anti-tuberculosis therapeutic efficacy *in vitro* and *in vivo*. *Plos One* **11**, e0149972 (2016).
15. Zelmer, A. *et al.* A new *in vivo* model to test anti-tuberculosis drugs using fluorescence imaging. *J. Antimicrob. Chemother.* **67**, 1948–1960 (2012).
16. Filonov, G. S. *et al.* Bright and stable near-infrared fluorescent protein for *in vivo* imaging. *Nat. Biotechnol.* **29**, 757–761 (2011).
17. Piatkevich, K. D. *et al.* Near-infrared fluorescent proteins engineered from bacterial phytochromes in neuroimaging. *Biophys. J.* **113**, 2299–2309 (2017).
18. Shcherbakova, D. M. & Verkhusha, V. V. Near-infrared fluorescent proteins for multicolor *in vivo* imaging. *Nat. Methods* **10**, 751–754 (2013).
19. Shcherbakova, D. M., Shemetov, A. A., Kaberniuk, A. A. & Verkhusha, V. V. Natural photoreceptors as a source of fluorescent proteins, biosensors, and optogenetic tools. *Annu. Rev. Biochem.* **84**, 519–550 (2015).
20. Coutant, E. P. & Janin, Y. L. Synthetic routes to coelenterazine and other imidazo[1,2- α]pyrazin-3-one luciferins: essential tools for bioluminescence-based investigations. *Chem. – Eur. J.* **21**, 17158–17171 (2015).
21. Rummyantsev, K. A., Turoverov, K. K. & Verkhusha, V. V. Near-infrared bioluminescent proteins for two-color multimodal imaging. *Sci. Rep.* **6**, 36588 (2016).

Acknowledgements

I am grateful to Prof. Stewart Cole for having offered me a position in his team for the last 4 years and for having proposed such an interesting (yet challenging) project, as well as for our valuable discussions and for his guidance during my entire PhD; to Prof. Andy Oates, who kindly accepted to join as co-advisor, for the insightful advice and discussions, for his open-mindedness and for his help concerning the zebrafish experiments; to Prof. Ulrich Schaible for having accepted to be part of the jury at my candidacy exam and thesis defense and for his wise advice; to Prof. Astrid van der Sar for having warmly welcomed me in her lab for a training on zebrafish infection techniques and for having joined my evaluation committee; to Dr. Neeraj Dhar for his technical assistance and advice as well as for the evaluation of this work; to Prof. Andrea Ablasser for having kindly accepted to chair my oral exam; to Dr. Laurel Rohde for having generously provided zebrafish eggs, for her help on zebrafish procedures and for having revised my thesis; to Prof. Melanie Blokesch for her mentoring; to my dear Martin for having carefully read and corrected my manuscripts; to the entire UPCOL team for technical help and assistance, notably Dr. Andréanne Lupien and Dr. Claudia Sala, for insightful discussions, for the great team spirit and support, especially among the PhD students of the lab; to all the past and present members of the GHI for making the institute a great place for work, sharing and learning; finally to my parents, family, friends, classmates and colleagues who unconditionally and continuously supported me during my studies at EPFL.

Lausanne, January 10, 2019



Raphael Sommer

Abbreviations

3R	Replace, reduce, refine	MDR	Multidrug-resistant
AIDS	Acquired immune deficiency syndrome	MIC, MIC ₉₉	Minimal inhibitory concentration
BCG	Bacille Calmette-Guérin	min	Minutes
BDQ	Bedaquiline (TMC207)	MTBC	<i>M. tuberculosis</i> complex
BTZ	Benzothiazinone	ND	Not determined
BV	Biliverdin	NHP	Non-human primate
CCD	Charge-coupled device	NI	Not infected
CFM	Clofazimine	NIR	Near-infrared
CFU	Colony forming unit	ns	Not significant
CLR	Clarithromycin	NT	Not treated
CT	Computed tomography	NTM	Nontuberculous mycobacteria
d	Days	PBTZ	Piperazine benzothiazinone
dpi	Days post infection	PET	Positron emission tomography
DprE1	Decaprenyl-phospho-β-D-ribose oxidase	PYR	Pyrdomycin
FDG	2-deoxy-2-[¹⁸ F]fluoro-D-glucose	RD1	Region of differentiation 1
FFlucRT	Red-shifted thermostable firefly luciferase-based reporter	RR	Rifampicin-resistant
FMNH ₂	Reduced flavin mononucleotide	S.E.M., s.e.m.	Standard error of the mean
FP	Fluorescent protein	SAR	Structure-activity relationship
h	Hours	SCID	Severe combined immunodeficiency
HIV	Human immunodeficiency virus	SD	Standard deviation
HO1	Heme oxygenase 1	SHO	SCID hairless outbred
hpf	Hours post fertilization	TAMRA	Tetramethylrhodamine
INH	Isoniazid	TB	Tuberculosis
Lux	<i>luxCDABE</i> -based reporter	WHO	World Health Organization
MCZ	Macozinone (PBTZ169)		

Curriculum Vitae

Raphael Sommer, PhD MICROBIOLOGIST

Profile

Expertise in drug discovery targeting infectious diseases and imaging technologies

Background in biology, chemistry and biological engineering

Integrated and multidisciplinary scientific approaches

Interest in health-related disciplines and life sciences

raphael.sommer@epfl.ch
raphael.sommer@bluewin.ch

+41 79 265 08 25

EPFL SV GHI UPCOL
Station 19
CH-1015 Lausanne
Switzerland

Mycobacteriology ✓

Drug discovery ✓

Mouse models ✓

Zebrafish models ✓

Molecular biology ✓

Microbial pathogenesis ✓

(A)BSL3 expertise ✓

Languages:

French (native)

English (C1)

German (B1)

swiss

not married

*03.04.1990

driving license cat. B

Education and Training

PhD Candidate in Molecular Life Sciences

Feb. 2015 to date

Swiss Federal Institute of Technology (EPFL, Lausanne)
Laboratory of Microbial Pathogenesis

Thesis: *Innovative Tools and in vivo Methods for Tuberculosis Drug Discovery and Development.*

Under the supervision of Prof. Stewart T. Cole and Prof. Andy Oates.

- Characterization of drug-target interaction with antibiotic-derived, bacterial-specific fluorescent probes, with applications *in vitro* and *in vivo*.
- Design, construction and optimization of genetically engineered fluorescent and bioluminescent bacterial reporters, for imaging in mouse models.
- Installation and operation of an *in vivo* imaging platform to assess the bacterial burden of *M. tuberculosis*-infected mice, evaluation of disease progression and drug efficacy in real time.
- Implementation of a zebrafish embryo infection model as a tool for drug discovery and development.
- Skills in bacteriology (*M. tuberculosis* and other mycobacteria), drug discovery and development, molecular biology and cloning, BSL2 / (A)BSL3 expertise, mouse models (FELASA Cat. B), *in vivo* imaging, zebrafish models, microscopy (fluorescence, confocal, super-resolution), image analysis, infection biology and pathogenesis, *in vitro* and *in vivo* infection assays.

MSc in Life Sciences and Technology

2012 – 2014

(Engineer in Life Sciences and Technology dipl. EPFL)

Swiss Federal Institute of Technology (EPFL, Lausanne)

Specialization in Molecular Medicine. Competences in disease biology (cancer, infection), immunology and pharmacology. Capacity to bring an innovative and molecular-oriented approach to cellular biology.

BSc in Chemistry and Chemical Engineering

2008 – 2012

Swiss Federal Institute of Technology (EPFL, Lausanne)

Synthetic, medicinal and biological chemistry, biochemistry, mathematics, physics.

Professional Experience

Master Thesis

02 – 08, 2014

Institute for Bioscience and Biotechnology Research, Rockville (MD), USA

- Production, purification and study of recombinant proteins, to investigate their potential roles in tumor development. Technical skills in PCR, molecular cloning, expression and purification of recombinant proteins, fast protein liquid chromatography (ÅKTA), affinity studies (ITC). Adaptation to international environment, communication in English.

Engineering Internship in Industry

07 – 09, 2013

Debiopharm International SA, R&D Unit, Ecublens (VD)

- Development of an optimized formulation for a poorly soluble API and excipient screening. Skills: work in private sector, teamwork and reporting, solubility analysis, basics in pharmaceutical formulation.

Teaching Assistant

2010 – 2018

Swiss Federal Institute of Technology (EPFL, Lausanne)

- Supervision of practical work and theoretical exercises. Acquired competences: communication and teaching skills, public speaking.

List of Publications

Comparative analysis of luciferase-based systems for bioluminescence imaging of tuberculosis infection in mice. Sommer, R., and Cole, S. T: **2019** (in preparation)

Monitoring tuberculosis drug activity in live animals by near-infrared fluorescence imaging. Sommer, R., and Cole, S. T: **2019** (in preparation)

Fluorescent benzothiazinone analogues efficiently and selectively label DprE1 in mycobacteria and actinobacteria. Sommer, R., Neres, J., Piton, J., Dhar, N., van der Sar, A., Mukherjee, R., Laroche, T., Dyson, P. J., McKinney, J. D., Bitter, W., Makarov, V., and Cole, S. T: *ACS Chem. Biol.* **2018**, 13, 3184–3192.

Arylvinylpiperazine amides, a new class of potent inhibitors targeting QcrB of *Mycobacterium tuberculosis*. Foo, C. S., Lupien, A., Kienle, M., Vocat, A., Benjak, A., Sommer, R., Lamprecht, D. A., Steyn, A. J. C., Pethe, K., Piton, J., Altmann, K.-H., and Cole, S. T: *mBio* **2018**, 9 (5), e01276-18

The inosine monophosphate dehydrogenase, Guab2, is a vulnerable new bactericidal drug target for tuberculosis. Singh, V., Donini, S., Pacitto, A., Sala, C., Hartkoorn, R. C., Dhar, N., Keri, G., Ascher, D. B., Mondésert, G., Vocat, A., Lupien, A., Sommer, R., Vermet, H., Lagrange, S., Buechler, J., Warner, D. F., McKinney, J. D., Pato, J., Cole, S. T., Blundell, T. L., Rizzi, M., and Mizrahi, V: *ACS Infect. Dis.* **2017**, 3, 5–17.

Talks and Posters

Le poisson zèbre – un modèle animal pour la recherche biomédicale

Sommer, R., ‘Association Suisse pour la Formation en Soins Animaliers – formation continue’, October 04, 2018, Lausanne, Switzerland. *Invited talk for an animal care continuous education program (in French)*

Zebrafish embryos as models to study tuberculosis and their application in drug discover

Sommer, R., Cole, S. T and Oates, A. C. ‘Global Health Institute retreat’, June 18-20, 2018, Zermatt, Switzerland. *Prize for the Best Talk by a PhD student*

Zebrafish embryos as models to study tuberculosis and their application in drug discovery

Sommer, R., Cole, S. T and Oates, A. C. ‘11th Swiss Zebrafish Meeting’, May 18, 2018, Lausanne, Switzerland. *Contributed talk*

Tuberculosis imaging

Sommer, R. ‘My Thesis in 180 Seconds Competition’ (<https://www.youtube.com/watch?v=zD70ySvSqY>) October 10, 2016, Lausanne, Switzerland. *Finalist at the EPFL contest (in French)*

Mycobacterial imaging with fluorescent benzothiazinones for *in vitro* and *in vivo* applications

Sommer, R. and Cole, S. T. ‘EMBO Conference Tuberculosis 2016’, September 19-23, 2016, Paris, France. *Poster presentation*

Computer Skills

- MS Office (Word, PowerPoint, Excel)
- GraphPad Prism, Fiji, ImageJ
- SnapGene, Adobe Illustrator

Other Interests

Movies, sports (ski, via ferrata),
music (clarinet), traveling.

**Ce document a été imprimé au Centre d'impression EPFL,
imprimerie climatiquement neutre, certifiée myClimate.**